

**Nanoscale Manganese Structures on Graphite Studied using
Synchrotron Radiation.**

Thesis submitted for the degree of
Doctor of Philosophy
at the University of Leicester

by

Anthony Mark Keen BSc (Leicester) MSc (Liverpool)
Department of Physics and Astronomy
University of Leicester

September 1996.

UMI Number: U087356

All rights reserved

INFORMATION TO ALL USERS

The quality of this reproduction is dependent upon the quality of the copy submitted.

In the unlikely event that the author did not send a complete manuscript and there are missing pages, these will be noted. Also, if material had to be removed, a note will indicate the deletion.



UMI U087356

Published by ProQuest LLC 2015. Copyright in the Dissertation held by the Author.
Microform Edition © ProQuest LLC.

All rights reserved. This work is protected against
unauthorized copying under Title 17, United States Code.



ProQuest LLC
789 East Eisenhower Parkway
P.O. Box 1346
Ann Arbor, MI 48106-1346



Nanoscale Manganese Structures on Graphite Studied using Synchrotron Radiation.

by Anthony Mark Keen

Abstract

The growth mode and the electronic and magnetic properties of nanoscale Mn structures, in the form of islanded films and deposited mesoscopic clusters, have been investigated using synchrotron radiation.

The Volmer-Weber growth of Mn films was studied by modelling the surface reflectivity in the extreme ultraviolet region (6-36 nm). The island growth at 423 K showed a change in growth mode as a function of coverage.

Spin Polarised Photoelectron Diffraction (SPPED) from thick Mn revealed that the short range magnetic order (SRMO) is lost at a temperature of 505 K, 5.3 times the bulk Néel Temperature. Results for an islanded film, where the average island size was 6 nm, showed surprisingly that SRMO breaks down at the bulk Mn Néel temperature, with the interpretation that a complete loss of magnetic order is induced down to atomic length scales in the mesoscopic system.

Core level and valence band photoemission from islanded Mn films have shown modified lineshapes in comparison to the bulk. The peak asymmetry of the 3p core level increases with decreasing particle size indicating a perturbation of the collective electron response upon the production of a core hole. The valence band and 3p core level photoemission also showed marked changes in lineshape as the temperature was increased through the bulk Mn Néel temperature.

Mesoscopic Mn clusters have been deposited *in-situ* with the use of a high temperature gas aggregation source. Both unfiltered and size-selected 2.5 nm clusters have been investigated. Photoemission from exposed clusters showed significant changes in the Mn 3s core level line shape with respect to the bulk, interpreted as an enhanced atomic magnetic moment. Unfiltered Mn clusters were also embedded in a V matrix revealing a satellite structure in the 3s photoemission from V suggesting that the Mn clusters magnetically polarise surrounding V atoms.

Acknowledgements

I would like to thank Dr. C. Binns for his supervision during the course of this work. I also wish to thank the EPSRC for the provision of a studentship.

I have gained much experience from working within the Surface Science group headed by Prof. C. Norris, with whom it has been a privilege to work, however he has serious misguided loyalties in his support of a particular north London football club. It has also been a pleasure to work with the "spanner men" - Dart, Fat Bloke, Barker, Steady, Maj, Kev, welsh bloke, and Cath (the honorary spanner bloke). Without the help of Steve B and Stu M i'm sure that most of the experiments would have been possible! Many thanks.

I would like to express my gratitude to Mr. S. C. Thornton and Mr. J. S. G. Taylor for their excellent design work and technical expertise. The work of the Leicester Physics department mechanical and electrical workshops is also gratefully acknowledged. All of the experiments were carried out at the CCLRC Daresbury Laboratory, and I am indebted to the staff there for all their assistance.

Finally, I cannot thank enough my family and friends for all their support during the course of my studies.

Contents

Chapter 1	Introduction	1
Chapter 2	Theoretical Background	8
2.1	Introduction	9
2.2	Photoemission	11
2.2.1	The Basic Process	11
2.2.2	The Three-Step Model	15
2.2.3	The One-Step Model	17
2.3	XUV Reflectivity	18
2.3.1	Islanded Film Model	19
2.4	Spin Polarised Photoelectron Diffraction (SPPED)	21
2.4.1	Spin-Dependent Scattering Effects in PED	26
	Exchange Scattering	26
	Spin-Orbit Scattering	27
Chapter 3	Experimental Details	29
3.1	Introduction	30
3.2	Surface Science	30
3.2.1	UHV Chamber	30
3.2.2	Sample Manipulation	31
3.2.3	Sample Heating and Cooling	35
3.2.4	Substrate Preparation	38
3.2.5	Metal Vapour Sources	39

	Knudsen Cell Evaporator	39
	Electron Beam Evaporator	41
3.2.6	Leicester University Mesoscopic Particle Source (LUMPS)	41
	Mass Filter	45
3.3	Experimental Measurements	48
3.3.1	Synchrotron Radiation	48
3.3.2	Beamline 6.1 - Grazing Incidence Monochromator (GIM)	49
3.3.3	Photoelectron detection	52
	Concentric hemispherical analyser	52
Chapter 4	The Growth of Mn on HOPG	54
4.1	Introduction	55
4.2	Experimental	57
4.3	Analysis Procedure	58
4.4	Results and Discussion	59
4.5	Summary	67
Chapter 5	A SPPED study of Manganese on (HOPG) Graphite	69
5.1	Introduction	70
5.2	Experimental	75
5.3	Analysis Procedure	75
5.4	SPPED Results of Mn Films on (HOPG)	79
5.4.1	Thick Mn Film	79
5.4.2	Islanded Mn Film	82

5.5	Discussion	85
5.6	Summary	89
Chapter 6	Photoemission from Bulk Mn and Mesoscopic Mn particles.	90
6.1	Introduction	91
6.2	Experimental	92
6.3	Results and Discussion	92
6.4	Summary	96
Chapter 7	Photoemission from Deposited Mesoscopic Manganese Clusters.	97
7.1	Introduction	98
7.2	Experimental	99
7.3	TEM and Size Distributions	100
7.4	Results	103
7.5	Discussion	109
7.6	Summary	111
Chapter 8	Summary and Suggestions for Further Work	113
8.1	Introduction	114
8.2	Mn Growth	114
8.3	Photoemission and SPPED Results from Mn	115
8.4	Investigation of Deposited Clusters	117
8.5	Suggestions for Further Work	118

Publications

120

References

122

Chapter 1

Introduction

In general the macroscopic properties of materials, their physical and chemical traits, are determined by the specific arrangement of atoms and their outer electron configuration. Reducing the dimensions of a system, for instance by introducing a surface as the termination of a bulk crystal lattice, produces an atomic environment which is significantly different from the bulk. The number of nearest neighbours is reduced and the atoms in the top most layers will not remain in the bulk configuration, they will relax in the plane perpendicular to the surface, and reconstruct in the plane parallel to it. This general reorganisation of atoms can manifest itself as modified electronic and magnetic properties.

With the development of nano-technology and techniques such as molecular beam epitaxy (MBE) it is possible to grow ultra-thin films in the form of monolayers and superlattice structures. In these systems the reduction in atomic co-ordination number can induce effects such as shifts in electron energy levels and modification of the densities of states. As a consequence of the reduced atomic co-ordination, the d-band width at metal surfaces is smaller than in the bulk resulting, in general, in an increase in the local magnetic moment and possibly a modification of the spin arrangement. For instance V and Mn in the bulk are paramagnetic and antiferromagnetic respectively but investigations of deposited ultra-thin V films on Fe(100) (Walker *et al* 1994) and highly oriented pyrolytic graphite (HOPG) (Binns *et al* 1992(i)) indicate net magnetic moments at the surface and investigations of

deposited ultra-thin Mn films on Fe(100) (Walker *et al* 1993) and Co(100) (O'Brien *et al* 1994) indicate ferromagnetic ordering of the overlayer. The role of dimensionality in the modification of a material's properties is, therefore, paramount.

From this perspective ultra-small particles, that is aggregates of atoms in the size range 1nm to 10nm, will have properties different from the solid state regime, since they can be considered either as low (zero-) dimensional (quantum dots) or systems in which the proportion of surface atoms is enhanced. Particles with diameters smaller than 1nm are more properly regarded as atomic clusters and show stepwise changes in their behaviour as a function of size. Particularly significant changes are observed when the number of atoms coincides with a 'magic number' corresponding to the completion of an atomic or electronic shell. Above 2nm the particles are referred to as **mesoscopic** and generally adopt the bulk crystal structure (although this may be multi-twinned in order to produce the minimum energy morphology). Their unusual properties, which tend to vary smoothly as a function of the particle size in this region, arise from quantum size effects, the finite confinement of the valence electron gas and the dominance of the surface.

As the size of the particle is reduced a number of effects come into play. The valence band energy level spacing becomes significant relative to other energy parameters, such as the thermal energy kT and the Zeeman energy $\mu_B H$. This quantum size effect can lead to anomalous thermodynamic and magnetic properties (Kubo 1962). For example, an enhanced paramagnetic susceptibility

is predicted at low temperatures with the temperature-independent Pauli paramagnetism replaced by a Curie law dependence (Kobayashi *et al* 1972). There is a size dependent perturbation of the collective electron behaviour producing a less effective screening response as a core hole is photoionised. This can be envisaged as a 'stiffening' of the electron gas as it becomes more confined. Also the enhanced proportion of low co-ordinated atoms at the surface (or interface) implies a further perturbation of the bulk electronic structure. Lowering the co-ordination has the effect of narrowing the valence d-band responsible for magnetism and increasing the density of states at the Fermi surface with a resulting increase in the local magnetic moment. The observed enhancement, by up to 36% over the bulk value, of the average atomic moment in ultra-small Fe, Co and Ni particles (Metzger *et al* 1994, Bucher *et al* 1991, Billas *et al* 1994 (i), Billas *et al* 1994 (ii)) has been attributed to this factor as has the recent discovery of 4d magnetism in small Rh clusters (Cox *et al* 1994).

Although free particles represent the most unperturbed form, there are reasons for studying particles when supported on solid surfaces or embedded within a matrix. The substrate allows control of temperature over a wide range and inhibits rotational disorder between particles allowing anisotropy within a particle to be determined. Sufficiently high planar densities can be achieved to exploit the power of surface sensitive techniques, such as photoemission, and also interesting effects can be introduced by particle-host and particle-particle interactions. Xhie *et al* 1991 and Xhie *et al* 1992 have performed scanning tunnelling microscopy (STM) studies of Pt and Co particles on graphite where charge density waves (CDW's) were induced on the graphite surface with a

tendency for the particles to assemble at the nodes of the CDW and Sattler 1992 has reported ordered arrays of Au particles on graphite. These cluster lattice systems represent a new form of matter in which some intrinsic properties of the free particles can be retained in the supported assembly. Chen *et al* 1994 have reported Co clusters of average size 1.8nm supported in a DDAB matrix showing a 20% increase in the atomic magnetic moment which is in reasonable agreement with the value for free clusters of the same size (Billas *et al* 1994).

In recent years there has been a significant expansion of interest in experimental and theoretical studies of mesoscopic particles which has been motivated in part by the technological potential of supported USPs. For example, the recent discovery of the giant magneto-resistance (GMR) effect in granular films and its potential applications to the magnetic recording industry. GMR was first observed in Fe/Cr multilayers by Baibich *et al* (1988) but has since been observed in ultra-small Co precipitates in Cu-Co alloys by Berkowitz *et al* (1992) and other multilayered and granular films Gijs *et al* 1992, Parkin *et al* (1993), Tsoukatos *et al* (1992) and Maeda *et al* (1992). The creation of new materials with modified mechanical properties is also possible by inserting mesoscopic particles into inert matrices to produce ultra-fine grained solids, proceedings ISPCFS (1992) and references therein. Ductile ceramics and metals with dramatically increased strength are examples of these materials which owe their properties to a reduced grain size and a large proportion of atoms at grain boundaries. Other important technologies include catalysis, photocathodes and ultra-cold refrigeration, S Umemura (1986).

This thesis describes measurements made on mesoscopic Mn particles supported on graphite and is part of a continuing programme of research at Leicester into systems of low dimensions. The work falls into two categories; (i) islanded Mn films grown on graphite by vacuum evaporation, which constitutes the bulk of the work reported and (ii) deposited ready-made mesoscopic Mn clusters. Previous investigations by the Leicester group employed the first method of sample production, using compact metal vapour sources and conditions such that Volmer-Weber growth would occur. During the course of this experimental work, though, the overall programme was being advanced with the development of a gas aggregation source for the *in-situ* deposition of clusters. This facility was used in the latter stages of the project and the first experimental data is presented here.

The work carried out in the study of islanded films includes an investigation into the growth and morphology of the discontinuous films from very low coverages to the point where the islands have agglomerated into a thick film. In studying islanded films there is a major problem of determining the average size of the islands in-situ, this has been solved by the development of a technique to determine the size and wavelength dependence of scattering in the XUV region by an islanded film from a reflectivity measurement. The spectral dependence of the reflectivity of the film in the XUV region is measured and compared to the reflectivity of the clean substrate surface modified by the size-dependent scattering by the particles. The fit is then optimised as a function of certain parameters one of them being the average island size.

Photoelectron spectroscopy, used with synchrotron radiation, has been employed to investigate changes in core level lineshapes and valence band photoemission from the islanded films in comparison with the bulk. It is an ideal tool for investigating the electronic structure of ultra-thin layers being surface sensitive and capable of probing states far from the Fermi level. Magnetic order has been investigated using spin-polarised photoelectron diffraction (SPPED) (Sinkovic and Fadley 1985). This is an emerging technique which utilises the natural spin-polarisation of the exchange split core levels in transition metals. If the emitting atom is surrounded by a magnetically ordered structure, differential scattering of the spin-up and spin-down components will occur. In its simplest form the experiment looks for an abrupt step in the plot of the intensity ratio of s multiplets with increasing temperature indicating a breakdown in short-range magnetic order (SRMO).

The work carried out in the study of deposited Mn clusters concentrates on core level and valence band photoemission measurements of uncovered dilute assemblies of deposited clusters from both mass-filtered and unfiltered particle beams with the view to obtain information on the cluster size dependence of the magnetic properties of these films. Unfiltered particles have also been embedded in a continuous V matrix to make a nano-scale granular film and investigate the possibility of magnetic ordering in the V matrix. Throughout all of the studies highly oriented pyrolytic graphite (HOPG) was chosen as a substrate. It has a low surface free energy which allows for easy islanding of the overlayer and is very inert remaining clean in ultra-high vacuum (UHV) conditions for long periods.

Chapter 2 gives an outline of the theory of photoelectron spectroscopy and the basic principles of spin-polarised photoelectron diffraction along with a description of the theoretical model used in the growth study. Chapter 3 explains the experimental details involved in the studies, including the specific equipment used for growing the Mn islands *in-situ* and also for the production of the clusters. In chapter 4 is presented the study on the growth and morphology of islanded Mn films. A SPPED study of islanded and bulk Mn films is presented in chapter 5. Chapter 6 presents a photoemission study of islanded Mn films compared to the bulk and chapter 7 presents the photoemission study of deposited exposed Mn clusters and incorporated into a V matrix. The experimental work is summarised in chapter 8 along with some suggestions for further work.

Chapter 2

Theoretical Background

- 2.1 Introduction
- 2.2 Photoemission
 - 2.2.1 The Basic Process
 - 2.2.2 The Three-Step Model
 - 2.2.3 The One-Step Model
- 2.3 XUV Reflectivity
 - 2.3.1 Islanded Film Model
- 2.4 Spin Polarised Photoelectron Diffraction (SPPED)
 - 2.4.1 Spin-Dependent Scattering Effects in PED
 - Exchange Scattering
 - Spin-Orbit Scattering

Chapter 2

Theoretical Background

2.1 Introduction

With the ability to grow ultra-thin films *in-situ* it is possible to create novel structures where the role of the surface is artificially enhanced, for instance in mesoscopic particles. This is usually accompanied by a modification of the material's properties at the surface relative to the bulk and it becomes necessary to investigate these films with experimental probes which are surface sensitive. The experimental probe used in the investigation of the electronic structure and magnetic properties of the discontinuous films and deposited clusters is photoelectron spectroscopy (PES). An important factor governing the surface sensitivity of any technique which requires the detection of primary electrons, i.e. those which have not been inelastically scattered, is the energy of the probe used. For this work the electron energies fall in the range 10-200eV and from figure 2.1, after Seah and Dench (1979), confirmation that this emission is from the surface region is found. It shows the element independent *universal curve*, which is the inelastic mean free path of electrons from various elements as a function of the electron energy. The graph shows a broad minimum between 50 and 100eV indicating that electrons in the energy range of interest are derived from the first few atomic layers.

The technique of spin-polarised photoelectron-diffraction (SPPED) has been used to obtain information on magnetic order. It utilises the multiplet split

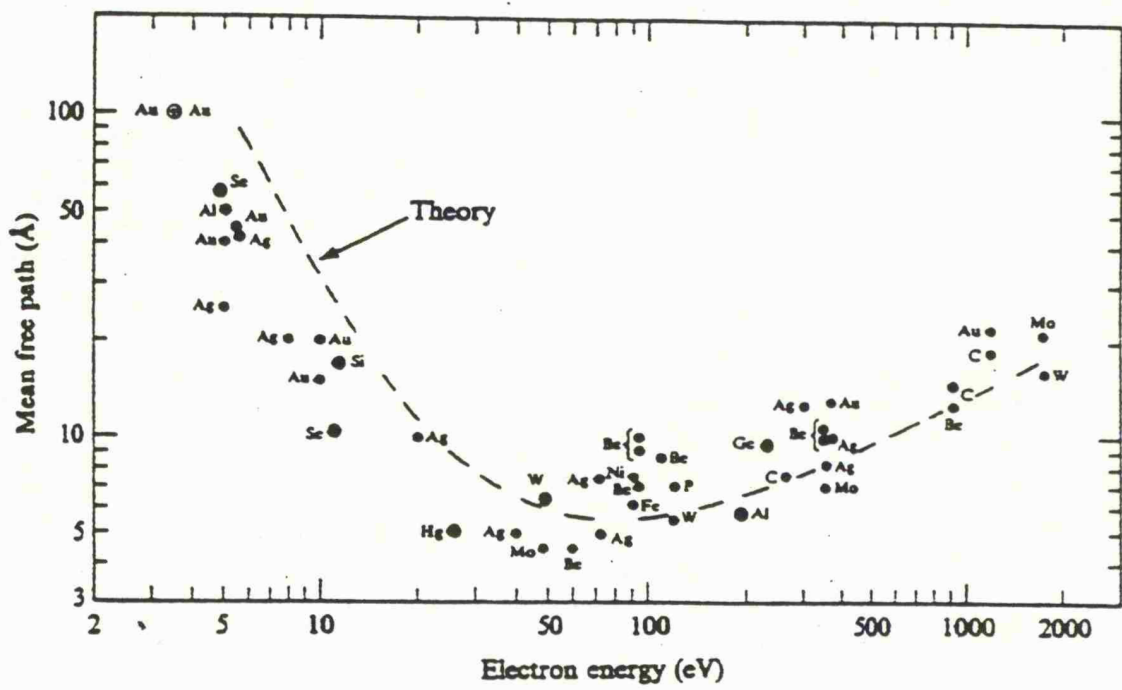


Figure 2.1 Universal curve of inelastic mean free path of electrons.

nature of core-level photoelectrons as a source of highly spin-polarised electrons for which spin-dependent scattering and diffraction could occur during photoelectron escape from the specimen. This chapter presents basic principles and theoretical aspects of photoemission and SPPED, and a description of the theory underlying the reflectivity model used in the growth study, including references giving more extensive details.

2.2 Photoemission

2.2.1 The Basic Process

Photoelectron emission involves the emission of electrons from matter in response to photons being absorbed by it, illustrated in figure 2.2(a). The electrons may reach the surface without being scattered or they may suffer scattering. Phonon scattering may influence the direction of the outgoing electron but the energy change is small. Alternatively the electron can suffer inelastic scattering with a substantial loss of energy. Figure 2.2(b) also depicts a typical energy distribution curve (EDC) showing sharply structured features, the primary electrons, on a featureless smooth secondary electron background. The primary electrons are those which have not undergone inelastic scattering whereas the secondary electrons have. The mean free path for inelastic scattering of electrons depends strongly on the electron energy so that, in general, primary electrons of different energies may emerge from different average escape depths below the surface (see figure 2.1). Electrons with kinetic energies in the range 10-1000eV above the fermi energy E_F are scattered quite

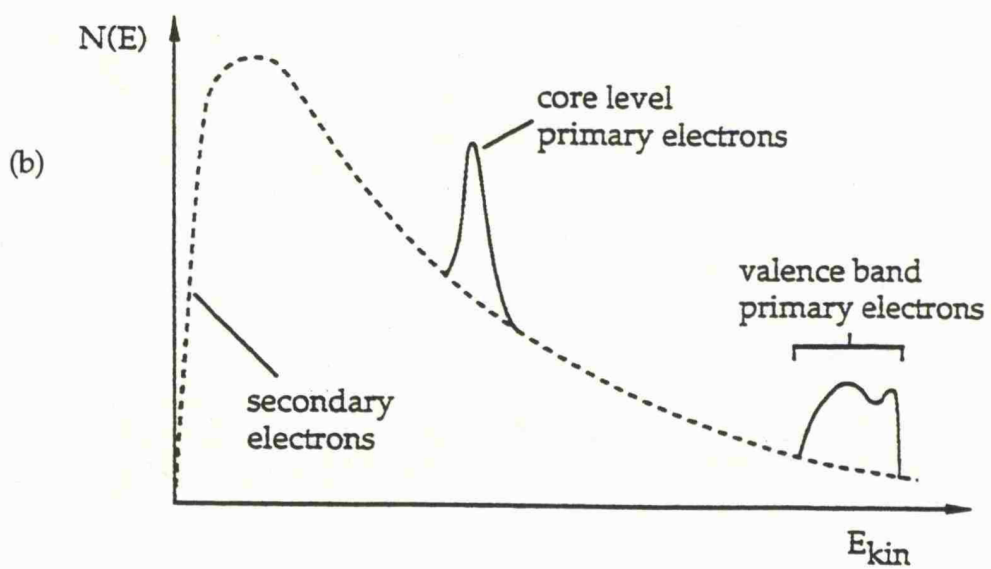
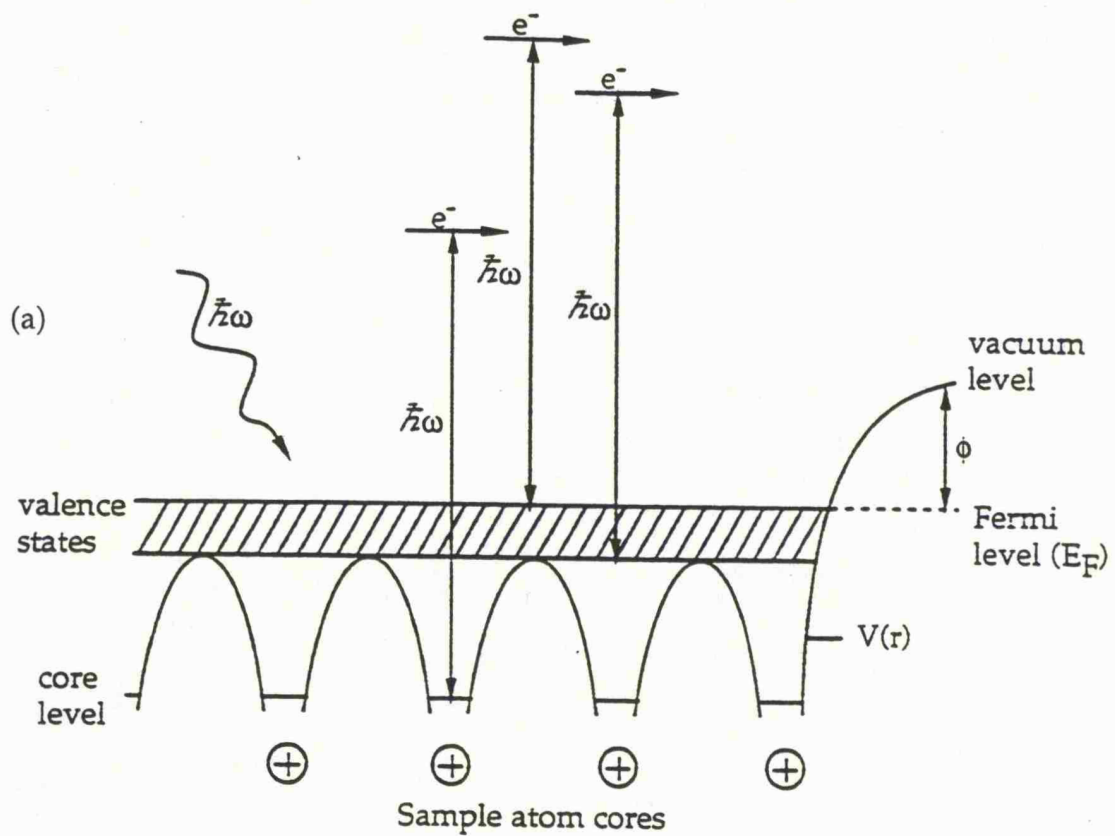


Figure 2.2 (a) Illustration of the photoemission process, (b) a typical EDC..

strongly in solids and consequently those which emerge without any serious degradation of energy must originate very close to the surface.

The experimental geometry is detailed in figure 2.3. A monochromatic beam of photons is incident at an angle θ_i with respect to the surface normal and an azimuthal angle ϕ_i with respect to a crystallographic direction. The photons can excite emission of electrons, in a direction labelled by the two angles θ_e and ϕ_e , from levels with a binding energy (E_b) less than the beam energy ($\hbar\omega$). For metals it is convenient to define the binding energy relative to the Fermi level (E_F) to allow for the work function (ϕ) in a modified Einstein relation :-

$$E_b = \hbar\omega - E_k \quad (2.1)$$

where E_k is the kinetic energy of the emitted electron with respect to the Fermi level. The escape time of photoelectrons of more than a few eV kinetic energy is comparable to the typical transition time between electronic states, about 10^{-15} s. Therefore the atoms do not have enough time to rearrange themselves and thereby change the electronic states during the photoemission process. This is referred to as a frozen orbital approach and is a combination of the Frank-Condon and the Born-Oppenheimer principles.

In the semi-classical approximation, where the photon is treated classically and the electron is treated quantum-mechanically, the probability of exciting an electron from an initial state with wavefunction Ψ_i to a final state Ψ_f is proportional to M_{fi}^2 , where

$$M_{fi} = \langle \Psi_f | \mathbf{A} \cdot \mathbf{p} + \mathbf{p} \cdot \mathbf{A} | \Psi_i \rangle. \quad (2.2)$$

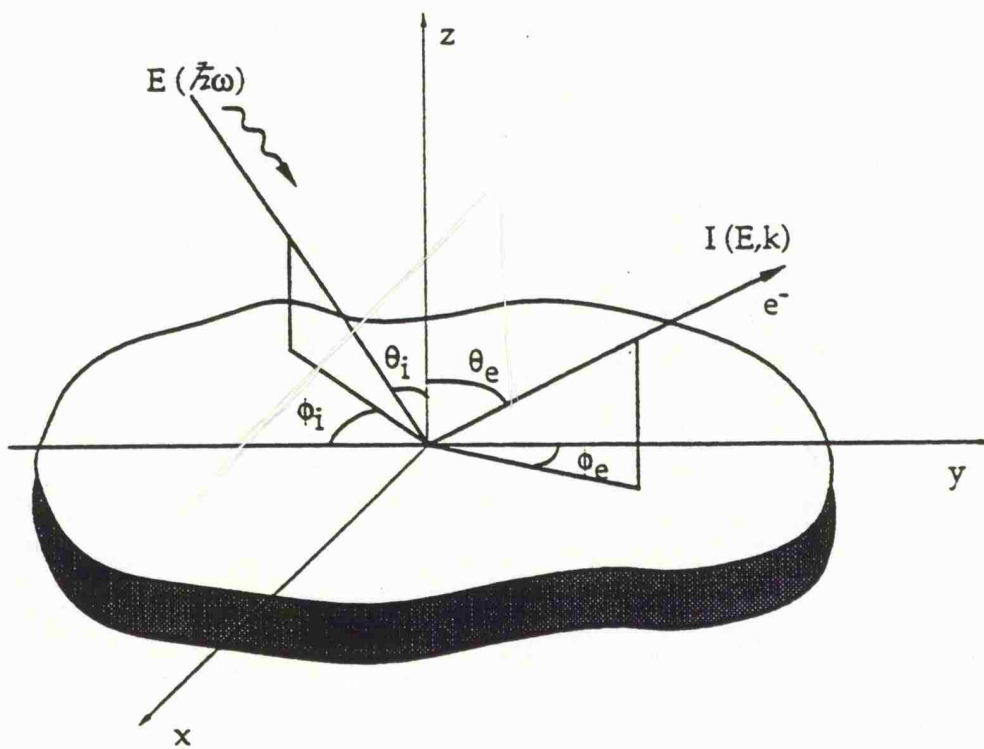


Figure 2.3 Experimental geometry for a photoemission experiment.

Here \mathbf{p} is the momentum operator and \mathbf{A} is the vector potential of the incoming radiation. It is normally assumed that $\nabla \cdot \mathbf{A} = 0$ so that

$$M_{fi} = \langle \Psi_f | \mathbf{A} \cdot \mathbf{p} | \Psi_i \rangle. \quad (2.3)$$

The theory of photoemission has always been of angle-resolved photoemission since angular effects have to be calculated before integrating over the angles to describe traditional angle-integrated data. There are numerous theoretical methods to explain photoemission from solids, however, they can be generally divided into two categories:

(i) Semiphenomenological theories, which are founded on the so-called 'three-step model' originally put forward by Spicer (1958). These attempt, in an approximate way, to divide the photoemission process into several steps and try to understand each of the steps in turn.

(ii) Microscopic theories, e.g. those due to Adawi (1964), Mahan (1970), Schaich and Ashcroft (1971), Caroli *et al* (1973), Feibelman and Eastman (1974), Pendry (1975, 1976), Holland (1977) and Li *et al* (1978) attempt to account for photoemission from a solid in terms of a single inelastic scattering event, the so-called 'single-step model'.

2.2.2 The Three-Step Model

Originally put forward by Spicer (1958), the 'three-step model' involves three independent processes: photoabsorption, propagation of the excited electron to the surface and escape of the photoelectron into the vacuum. If only the elastically scattered electrons are considered then the photocurrent is given by

$$I(E_i + \hbar\omega) = P(E_i + \hbar\omega)T(E_i + \hbar\omega)D(E_i + \hbar\omega) \quad (2.4)$$

where P, T and D are the photoabsorption, propagation and escape factors respectively. Cardona and Ley (1978) have shown that both the propagation and escape factors, T and D, are smoothly varying functions of E and are therefore not expected to give rise to any structure in $I(E_i + \hbar\omega)$. Photoabsorption is a quantum-mechanical process and the $P(E_i + \hbar\omega)$ factor is derived from first-order time-dependent perturbation theory. The optical transition probability, at a \mathbf{k} point, of electrons from bulk occupied states E_i into empty final states E_f is given by the following 'golden rule' type formula,

$$P(E_i + \hbar\omega) \propto \sum_{i,f} \int d^3\mathbf{k} |\langle i|\mathbf{p}|f\rangle|^2 \delta(E_f(\mathbf{k}) - E_i(\mathbf{k}) - \hbar\omega) \delta(E_f(\mathbf{k}) - E). \quad (2.5)$$

The assumption that these states are bulk implies that crystal momentum \mathbf{k} is a good quantum number which is to be conserved in the reduced zone scheme. The first delta function ensures that the photon energy is equal to the difference in energy of the initial and final states and the second delta function ensures that the energy E selected by the electron energy analyser is equal to the final energy E_f . By adding another delta function to equation (2.5) to provide for the conservation of the two-dimensional wave vector parallel to the surface the photocurrent is then given by the expression below,

$$I(E_i + \hbar\omega) \propto \sum_{i,f} \sum_{\mathbf{G}} \int_{\text{bz}} d^3\mathbf{k} |M_{fi}|^2 \delta(E_f(\mathbf{k}) - E_i(\mathbf{k}) - \hbar\omega) \times \delta(E_f(\mathbf{k}) - E) \delta_{\mathbf{k}_i + \mathbf{G}_i, \mathbf{K}_i} T(E_i + \hbar\omega) D(E_i + \hbar\omega) \quad (2.6)$$

An approximation used in computing the above expression is the joint density of states model. Here the matrix element M_{fi} and the factors T and D are assumed to be constants. This model can be used for band structure mapping as direct transitions in E-k space can be identified. There are major shortcomings with the model though, it is incapable of explaining the dependence of peak intensities on the photon energy, for metals the matrix element M_{fi} is not constant and it uses stationary initial and final-state wavefunctions for calculating M_{fi} which is not strictly correct as the photoemission process involves highly excited final states.

2.2.3 The One-Step Model

The one-step model considers the entire photoemission process as a single step, the photoexcited electron is allowed to undergo many-body scattering processes before it leaves the surface. Different formalisms have been developed (Adawi 1964, Mahan 1970, Schaich and Ashcroft 1971, Caroli *et al* 1973, Feibelman and Eastman 1974, Pendry 1976, Holland 1977, Bross 1977, Liebsch 1978) but all are based on the same theory. The differential cross section for the primary photoelectron emission is given by a golden rule expression:

$$\frac{\partial \sigma}{\partial \Omega}(E_f, \mathbf{k}_f^{\parallel}, \hbar\omega, \mathbf{A}) \propto \sqrt{(E_f - E_{\text{vac}})} \sum_i \left| \langle \Psi_f | \mathbf{p} \cdot \mathbf{A} + \mathbf{A} \cdot \mathbf{p} | \Psi_i \rangle \right|^2 \times \delta(E_f - E_i - \hbar\omega). \quad (2.7)$$

E_f and $\hbar \mathbf{k}_f^{\parallel}$ are the final state energy and the reduced momentum parallel to the surface, $\hbar\omega$ is the photon energy, \mathbf{A} is the vector potential of the electromagnetic field, \mathbf{p} is the momentum operator, E_i is the initial state

energy, E_{vac} is the vacuum level and Ψ_i and Ψ_f are the initial and final-state wavefunctions.

The photoeffect is induced via a perturbation of the crystal Hamiltonian by the dipole operator ($\mathbf{p}\cdot\mathbf{A}+\mathbf{A}\cdot\mathbf{p}$) which describes the interaction of the photon with the electron. Since a free electron cannot absorb a photon because energy and momentum cannot be conserved, the extra source of momentum in photoemission is provided by the crystal which gives rise to bulk and surface photoeffects. In this model the photoemission event affects the wavefunction Ψ_f . Ψ_f describes an electron state which contains an outgoing plane wave with the energy E_f and to fulfil the proper continuity requirements at the surface this state has to contain several other waves converging on to the surface.

Pendry (1976), with the objective of finding a rapid method of photoemission calculation, developed a theory entirely within a scattering formalism. This included all the important ingredients: band structure, surface effects, matrix elements, multiple scattering of initial and final-state wavefunctions and valence and final-state lifetime effects. The one-step model is more rigorous than the three-step model but involves much computational effort.

2.3 XUV Reflectivity

When growing islanded films it is important to know the average size of the islands without having to remove the film from UHV in order to determine any size dependency on the properties being measured. A technique has

therefore been developed to do this *in-situ* which involves measuring the spectral dependence of the reflectivity of the islanded film in the XUV region. This measured reflectivity is then modelled by calculating the reflectivity from the clean substrate modified by the overlayer.

2.3.1 Islanded Film Model

The theory used is that of Jarrett and Ward (1976) in which the reflectivity of an overlayer is calculated by considering it as a continuous film with an effective refractive index corresponding to an inhomogeneous medium. The model is based on the theory developed by Maxwell-Garnett (1904) which treated the discontinuous film as a dispersion of identical small metal spheres, it was extended by generalising the shape of the particles to ellipsoids of revolution, after David(1939), and arranging the ellipsoids on a surface and dealing with the specific interaction which occurs between such a two-dimensional array of dipoles, after Yamaguchi (1962).

Jarrett and Ward showed that the effective dielectric constants of the discontinuous film are given by

$$\epsilon'_1 = \frac{\epsilon_a \{1 + q[\epsilon_1 \epsilon_a (1 - 2F) + F(\epsilon_1^2 + \epsilon_2^2) - \epsilon_a^2 (1 - F)]\}}{[\epsilon_a + F(\epsilon_1 - \epsilon_a)]^2 + (F\epsilon_2)^2} \quad (2.8)$$

and

$$\epsilon'_2 = \frac{q\epsilon_2 \epsilon_a^2}{[\epsilon_a + F(\epsilon_1 - \epsilon_a)]^2 + (F\epsilon_2)^2}, \quad (2.9)$$

where ϵ_1 and ϵ_2 are the dielectric constants of the bulk material, ϵ_a is the dielectric constant of the medium in which the particles are situated, which is vacuum, q is the volume filling fraction of the film and F is a shape factor given by :

$$F = f(1 - q) \quad , \quad (2.10)$$

where f is the shape factor introduced by David (1939), which is dependent on the geometrical shape of the particle and has components parallel and perpendicular to the plane of the substrate defined by :

$$f_{//} = \frac{1}{2}w(w^2 + 1) \left[\frac{1}{2}\pi - \tan^{-1}w - \left(\frac{w}{w^2 + 1} \right) \right] \quad (2.11)$$

and

$$f_{\perp} = 1 - 2f_{//} \quad . \quad (2.12)$$

Here w is related to the ratio of the half axes, a and b of the ellipsoids by :

$$w = \frac{1}{b^2/a^2 - 1} \quad . \quad (2.13)$$

The effective refractive index of the film was calculated and the total reflectivity was obtained from the reflected amplitudes using equations (2.14) and (2.15)

$$r_{\perp} = \frac{r_{12\perp} + r_{23\perp}C}{1 + r_{12\perp}r_{23\perp}C} \quad (2.14)$$

$$r_{//} = \frac{r_{12//} + r_{23//}C}{1 + r_{12//}r_{23//}C} \quad (2.15)$$

where c is a complex exponent given by

$$c = e^{2\eta(iu_2 - v_2)} \quad (2.16)$$

with η being related to d , the film thickness, by

$$\eta = \frac{2\pi d}{\lambda}. \quad (2.17)$$

In equation (2.16) u_2 and v_2 are drawn from the calculated effective refractive index of the overlayer. A weighted fit index, defined by:

$$x = \sum \left\{ \left[\frac{R_m - R_{\min}}{R_{\max} - R_{\min}} \right] \left[\frac{R_m - R_c}{R_m} \right] \right\}^2 \quad (2.18)$$

where R_m and R_c are the measured and calculated reflectivities respectively and R_{\max} and R_{\min} are the maximum and minimum values of the measured reflectivity, was then minimised as a function of three parameters, the shape (b/a), the coverage (q) and the average island size (d).

2.4 Spin Polarised Photoelectron Diffraction (SPPED)

SPPED is an emerging technique for the study of magnetic behaviour in magnetic materials. Although experiments involving spin polarised electrons as both sources and emitters are well established Celotta *et al* (1979), Alvarado *et al* (1982), Raue *et al* (1983), Siegmann (1984), Siegmann *et al* (1984), Feder (1985), there exists the ability with SPPED to carry out spin polarisation experiments on photoelectrons using the photoemission process itself to polarise the electrons, therefore requiring no polarised radiation or external

spin detection. It is based on the structural technique of x-ray photoelectron diffraction (XPD) using core-level emission, and is sensitive to surface and near-neighbour magnetic order. Excitation occurs by the absorption of a photon, obeying the dipole selection rules, and the diffraction process results from the modulation of the primary wave by the scattered waves as the scattering potential is changed. For a magnetic sample this can be achieved by varying the temperature, this variation introduces magnetic fluctuations which affect the exchange part of the scattering potential for a spin-up photoelectron relative to that of a spin-down at a given scattering centre. The fact that SPPED involves internal sources of polarised electrons referenced to their respective emitters implies that it can be employed to study magnetic order in both ferromagnets and anti-ferromagnets.

In order to perform such an experiment two core photoelectron peaks are required that are well-resolved, close together in kinetic energy and highly spin polarised in opposite directions with respect to the magnetic moment of the emitter. The highest degree of spin polarisation of core-level photoelectrons is found in the multiplet splittings of partially filled 3d and 4f atoms.

Photoemission from s levels is of particular interest (figure 2.4), since the dominant features consist of a simple doublet with the lower binding energy peak being spin polarised anti-parallel to the magnetic moment of the emitter and the higher binding energy peak being spin polarised parallel to the magnetic moment of the emitter. It is not necessary to know the degree of spin polarisation, though it needs to be large to produce significant SPPED effects.

In the context of photoelectron diffraction a photoelectron, in a magnetically

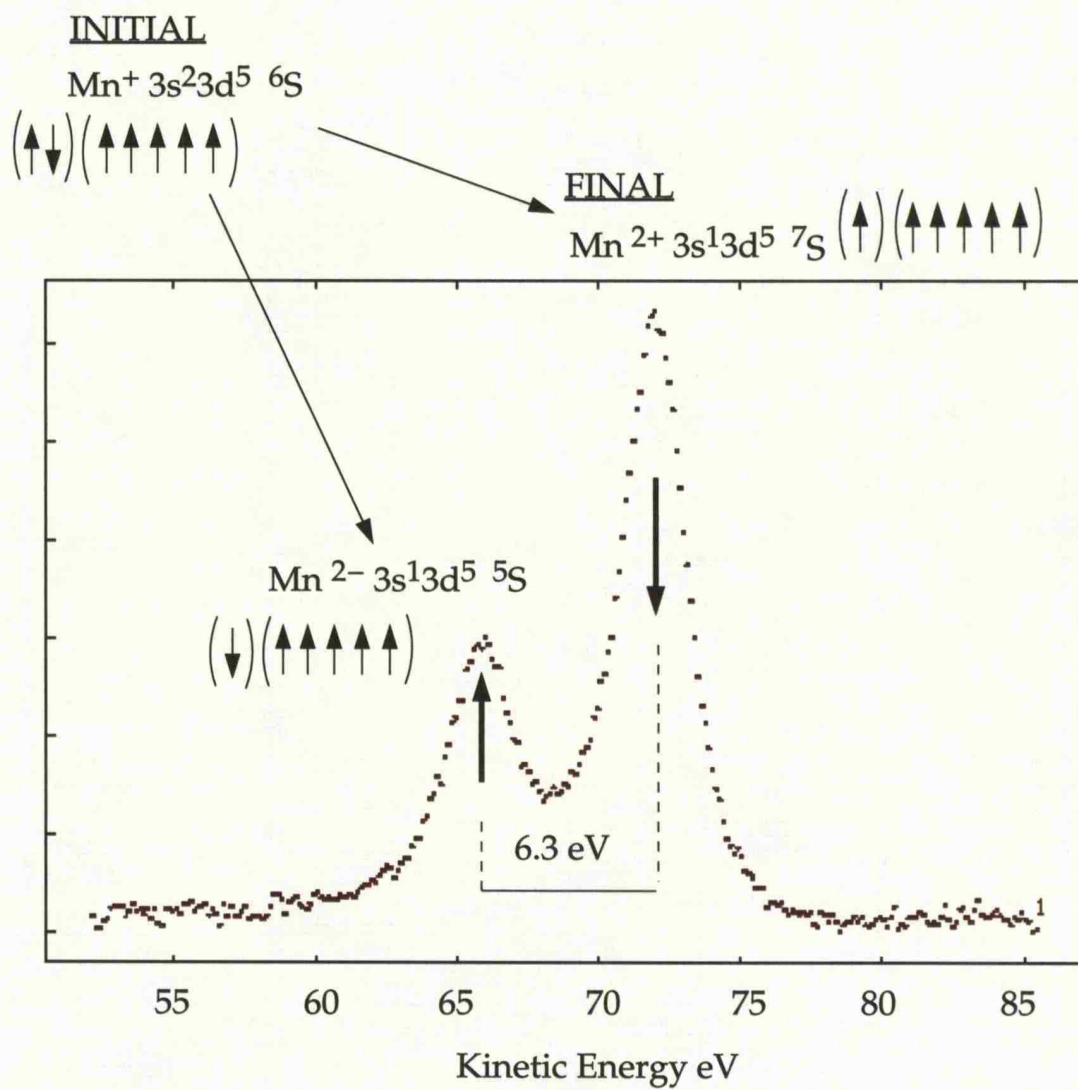


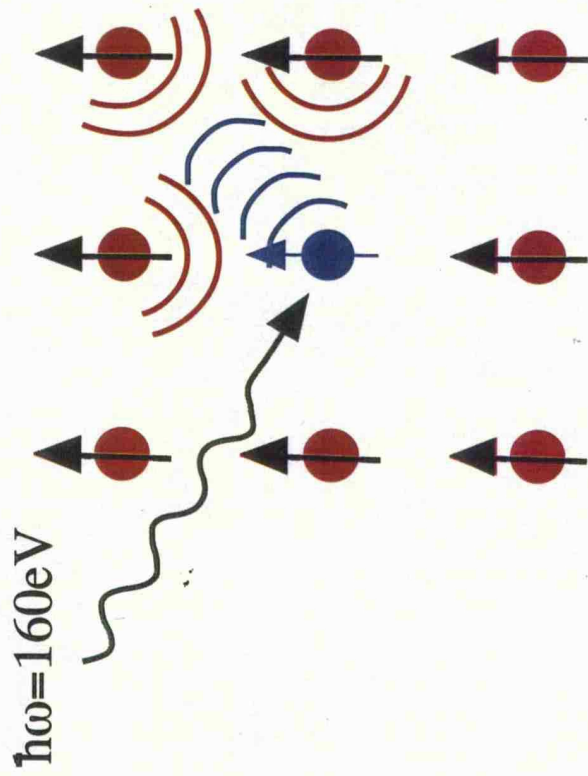
Figure 2.4 Photoelectron EDC in the region of the Mn 3s core level with the initial and final states involved in the photoemission process.

ordered material, which is polarised parallel to its emitter atom will have a definite polarisation with respect to the other magnetic atoms in the lattice, figure 2.5 (a). The diffraction of such a photoelectron from a neighbouring magnetic atom will thus depend on the relative orientation of the magnetic moments of the photoelectron and scatterer, since there will be a small additional exchange interaction if the two spins are parallel and no such interaction if the spins are anti-parallel. Thus the relative intensities of the two multiplet-split core peaks should be affected by the magnetic order of the lattice, or a change in magnetic order will manifest itself as a modification of the relative intensities of the core peaks as in figure 2.5 (b), after Sinkovic *et al* (1985), this is the crux of SPPED.

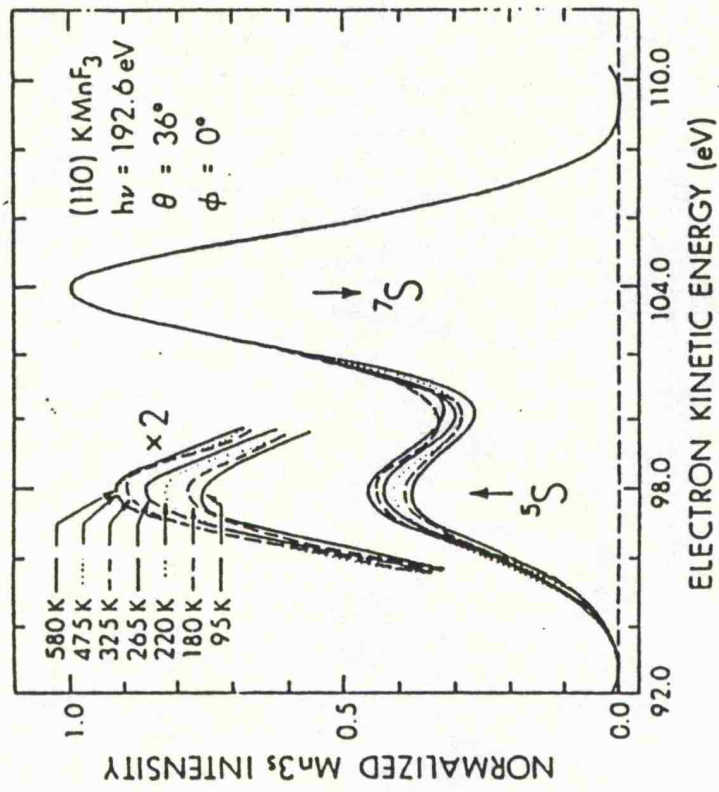
The spin dependent part of the diffraction process is expressed through a spin asymmetry, S :

$$S(\mathbf{k}) = \frac{I_{\uparrow}(\mathbf{k}) - I_{\downarrow}(\mathbf{k})}{I_{\uparrow}(\mathbf{k}) + I_{\downarrow}(\mathbf{k})} \quad (2.19)$$

where $I_{\uparrow}(I_{\downarrow})$ is the intensity of the elastically scattered spin-up (spin-down) electrons, \mathbf{k} is the final electron wave vector after the scattering and \mathbf{k}_0 will be defined as the initial wave vector before the scattering. To understand the information obtained from SPPED it is necessary to investigate the origin of the spin-dependent effects. The rest of this section deals briefly with the relevant mechanisms involved in spin-dependent scattering.



(a)



(b)

Figure 2.5 (a) Schematic of SPED, (b) Mn 3s photoelectron spectra at several temperatures, normalised to the 7S (spin down) peak, showing the change in relative intensity, after Sinkovic *et al* (1985).

2.4.1 Spin-Dependent Scattering Effects in PED

By analogy with prior analyses of spin-polarised LEED results spin dependent scattering effects in PED are expected to be caused principally by the spin-dependence of the elastic differential scattering cross-section. The intensity of such scattered electrons is determined by the scattering Hamiltonian,

$$H = V + V_{\text{ex}} + V_{\text{so}} \quad (2.20)$$

where V_{ex} is the valence exchange interaction, V_{so} is the spin-orbit interaction and V describes the spin independent part of the scattering potential. Two different mechanisms can therefore give rise to the spin-dependence: exchange and spin-orbit scattering .

Exchange scattering

By writing the exchange part of the scattering potential as the proportionality,

$$V_{\text{ex}} \propto J_s \cdot S \quad (2.21)$$

where J is the exchange coupling constant, s is the spin of the incident electron and S is the spin of the scattering atom, it can be concluded that the spin-dependence in the elastic cross-section will be observed only by the scattering of polarised electrons from atoms with a non-zero total spin moment. So performing a diffraction experiment on a solid with many scatterers an exchange induced spin asymmetry will only be produced from a solid with some degree of local magnetic order, and the magnitude of any asymmetry observed will be dependent on the relative orientation of the spin

of the electron with the spin of the scatterer. Consequently, since the electrons being scattered are spin-polarised with respect to the spin of the emitter, equation 2.17 can be written as,

$$V_{\text{ex}} \propto S_0 \cdot S_j \quad (2.22)$$

where S_0 is the spin of the emitter and S_j is the spin of the j th scatterer. Therefore SPED is directly sensitive to the relative spin orientation of a few shells of nearest neighbours.

Spin-orbit scattering

Spin-dependent electron-atom scattering can also be produced by the spin-orbit interaction. This part of the scattering potential is given by:

$$V_{\text{so}} \propto s \cdot L \quad (2.23)$$

where s is the spin of the electron and L is the angular momentum of the scattered electron. Kessler (1976) has shown in detail that the differential scattering cross section with the inclusion of V_{so} can be written as:

$$\sigma(\Delta\mathbf{k}) = \sigma(|\Delta\mathbf{k}|) [1 + S(|\Delta\mathbf{k}|) s \cdot \hat{\mathbf{n}}] \quad (2.24)$$

where $\Delta\mathbf{k} = \mathbf{k} - \mathbf{k}_0$ is the momentum transfer in the scattering, $\sigma(|\Delta\mathbf{k}|)$ is the spin-independent scattering cross section and $S(|\Delta\mathbf{k}|)$ is the Sherman function, s is the spin of the scattered electron, and $\hat{\mathbf{n}}$ is the normal to the scattering plane defined as:

$$\hat{\mathbf{n}} = \mathbf{k} \times \mathbf{k}_0 / |\mathbf{k} \times \mathbf{k}_0|. \quad (2.25)$$

Scattered intensities are proportional to the differential scattering cross section and from equations 2.15 and 2.21 the spin-orbit induced spin asymmetry S_{so} reduces to

$$S_{so} = S(|\Delta\mathbf{k}|)s \cdot \hat{n}, \quad (2.26)$$

consequently it is dependent on the relative orientation of the spin polarisation of the scattered electron and the normal to the scattering plane. Thus, spin-orbit induced spin asymmetries can be observed in the scattering of spin-polarised electrons from non-magnetic as well as magnetic solids.

Chapter 3

Experimental Details

3.1 Introduction

3.2 Surface Science

3.2.1 UHV Chamber

3.2.2 Sample Manipulation

3.2.3 Sample Heating and Cooling

3.2.4 Substrate Preparation

3.2.5 Metal Vapour Sources

Knudsen Cell Evaporator

Electron Beam Evaporator

3.2.6 Leicester University Mesoscopic Particle Source

(LUMPS)

Mass Filter

3.3 Experimental Measurements

3.3.1 Synchrotron Radiation

3.3.2 Beamline 6.1 - Grazing Incidence Monochromator

(GIM)

3.3.3 Photoelectron detection

Concentric hemispherical analyser

Chapter 3

Experimental Details

3.1 Introduction

A fundamental requirement in the study of surfaces and thin films is an ultra-high vacuum (UHV) environment. This is essential if the sample is to stay free from contamination for the long periods required to carry out surface science experiments (see Yarwood (1967) for a detailed description of the techniques necessary to achieve UHV). This chapter describes the equipment necessary to make the measurements reported in this thesis. It includes details about equipment used for the *in-situ* preparation, growth and investigation of islanded films at low base pressures. Included also are the details about a recently developed gas aggregation source, designed for the deposition of mass selected clusters.

3.2 Surface Science

3.2.1 UHV Chamber

The UHV system used to make the measurements was an endstation on one of the beamlines at the synchrotron radiation source (SRS) at the CCLRC Daresbury Laboratory, see section 3.3.1. The system is a general use facility and consists of the usual basic features; (i) the environmental chamber, (ii) pumping facilities for gas handling and to obtain UHV, (iii) a transfer load-lock

system and (iv) various facilities for sample characterisation. Users are required to set the system up to meet their needs with the equipment available and with any specialist equipment they have.

The environmental chamber, shown in plate 3.1, consists of a μ -metal cylinder with a number of ports of varying size to accommodate the necessary apparatus for the experiment. These include a liquid helium cooled manipulator (see section 3.2.2) a concentric hemispherical analyser for photoelectron spectroscopy (see section 3.3.3), a photomultiplier for the reflectivity measurements, various metal vapour sources for the deposition of pure materials (see section 3.2.5) and a VG SX 200 for Residual Gas Analysis. A purpose built gas aggregation cluster source for the deposition of ready made clusters (see section 3.2.6) can also be connected to the chamber by means of a UHV gate valve.

At UHV the chamber is pumped by a Varian 400 litres/sec ion pump and two liquid nitrogen cooled titanium sublimation pumps (TSP). During cluster deposition the ion pump is valved off and the main chamber is pumped by a Balzers 330 litres/sec turbomolecular pump with a liquid nitrogen cold trap. After baking the system at 150°C for approximately 18 hours a base pressure of 2×10^{-11} mbar can be routinely achieved.

3.2.2 Sample Manipulation

The sample position is controlled by means of a liquid helium cooled manipulator (see plate 3.2 and figure 3.1) which consists of a standard vacuum

Plate 3.1 Photograph of UHV chamber on SRS beamline 6.1.

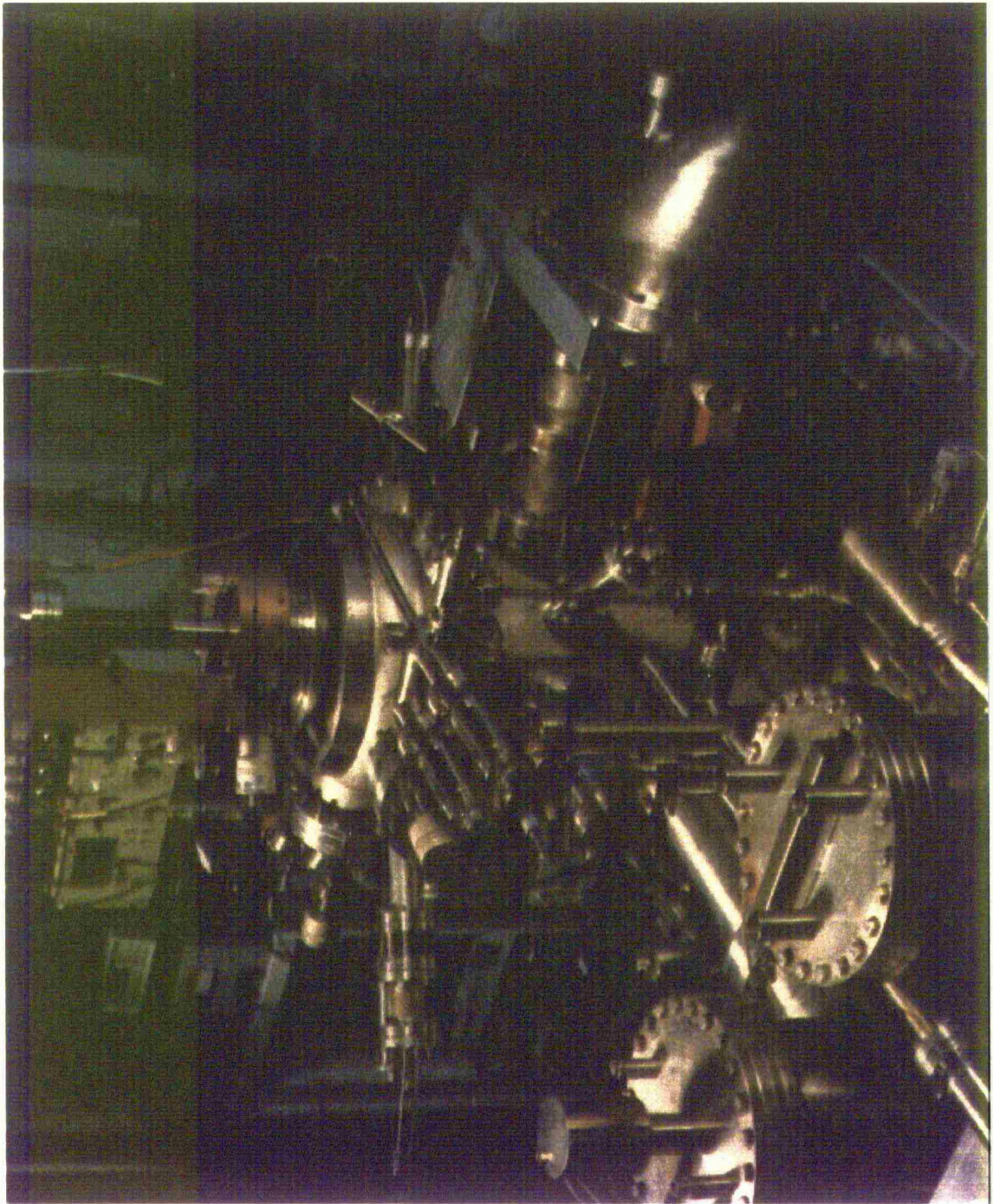


Plate 3.2 Photograph of liquid helium cooled manipulator.



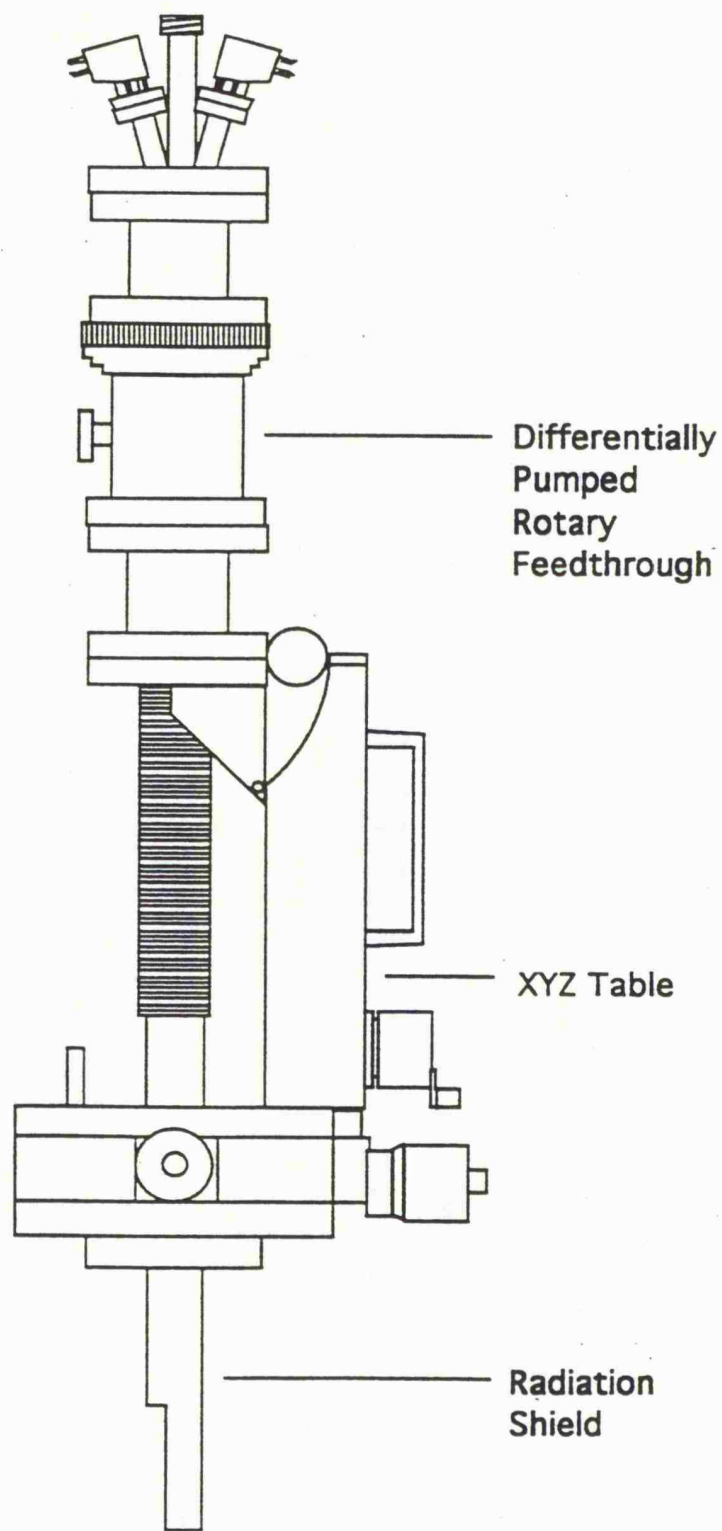


Figure 3.1 Schematic of liquid helium cooled manipulator.

generators (VG) HPLT series XYZ table with a differentially pumped rotary feedthrough (DPRF) and an Oxford Instruments CF1100 special continuous flow cryostat. The manipulator has the normal range of movement in the X, Y and Z directions and unrestrained polar rotation because the liquid helium delivery is along the manipulator axis and the DPRF has no limit of rotation. The sample plate cannot however rotate azimuthally because radial size limitations are imposed by a radiation shield.

The DPRF requires a vacuum of less than 10^{-2} mbar in the interspace between the vacuum seals in order to maintain a minimum pressure burst during rotation, and the whole assembly can be baked to a temperature of 150°C. The manipulator design also features an oxygen free high conductivity (OFHC) copper heat exchanger for UHV compatibility and good thermal conductivity at low temperatures. The sample stage is mounted off the heat exchanger and the whole assembly is surrounded by an OFHC copper radiation shield. It is radially compact to allow the sample to be positioned at the short focal lengths (typically 10 to 20mm) of the electron energy analyser used for photoelectron spectroscopy. For a detailed description of the liquid helium cooled manipulator see Teehan (1991).

3.2.3 Sample Heating and Cooling

The sample stage is shown in figure 3.2 and consists of two sections; (i) the top plate for holding the samples and (ii) the heater assembly. The sample itself is supported on a molybdenum spade and held in place by spot welded tantalum clips. This unit is then located on the top plate by sliding under some more

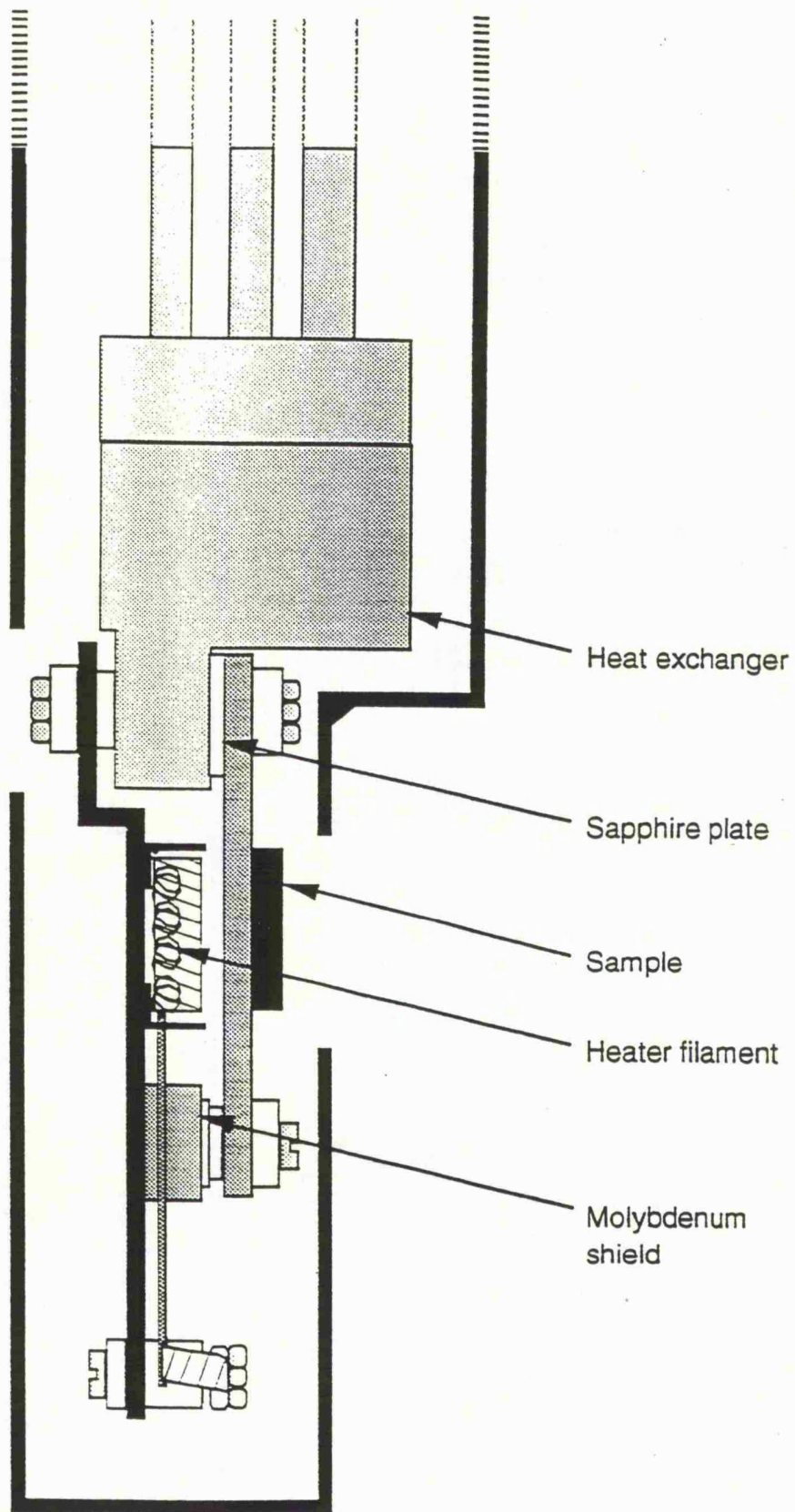


Figure 3.2 Schematic of sample stage used with the liquid helium manipulator.

tantalum clips. This design allows for easy transfer of samples without breaking the main chamber vacuum with only the sample spade needing to be replaced.

Both the sample spade and the top plate are machined from high purity molybdenum which outgasses little when heated to the high temperatures necessary during sample cleaning. The top plate is screwed to one side of the heat exchanger sandwiching between the two a 1mm thick polished synthetic sapphire plate. This material is an excellent electrical insulator but its thermal conductivity varies considerably with temperature, it insulates the heat exchanger from the sample plate when hot but provides good thermal contact between the two when both are cold. Behind the sample plate and bolted to the other side of the heat exchanger is the heater assembly. This is electrically isolated from the sample plate and heat exchanger with ceramics. Four electrical connections to the heater are made by feeding wires through small holes in the back of the radiation shield which connect to standard UHV manipulator feedthroughs on the top of the cryostat by going through the DPRF. Two of the connections supply power to a 0.2mm thoriaated tungsten wire filament, the other two connections are to the top plate, which is electrically isolated from the body of the manipulator, one is from a high voltage feedthrough and the other is the thermocouple connection. The filament is shielded to improve efficiency and all ceramics are protected by being placed out of line of sight or by use of a molybdenum shielding cup.

The sample can be heated radiatively by passing a current through the filament alone or by electron beam heating. In the latter the sample plate is biased to a

high positive voltage, typically 1kV, and electrons emitted from the hot filament bombard the rear of the sample plate thus heating it. The power requirements necessary for heating are 1kV, 6A filament current giving 60mA emission current. The temperature of the sample is monitored using a Chromel-Alumel thermocouple clamped to the top plate. The operating range of this thermocouple is 3K to 1640K which is ideal for the capabilities of the cryostat. Around the sample stage is a detachable OFHC radiation shield of all-welded construction. This shield is cooled by the cold helium gas returning from the heat exchanger and intercepts the vast majority of ambient radiation from the surroundings at room temperature.

3.2.4 Substrate Preparation

The substrates used in these experiments were highly oriented pyrolytic graphite (HOPG) supplied by Le Carbone as 99.99% purity pseudomonocrystal plates with dimensions 10.0mm x 10.0mm x 1mm. HOPG is a very inert material and relatively atomically flat. The substrates were cleaved in air as soon as possible prior to loading into vacuum, no pre-UHV processing is necessary. After evacuating the chamber to UHV the samples were heated to 1000K for thirty minutes and subsequent photoelectron spectra showed no signs of O, N and S contamination on the substrate. However occasionally a small level of Si contamination was observed in the photoelectron spectra. This is a 'known' contaminant of the manufacturing process and impossible to remove if present. After regular 'flashing' of the sample to 800K the pressure rise is limited to 1×10^{-8} mbar recovering to 5×10^{-11} mbar after 2-3 minutes.

3.2.5 Metal Vapour Sources

Mn and V films were deposited from compact metal vapour sources based on the design of Taylor and Newstead (1987). Two types of source were used; a Knudsen cell evaporator and an electron beam evaporator. They fit onto standard 70mm conflat UHV flanges and incorporate an integral shutter and a cryogenic shield, for use with water or liquid nitrogen. Both designs avoid direct line of sight from the filament to the sample. Thorough outgassing of the evaporator is crucial for UHV operation. After bakeout the evaporator will be run typically for three hours and then allowed to cool before connecting the coolant flow. Normal evaporation can then commence at a chamber pressure of 2×10^{-10} mbar or below.

Knudsen Cell Evaporator

Figure 3.3 is a schematic of the Knudsen cell evaporator used for the deposition of Mn islanded films. The evaporant, 99.98% pure Mn flake (supplied by Goodfellow) is loaded into a 1cm^3 alumina crucible around which is wound a 0.25mm diameter tungsten wire filament. The temperature is monitored with a Chromel-Alumel thermocouple located at the open end of the crucible. The vapour flux is collimated by a cap at the end of the crucible assembly and can be interrupted by a shutter which is fitted to a rotary drive. The filament is heated by a Farnell TS70 stabilised DC power supply and under operating conditions can remain at a constant temperature to within $\pm 2\text{K}$ for many hours. Typical conditions for the evaporation of Mn are an input power of 120 watts

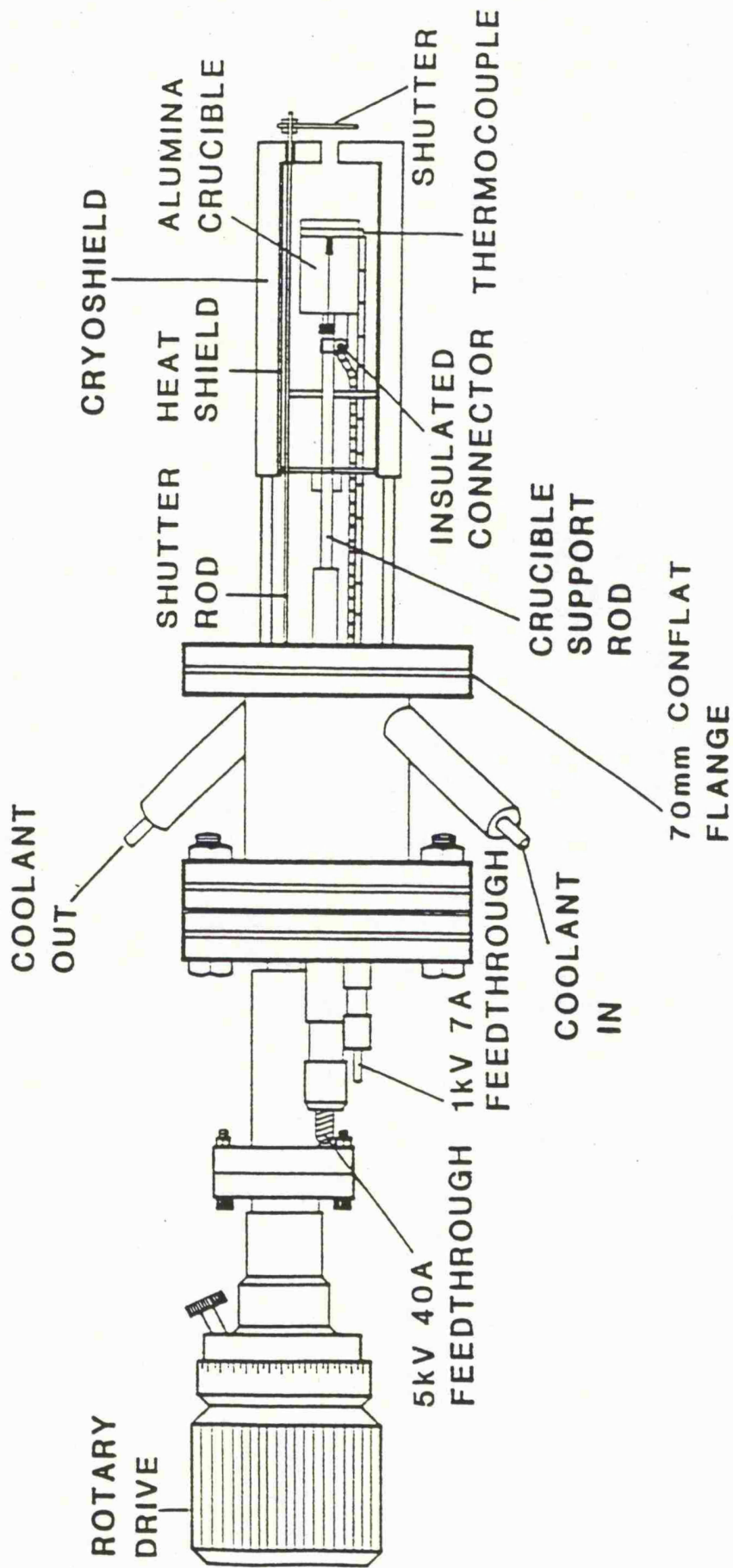


Figure 3.3 Schematic of Knudsen cell type vapour source.

giving a deposition rate at the sample of approximately one monolayer in 12 minutes.

Electron Beam Evaporator

Figure 3.4 is a schematic of the electron beam evaporator used for the deposition of V films. The evaporant, 99.8% pure V metal is supplied by Goodfellow in the form of a rod. It is clamped into a stainless steel tube and biased through a high voltage feedthrough. A filament of 0.2mm diameter thoriated tungsten wire is wound into a loop of diameter 22mm around the end of the rod. It is attached, through stainless steel rods to two small UHV feedthroughs. An earthed tantalum shield is placed between the metal and the filament to ensure that only the end of the rod is bombarded and to avoid direct contamination of the rod by the filament. The filament current is controlled by an emission stabiliser unit, which employs a feed-back system to hold the emission current at the selected level. Typical operating conditions are an applied positive potential of 2.5kV, 7A filament current giving an emission current of 12mA. This gives a deposition rate at the sample of one monolayer in approximately 6 minutes.

3.2.6 The Leicester University Mesoscopic Particle Source (LUMPS)

For the *in-situ* deposition of ready made clusters in UHV a gas aggregation source has been designed and constructed at Leicester, it is shown in plate 3.3 and schematically in figure 3.5. The system consists of a gas cell, in which the metal is evaporated, and a series of differentially pumped cooled apertures

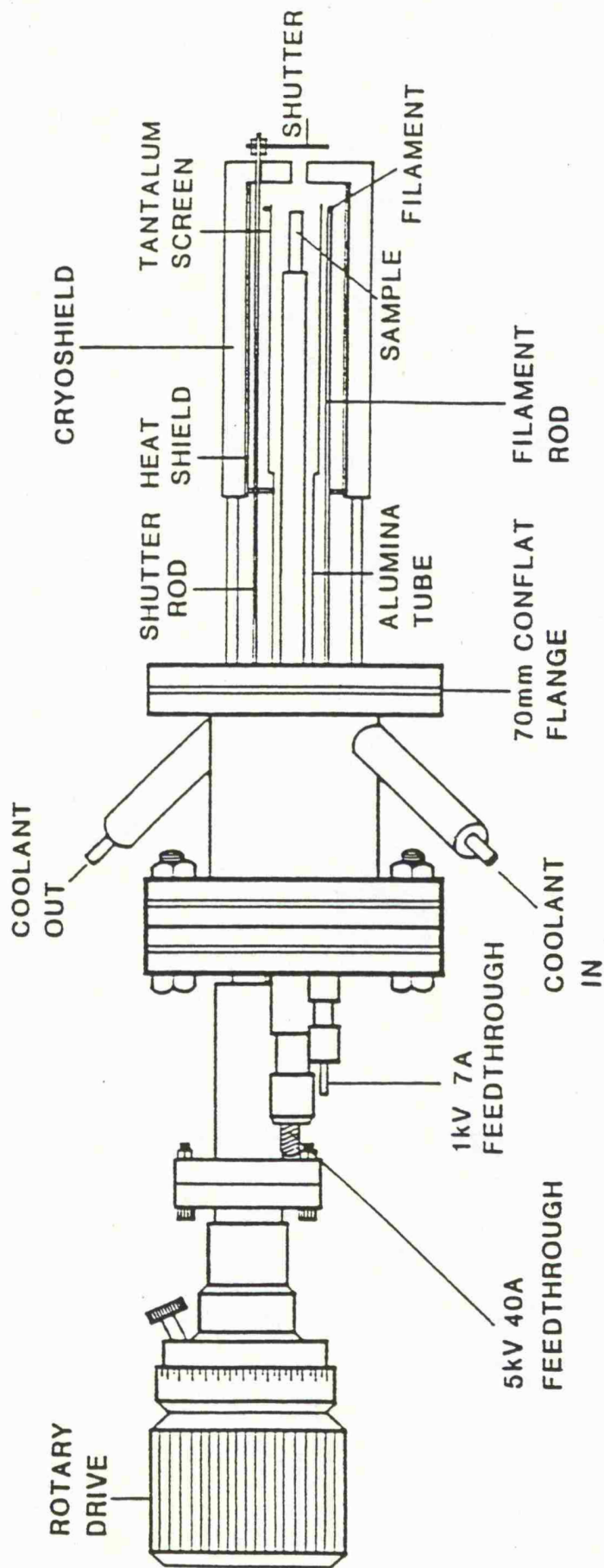
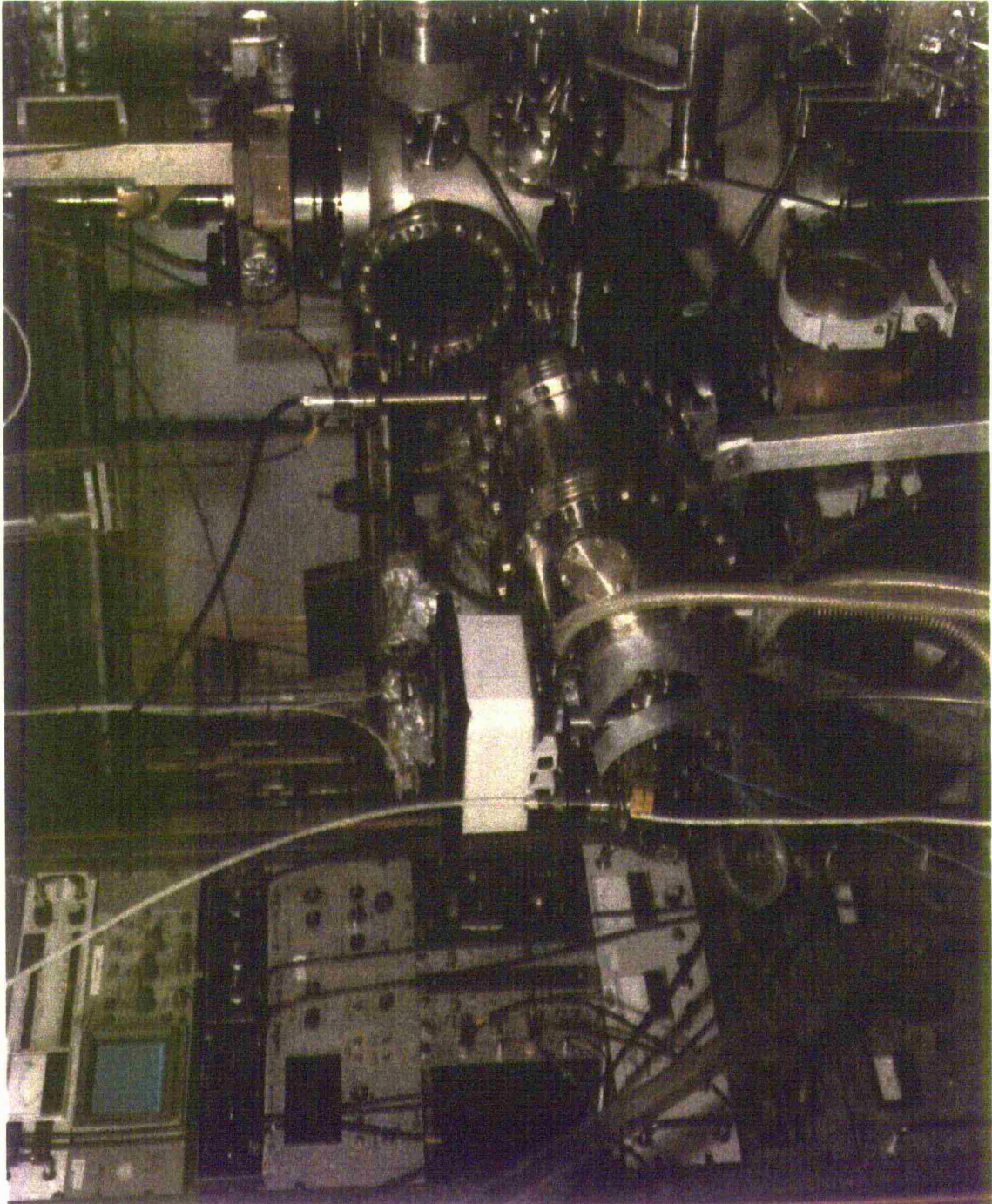


Figure 3.4 Schematic of electron beam type vapour source.

Plate 3.3 Photograph of the Leicester University Mesoscopic Particle Source (LUMPS).



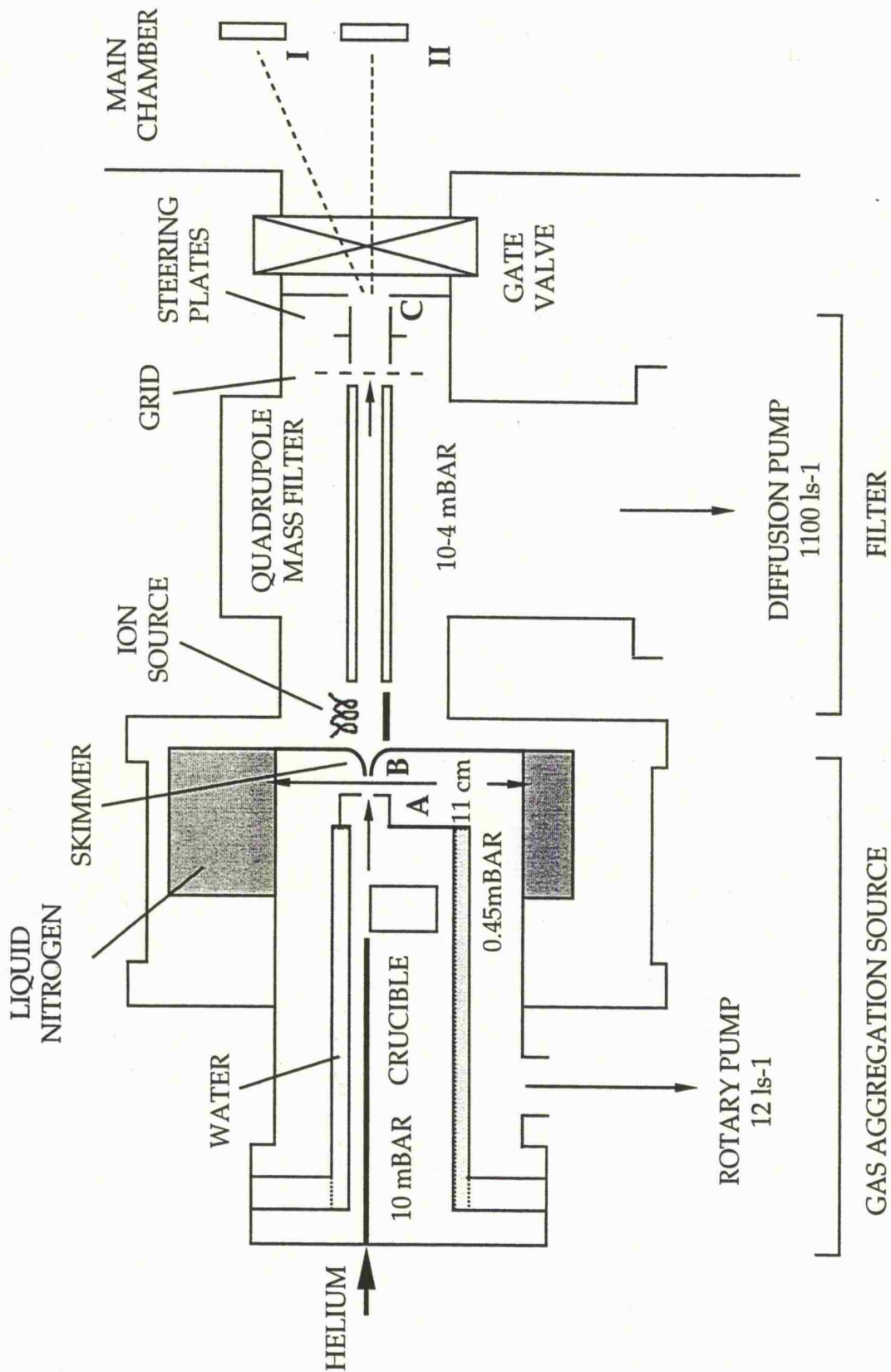


Figure 3.5 Schematic of the Leicester University Mesoscopic Particle Source (LUMPS).

between which the clusters are formed, ionised, mass-selected with a quadrupole filter and steered into the UHV environmental chamber. The gas cell contains the crucible, a niobium carbide (NbC) coated graphite crucible, and a boraelectric heater which is a graphite element with a pyrolytic boron nitride (PBN) coating, both were supplied by BN products UK. Metal (99.98% pure Mn flake supplied by Goodfellow) is evaporated from the crucible into the gas cell which contains a bath gas of helium at a pressure of 10mbar. The heater assembly, shown in plate 3.4, is surrounded by tantalum heat shields to improve efficiency and the surrounding region is water cooled to absorb the radiated heat. The metal atoms and helium carrier gas then pass into a liquid nitrogen cooled region. The mean free path at this pressure is short and the atoms undergo many collisions losing their thermal energy as they condense into clusters. The mixture then exits the cell through a 1mm aperture into a region pumped by an Edwards E2M40 rotary pump with a pumping speed at the aperture of 12ls^{-1} maintaining a vacuum of 0.45mbar. The condensed metal clusters and gas pass through a liquid nitrogen cooled copper skimmer (supplied by Beam Dynamics Incorporated, USA), with an orifice diameter of 1.0mm, into a chamber pumped by an Edwards 160MM Diffstak. This maintains a pumping speed at the skimmer of 1100ls^{-1} which gives a vacuum of 10^{-4} mbar in the chamber. It is in this chamber that the cluster beam undergoes ionisation, mass filtering and steering.

Mass Filter

The ionisation source, mass filter and steering plates are shown in plate 3.5 and have been designed to fit together as a single unit to allow accurate

Plate 3.4 Photograph of LUMPS heater assembly.

Plate 3.5 Photograph of the combined ion source, quadrupole and steering plates assembly.

alignment along the axis of the aperture and skimmer orifice. The ionisation source, supplied by Metri-Tech UK, has axial geometry and is a standard design found in commercial RGAs. The entrance to the ionisation source is placed as close to the skimmer exit as possible. The ionised clusters and carrier gas then pass into the quadrupole through a 1 mm diameter aperture where they are mass selected. After exiting the quadrupole through a similar size aperture they are steered using electrostatic plates into the environmental chamber through a final aperture of diameter 8mm. The quadrupole and its power supply were designed and constructed at Leicester. The quadrupole rods are precision ground to a diameter of 6.32mm with a tolerance of ± 0.01 mm and are 150mm long which gives a resolving power of about 100. The filter has variable frequency control over the range 125KHz to 1MHz, which gives a selectable mass range up to 10^6 amu.

3.3 Experimental Measurements

All of the experiments were performed using synchrotron radiation from the SRS at Daresbury Laboratory. The ability to tune the photon energy and high intensity of the beam makes the use of synchrotron radiation very desirable for surface science experiments.

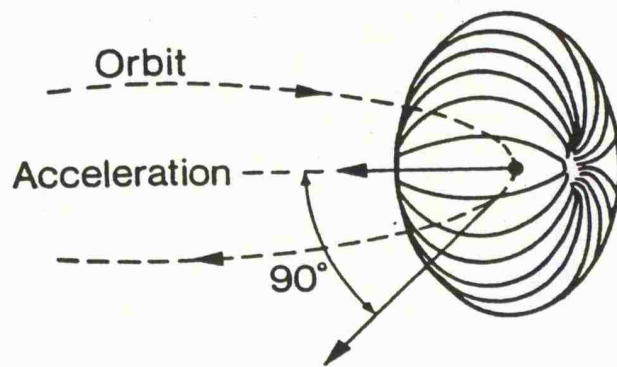
3.3.1 Synchrotron Radiation

When an electron is travelling in a circular orbit it is radially accelerated. This results in a characteristic radiation pattern which is dependent on the energy of

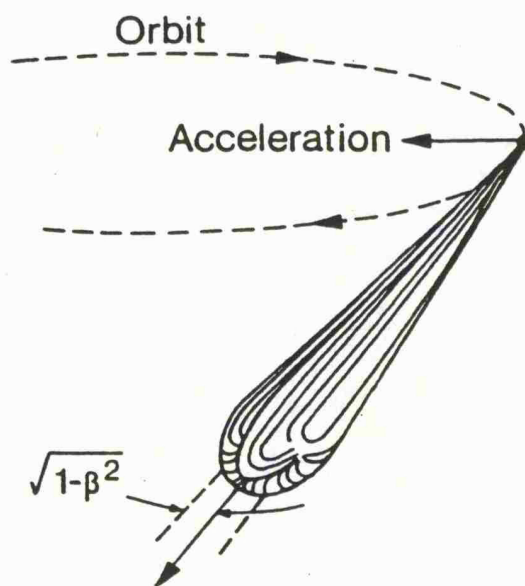
the electron. Figure 3.6(a) shows the toroidal radiation pattern emitted by a low energy electron. The SRS, however, operates at an energy of 2 GeV and the velocity of the electrons in the storage ring is relativistic. In this case a narrow cone of radiation is produced, Figure 3.6(b), with strong collimation in the instantaneous direction of flight, this is synchrotron radiation. There is almost 100% linear polarisation of the radiation in the plane of the orbit.

3.3.2 Beamline 6.1 - Grazing Incidence Monochromator

All the measurements reported in this thesis were performed on photoemission beamline 6.1 of the SRS at Daresbury Laboratory, shown schematically in figure 3.7. The synchrotron radiation has a continuous spectrum and before it can be used in a photoemission experiment it must undergo monochromatisation. Beamline 6.1 uses a grazing incidence monochromator (GIM), described by Howells *et al* (1978) which is based on the original geometry of Miyake *et al* (1969). It consists of a Au-coated plane grating made from spectrosil (fused quartz) and a Pt coated SiC spherical mirror which rejects higher spectral orders by selective reflections. Useable photon flux is delivered in the energy range 30-280eV with the peak output at around 150eV. A pre-mirror deflects the synchrotron radiation horizontally into the GIM where the required photon energy is selected. The monochromatic beam is then defined by post-monochromator slits which affect the beamline resolution. After the exit slits a Au-coated ellipsoidal focusing mirror deflects the light to bring it to a focus at the centre of the experimental chamber. This results in a typical beam intensity at the sample of 10^{11} photons s^{-1} with a 0.3% bandwidth and a spot size vertically of 1mm and horizontally 3mm.



(a) Non-Relativistic Case ($\beta \ll 1$)



(b) Relativistic Case ($\beta \approx 1$)

Figure 3.6 Angular intensity distributions of (a) slow and (b) relativistic electrons in a circular orbit (Tomboulain and Hartman 1956).

3.3.3 Photoelectron Detection

In a photoemission experiment the photoexcited electrons are emitted with a range of energies which can be detected by several types of charged particle energy analyser. In order to detect electrons of a particular energy a potential is applied to bring the electrons to the pass energy of the analyser. It therefore acts as a narrow pass filter with a band-width proportional to the pass energy. The resulting contribution to the sampled peak width can be reduced by using a smaller pass energy, but this in turn means a reduction in signal intensity. A spectrum is obtained by scanning the applied potential while keeping the pass energy of the analyser constant. In this work all photoemission measurements were made using one particular type of energy analyser, the concentric hemispherical analyser (CHA), described below.

Concentric Hemispherical Analyser

The CHA used in this work was a VSW HA-100 analyser with multi channel detection, shown schematically in figure 3.8. The photoemitted electrons undergo acceleration or retardation using a lens arrangement and they then pass into the analyser. This is comprised of two hemispherical surfaces with a potential applied between them. They are positioned concentrically with the inner sphere being positive and the outer one negative. Only electrons which enter with the analyser pass energy will emerge from the hemispheres. They are then focussed through another lens system onto the detector, which consists of chevron channel plates with sixteen anode strips allowing simultaneous multichannel detection.

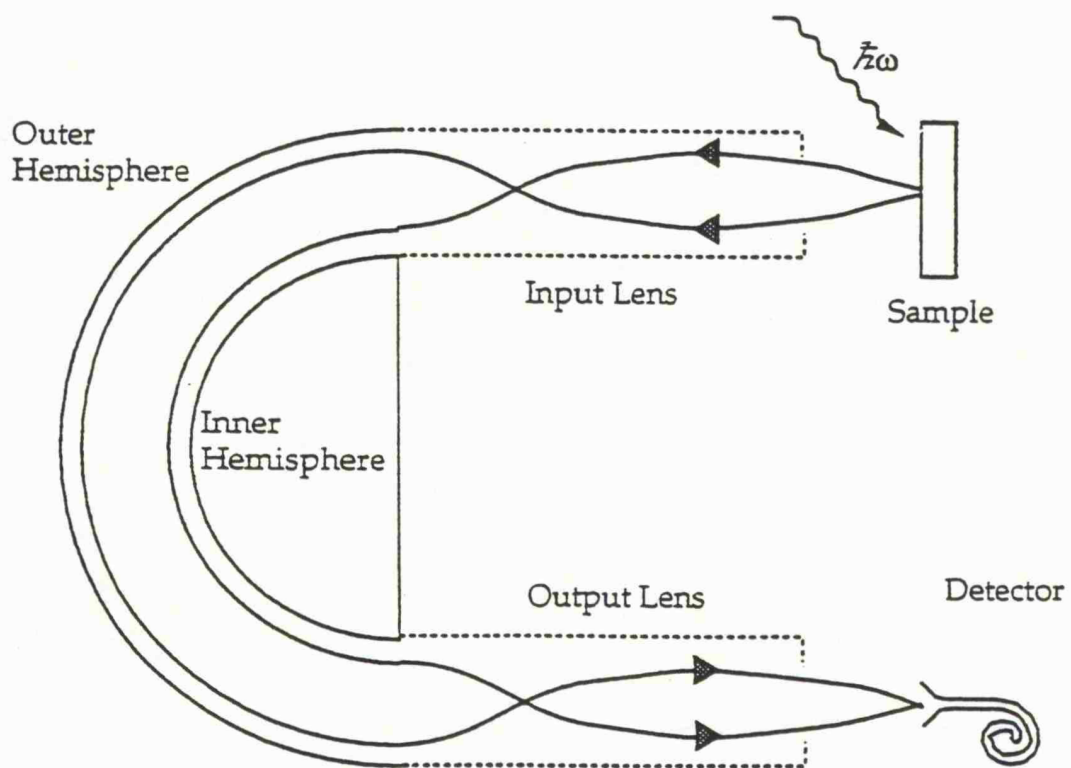


Figure 3.8 Schematic of CHA.

Chapter 4

The Growth of Mn on HOPG

- 4.1 Introduction
- 4.2 Experimental
- 4.3 Analysis Procedure
- 4.4 Results and Discussion
- 4.5 Summary

Chapter 4

The Growth of Mn on HOPG

4.1 Introduction

Deposition in UHV of many metals onto materials such as the alkali-halides, graphite, mica and many insulators exhibit the Volmer-Weber growth mode. Robins (1976), (1979), Harsdorff (1976), (1982), Kern *et al* (1979), Stenzel *et al* (1980), Fan *et al* (1988), Ganz *et al* (1988), Ganz *et al* (1989), Meunier and Henry (1994) and Xu *et al* (1994) present a selection of experimental and theoretical investigations. Venables *et al* (1983) presents a review of the nucleation and growth processes occurring in thin film formation. More specifically vacuum evaporation in UHV is a simple and proven in-situ method for producing mesoscopic transition metal particles, making the particles accessible for study with the powerful microscopic probes developed in surface science using synchrotron radiation. Techniques such as photoelectron spectroscopy and photoelectron diffraction are able to provide detailed information on crystal structure, electronic and magnetic properties and a size dependent study using such probes can make significant progress in understanding these systems. Allied with any size dependent study there is a need to know the average size of the particles without having to remove the sample from UHV to perform an ex-situ measurement and risking contamination. A technique has been developed to make in-situ measurements and the growth and morphology of islanded Mn films on graphite has been investigated from the earliest stages through to a thick film. The technique is based on surface reflectivity in the extreme ultraviolet region (XUV) and involves comparing the measured

reflectivity of the growing film in the wavelength range 6-36 nm with a calculation of the clean substrate reflectivity modified by the overlayer. The calculation is performed as a function of three parameters, the size and shape of the islands and the coverage.

The investigation of the optical properties of inhomogeneous films has a long history. It was Faraday (1857) who first speculated that the brilliant colours exhibited by very thin silver and gold films viewed in white light was due to the discontinuous nature of the films. Successive experimental investigations by Sennett and Scott 1950, Clegg 1952 and Rouard and Bousquet 1969 have confirmed this result. Mie (1908) presented the general solution to absorption and scattering of light by spherical particles, detailing the significance when the wavelength of the light is of the same order of magnitude as the particle size and explaining the presence of anomalous absorption bands observed in colloids. Consequently features are also observed in the reflectivity of deposited inhomogeneous films which aren't seen in the bulk or continuous layers and are highly sensitive to film morphology. Maxwell-Garnett (1906) set up a theoretical model to explain Faraday's result by treating the discontinuous film as a section cut from a composite medium containing a dispersion of small metallic spheres.

As discussed in chapter 2.3 the model used in these calculations is based on the theory of Jarrett and Ward (1976), which in turn has its foundations on Maxwell-Garnett's model but includes improvements by David (1937) and Yamaguchi (1962). The former proposed representing the particles by ellipsoids of revolution which are characterised by the ratio of their half axes, and the

latter arranges these ellipsoids on a surface and deals with the specific interaction which occurs between the two-dimensional array of dipoles.

Jarrett and Ward (1976) and McKenna and Ward (1981) have used visible light to study the shapes of gold and silver islands grown on glass and mica substrates showing that with increasing film thickness the particle size increases are accompanied with a decrease in the number of particles due to coalescence or preferential growth of larger particles. Mie theory has been used to characterise the surface roughness of tin oxide films by Schade and Smith (1985) and Binns and Bayliss (1989) used a model based on Mie theory to obtain the average size of silver islands grown by vacuum evaporation on graphite by considering the film as an array of independent spheres. Measurements have been extended into the extreme ultra-violet (XUV) by Binns *et al* (1992) to determine the average island size of mesoscopic chromium and vanadium islands on graphite.

4.2 Experimental

All measurements were made using the grazing incidence monochromator (GIM) on beam line 6.1 of the synchrotron radiation source (SRS) at Daresbury laboratory, described in chapter 3.3. This provides usable light flux in the spectral range 35 to 200 eV (35.42-6.20 nm). Photons were incident on the sample at a grazing angle of 22.5° and the specular reflectivity of the sample was measured using an EMI nude photomultiplier assembly with CuBe dynodes. A photon energy of 97 eV was used to monitor the reflected signal as a function of evaporation time. Growth was interrupted at 3 minute intervals

to carry out reflectivity scans over the photon energy range 35-200 eV for the first 60 minutes after which 10, 15 and 30 minute intervals were used. For the duration of the experiment the sample temperature was maintained at 423 K.

The films were deposited using a Knudsen cell vapour source described in chapter 3.2.5. The chamber base pressure was 2×10^{-11} mbar and was always less than 2×10^{-10} mbar during Mn deposition, recovering to the base vacuum within a few minutes of the deposition being interrupted. The highly oriented pyrolytic graphite (HOPG) substrates were cleaved ex-situ and heated to 1000 K for 30 mins in UHV to remove any residual gas. Photoemission measurements showed small traces of silicon present on some of the substrates prior to the growth of Mn films. The spectral dependence of the reflectivity of the clean substrates in this case was identical to those with no trace of contamination so the silicon produces no optical effect though it may perturb the characteristics of the film growth. The stability of the detector response was checked prior to each scan and the system geometry was such that measurements and depositions could be carried out without moving the sample.

4.3 Analysis Procedure

The data was analysed using the theoretical model described in chapter 2.3 which considers the overlayer as continuous with an effective refractive index corresponding to an inhomogeneous film of identical ellipsoids. Required as input by the model are optical constants for graphite and Mn over the spectral range in consideration (6-35 nm). For graphite a complete set of data is reported over the whole spectral range by Hagemann et al. Mn data is reported over

most of the range by Sonntag *et al* (1969), with gaps filled by Kramers-Kronig integrals of data from Johnson and Christy (1974), Girouard and Van Truong (1984) and Henke *et al* (1993).

The reflectivity $R(\lambda)$ was obtained from the reflected signal from the covered substrate, $I(\lambda)$, using the relation :

$$R(\lambda) = \frac{I(\lambda)}{I_0(\lambda)} R_0(\lambda) \quad (4.1).$$

Where $I_0(\lambda)$ is the signal from the clean substrate and $R_0(\lambda)$ is the reflectivity of graphite calculated from the measured optical constants. The spectral variation of the incident light flux and detector response is thus compensated for. The reflectivity determined using equation (4.1) has to be corrected for the second order flux from the monochromator which has been estimated by Bailey and Quinn from photoemission measurements of the Cu 3d band. The reflectivity was calculated for each growth and the fits were minimised as a function of three parameters: the film thickness, d , which in this model is related to the average island size; the ellipticity, b/a , which is a shape parameter and is the ratio of half axes of the ellipsoids; and the volume filling fraction, q , which is related to the coverage. The shape parameter was found to be the least significant of the three. In comparison to a two parameter fit using just q and d only marginal improvements were produced.

4.4 Results and Discussion

Figure 4.1 shows the measured reflectivity of a Mn film grown at 423 K as a function of evaporation time at a photon energy of 97 eV. This particular

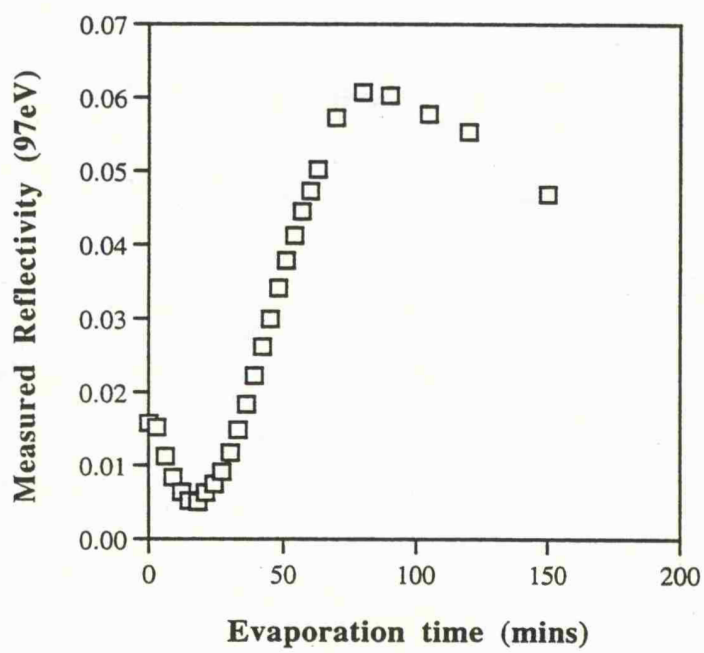


Figure 4.1. Reflectivity at 97 eV of a Mn film grown at 423 K as a function of Mn evaporation time.

energy corresponded to the point at which the increase in reflectivity of the thick Mn film relative to the clean graphite was greatest. The reflectivity curves for all the Mn growths exhibited the same general behaviour, a strong oscillation as expected due to interference within the film with increasing optical film thickness.

Figure 4.2 shows a selection of typical spectral scans from various coverages, specified by I/I_0 —the attenuation of the clean graphite reflectivity, along with the fitted curves from the model and the corresponding values for the volume filling factor (q) and film thickness (d) which gave the optimum fit, obtained through equations (2.8) to (2.18). As the coverage is increased through spectra (a) to (g) the fits become successively poorer, the explanation for this can be found in the figure itself. The feature due to the Mn $M_{II,III}$ absorption edge appears at a photon energy of approximately 50 eV, but as coverage is increased a discrepancy of about 5 eV is evident in the position of this feature between the measured and calculated reflectivities. It is believed to arise from a small discrepancy in the position of the edge in the published values of atomic cross sections from which the refractive index of Mn was calculated. The extent to which this discrepancy would affect the optimisation of the fit if the feature was shifted to the correct place is thought to be minimal and so the trends in the q and d parameters are thought to be reliable.

Figure 4.3 shows the product qd , representing the total amount of material on the surface as a function of evaporation time. At approximately 25 minutes the data exhibits a distinct change in the slope of qd , corresponding to a change in sticking probability. This signifies a change in the growth mode and is also

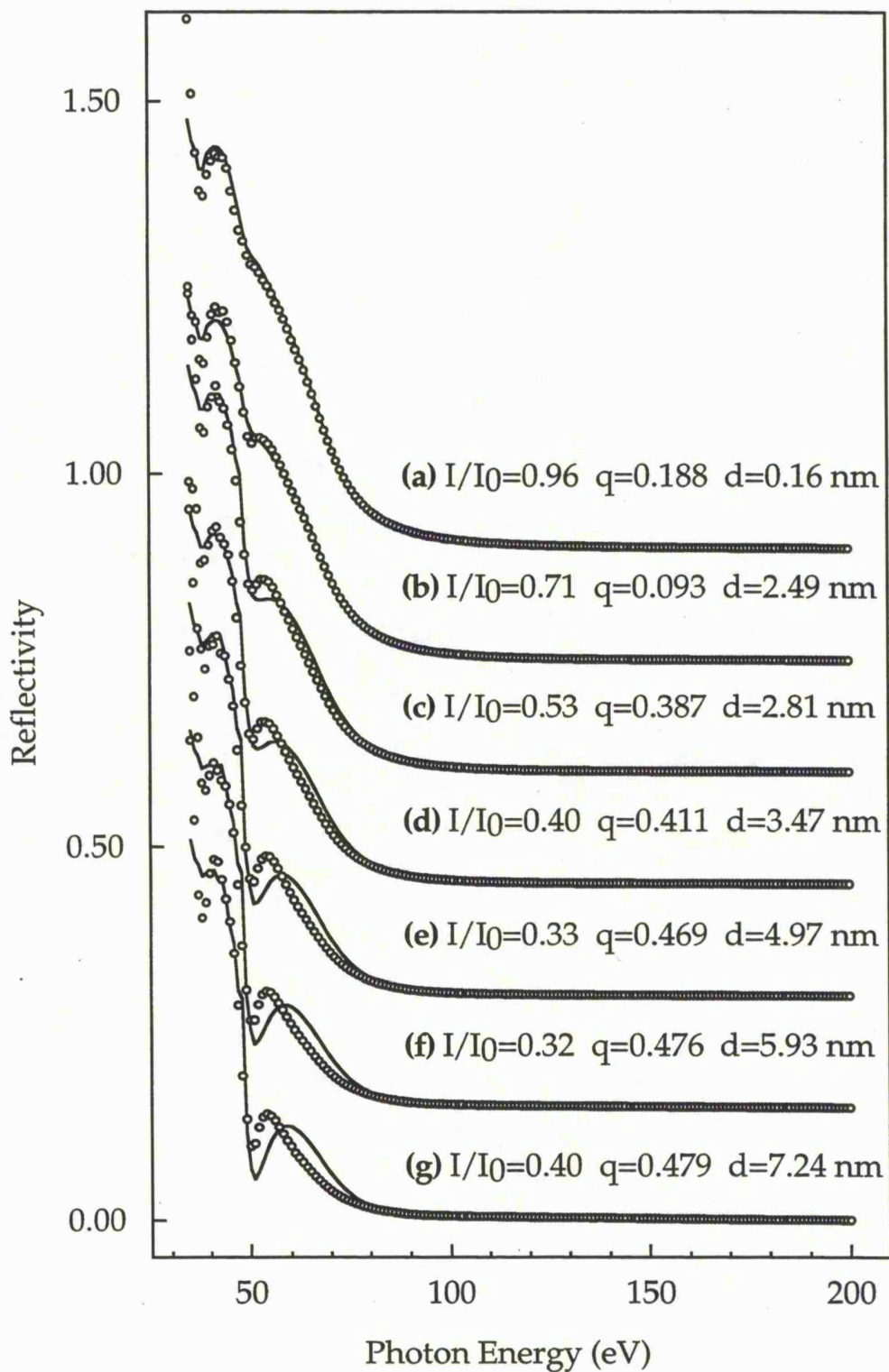


Figure 4.2. Measured (o) and calculated (—) reflectivities, of various coverages (specified by I/I_0 —the attenuation of the clean graphite reflectivity at 97 eV) Mn films showing values of film thickness (d) and volume filling fraction (q) giving the optimum fit.

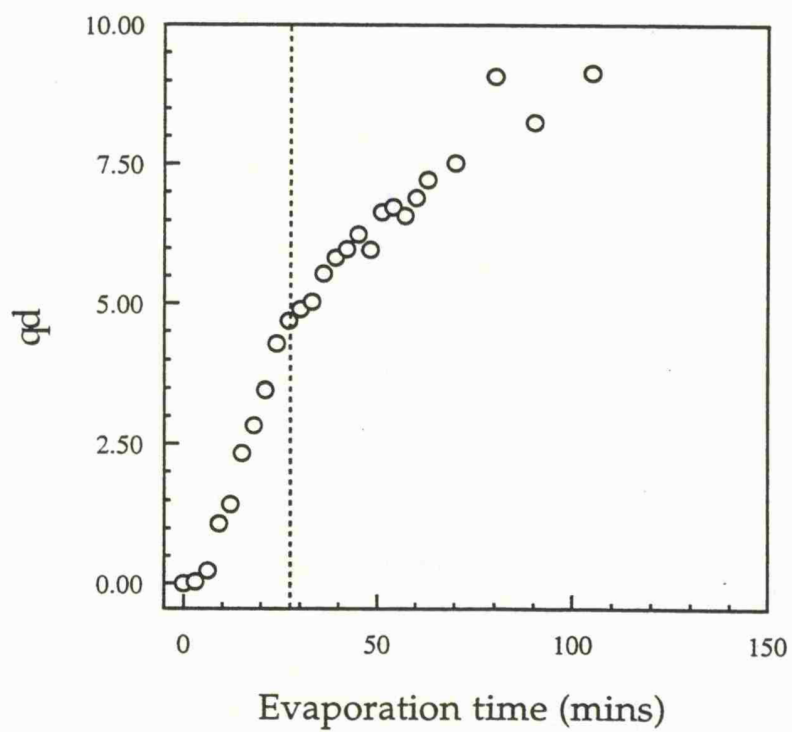


Figure 4.3 The product qd (proportional to the total amount of material in the film) of Mn films as a function of evaporation time. A change in sticking probability is indicated by the vertical line.

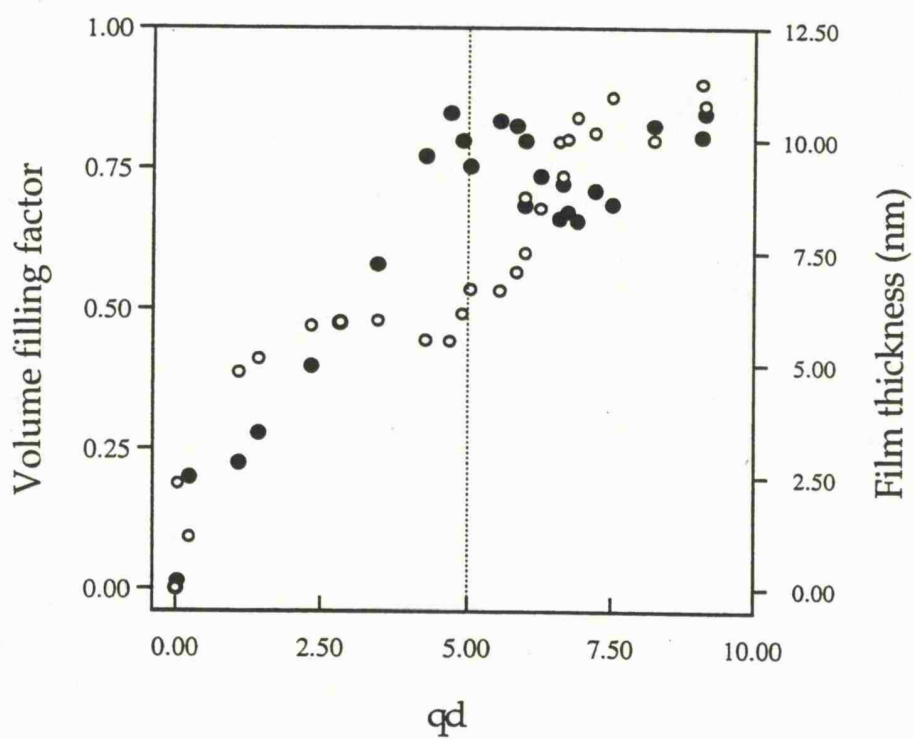


Figure 4.4 Volume filling factor (o) and thickness (•) of Mn films grown at 423 K as a function of coverage (qd).

evidenced by the data in figure 4.4 which shows both the volume filling factor (q) and film thickness (d) as a function of coverage (qd). During the initial stages of growth the film covers large areas of the surface very quickly depicted by the rapid increase in q up to nearly 0.5. At this point q levels off and is constant while d increases linearly indicating that the islands are growing vertically. This type of growth continues until the film thickness is about 10 nm at which point the coverage corresponds to the change in sticking probability observed in figure 4.3. The islands then stop growing vertically as shown by the flattening of the thickness curve and grow laterally indicated by the increase in q . Figure 4.3 also shows that there is a lower sticking probability for the latter growth mode.

Figure 4.5 shows the evolution of the shape of the islands and is consistent with the above results. The ratio of the island height to diameter is erratic at the start as expected but levels off to a small constant value as the film spreads to cover the surface indicating that the islands are flatter rather than taller. It then increases steadily corresponding to the columnar growth of the islands to a point where the island height and diameter are about equal after which the ratio decreases indicating the lateral growth at higher coverage. This change in the ratio from a steady increase to decrease also occurs at the same coverage at which the sticking probability was observed to change in figure 4.3.

The evolution of a metal island during film growth is determined by the relative magnitude of the flux of atoms onto and off of the island. The flux onto the island arises from two processes: that directly from the source and from atoms diffusing across the surface; the flux off the island occurs through

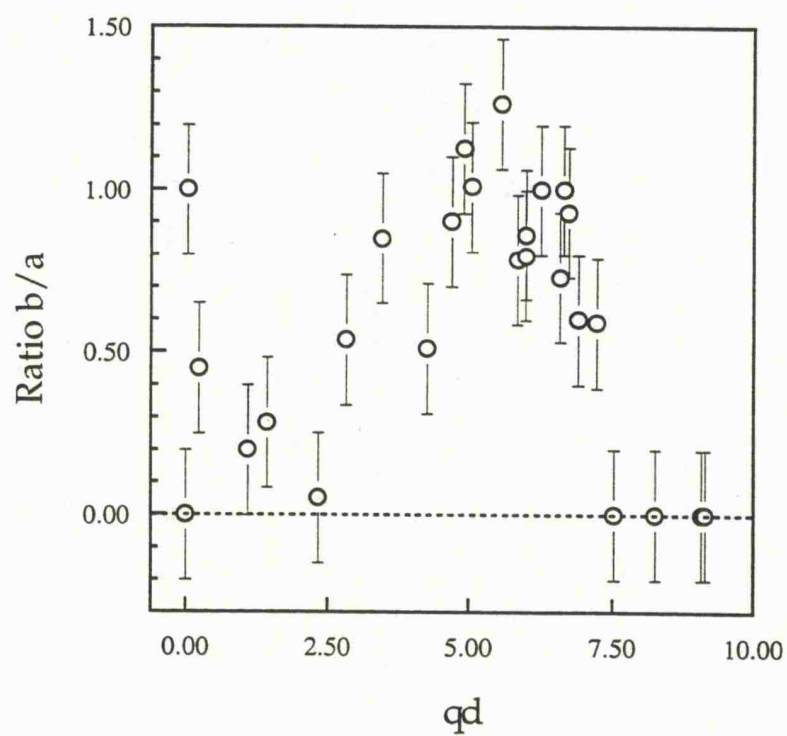


Figure 4.5. Ratio of semimajor to semiminor axes as a function of coverage (qd) of Mn films grown at 423 K.

evaporation from the surface. When the film is in the initial stages of growth a high proportion of the incident flux is directly from the evaporation source and the columnar growth of the islands is not unexpected. The change to lateral growth is hard to interpret in simplistic terms but must be due to an increased probability of atoms diffusing off the island surfaces and onto the substrate.

4.5 Summary

The growth of islanded Mn films at 423 K by vacuum evaporation onto HOPG has been investigated. With the combination of a realistic theoretical model to describe the measured XUV reflectivity of the islanded Mn films detailed information on their morphology has been found. The results for the Mn film growth are summarised below:

High coverage layer is formed initially , followed by vertical island growth, where

$$q = \text{constant and } d \propto t$$

Growth mode changes when the island height is the same as the width and lateral growth occurs, where

$$q \propto t \text{ and } d = \text{constant}$$

The growth is shown to occur in two distinct modes. To begin with the growing film rapidly covers a large proportion of the surface after which the islands grow vertically. The growth mode changes at a thickness of about 10 nm, when the island height and diameter are roughly equal, to horizontal growth and this is accompanied by a change in sticking probability.

The average particle sizes stated in the following chapters have been determined using the technique described above.

Chapter 5

A SPPED study of Mn on (HOPG) Graphite

- 5.1 Introduction
- 5.2 Experimental
- 5.3 Analysis Procedure
- 5.4 SPPED Results of Mn Films on (HOPG)
 - 5.4.1 Thick Mn Film
 - 5.4.2 Islanded Mn Film
- 5.5 Discussion
- 5.6 Summary

Chapter 5

A SPPED study of Mn on (HOPG) Graphite

5.1 Introduction

This chapter presents the work on the study of magnetic order in bulk and islanded Mn films on highly oriented pyrolytic graphite (HOPG) using spin-polarised photoelectron diffraction (SPPED), and represents the first such study on pure Mn. The idea of using photoemission to study magnetic order and the spin dependence of electron scattering was discussed briefly by Rothberg (1980) but it was Sinkovic and Fadley (1985) who developed the first quantitative theoretical analysis of the technique, which has subsequently been called SPPED, and Sinkovic *et al* (1985) who carried out the first experimental investigation.

In its simplest form the experiment makes use of multiplet split core-level photoemission lines as internally referenced sources of spin-polarised electrons, with no external spin detector then being necessary. Like the much more developed technique of PED without spin resolution, SPPED will be primarily sensitive to the first few spheres of neighbours surrounding an emitter. High surface sensitivity results from the fact that SPPED must be carried out at electron kinetic energies of 50-150 eV, in order to generate sufficiently strong magnetic scattering for detection, Sinkovic and Fadley (1985). It is reasonable to assume also that the photoelectron diffraction event captures the sample in a given magnetic state because spin fluctuations have a time constant about 6 orders of magnitude slower than a scattering event

(approximately 10^{-16} to 10^{-17} seconds) and no spin rotation can be expected in the time it takes the photoelectron to leave the emitter and scatter. As mentioned in chapter 2.4, for the 3d transition metals photoemission from the 3s level is the easiest case because of the simple doublet structure and the relatively large multiplet splittings. The quantity of interest in SPPED is the spin asymmetry, S , which has been defined by Sinkovic *et al* (1985) as

$$S = 100 \left[\frac{(R_{LT} - R_{HT})}{R_{HT}} \right] (\%).$$

Where R_{HT} and R_{LT} are the ratio of the multiplet peak intensities at high and low temperature respectively, HT is a temperature sufficiently high such that all magnetic order is lost and LT is any temperature below HT. Above the bulk ordering temperature the system exists in an intermediate magnetic state before encountering a high temperature transition where it becomes paramagnetic. In this paramagnetic region the ratio remains constant as the temperature is increased. So for 3d transition metals S is the intensity ratio of the spin-up relative to the spin-down 3s core level photoelectron signals normalised to the high temperature limit as a function of temperature. Experimental studies have been carried out by Sinkovic *et al* (1985) on KMnF_3 , a highly ionic crystal with a perovskite structure. The results are shown in figure 5.1(a), and by Hermsmeier *et al* (1989) on single crystal MnO in figure 5.1(b). Both are antiferromagnetic in the bulk with ordering temperatures of 88 K and 120 K respectively. By monitoring S as a function of temperature a steady decrease with increasing temperature is expected from theoretical spin-spin correlation behaviour. Instead abrupt changes were observed in S , at

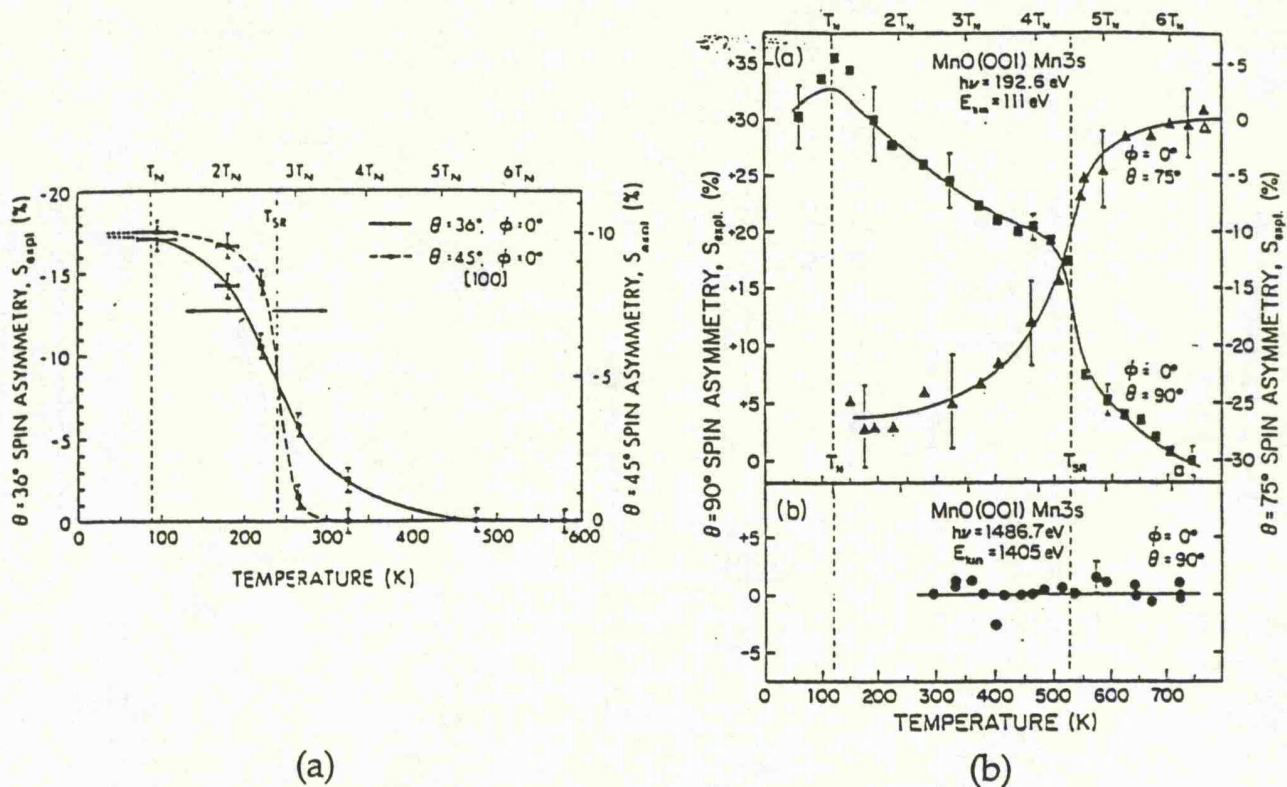


Figure 5.1. Experimental spin asymmetry results from (a) $KMnF_3$, after Sinkovic *et al* (1985) and (b) MnO , after Hermsmeier *et al* (1989).

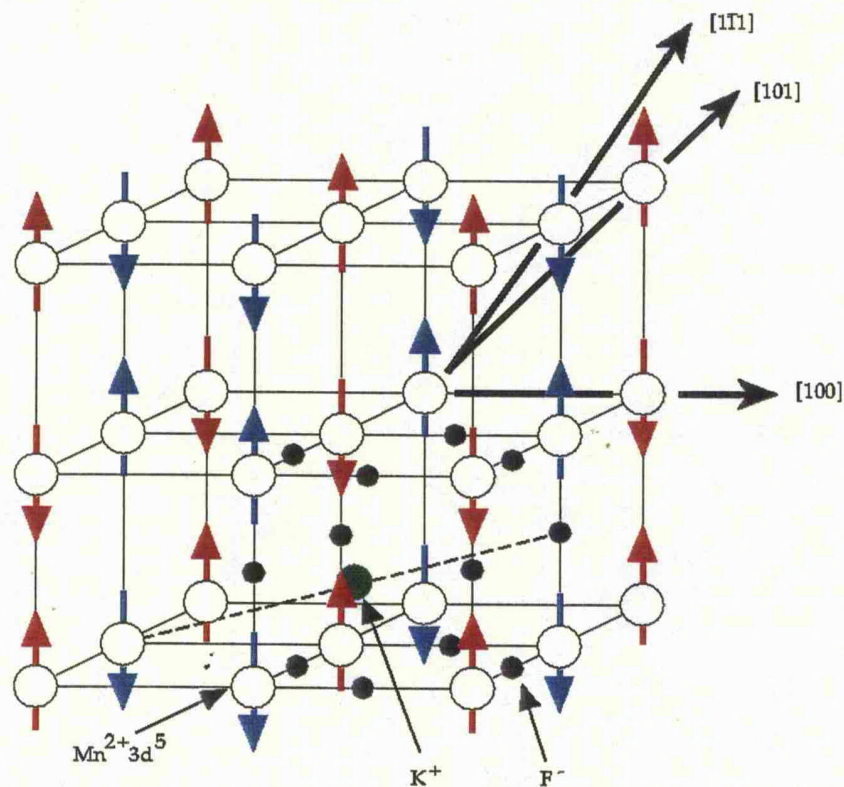


Figure 5.2 The perovskite structure of $KMnF_3$ with the antiferromagnetic ordering of Mn^{2+} ions occurring below $T_{N_{el}} = 88K$.

approximately 240 K for KMnF_3 and 540 K for MnO , well above their respective bulk ordering temperatures.

This result was shown to be direction dependent, figure 5.2 shows the KMnF_3 crystal structure and it is clear that emission along different directions should involve anisotropic spin effects. Sinkovic and Fadley (1985) performed single scattering cluster calculations of the degree of spin asymmetry in photoelectron intensity of a polar angle scan over a (110) oriented surface of KMnF_3 , showing significant angular-dependent changes in S . This allowed the SPPED effect to be maximised with a particular choice of emission direction, producing measured asymmetries of up to 17% for KMnF_3 and 25% for MnO . These measured values were somewhat greater than the maximum degree of asymmetry of 13% predicted by the calculations of Sinkovic and Fadley (1985), although general trends predicted for changes in S were observed experimentally. More specifically the slopes in S were found to vary in sign with emission direction at the transition temperatures for both KMnF_3 and MnO , but that the transitions occurred at the same temperatures and the percentage change at the transition was of a similar magnitude 10%-15% in each crystal.

SPPED measurements have also been attempted by Johnson *et al* (1987) on NaCrS_2 , with an investigation of the multiplet split Cr 3s core level. The results were compromised, however, by the complex nature of satellite structure in the vicinity of the core levels and by the fact that without any calculations of the spin asymmetry it was not known which photoelectron emission direction would produce an appreciable effect. The relative closeness in binding energy of the rather weak Cr 3s levels to the Na 2s peak was also

found to complicate the analysis with regards to background subtraction. It was concluded, though, that spin-dependent diffraction effects resulting from interactions with locally ordered spin arrays of Cr atoms *were* present in the Cr 3s spectra of NaCrS₂, but an accurate numerical determination of the asymmetry factor was not possible.

Spin-dependent photoelectron diffraction has also been observed by Waddill *et al* (1994) for Fe films on Cu(001). Circularly polarised x-rays were used to produce spin-polarised photoelectrons from the Fe 2p doublet and intensity asymmetries in the 2p_{3/2} level were observed as a function of photon energy, with a peak asymmetry of 5%. Strong angular effects were demonstrated in the spin-dependent scattering from experimental results for scattering along two high-symmetry directions and the results were well described by spin-polarised photoemission multiple-scattering calculations. This work expressed some concern over the validity of other work described above, due to the definition of the nature of the intrinsic 3s polarisation, and so measurements were performed in mirror planes to determine if the observed spin asymmetry was due to spin-dependent diffraction.

However, Hermsmeier *et al* (1988) compared core level photoelectron spectra from atomic Mn with corresponding spectra from the solid compounds MnF₂ and MnO to investigate the exact nature of the multiplet splittings and final-state extra-atomic processes involved. They found that the multiplet structures were essentially identical, strongly supporting the idea of a spin-resolved 3s spectrum. This intra-atomic, unscreened interpretation of the multiplets has been confirmed in a theoretical analysis by Kinsinger *et al* (1990),

in which it was concluded that final-state screening effects are only important for 3d compounds containing Ni²⁺ and Cr²⁺.

5.2 Experimental

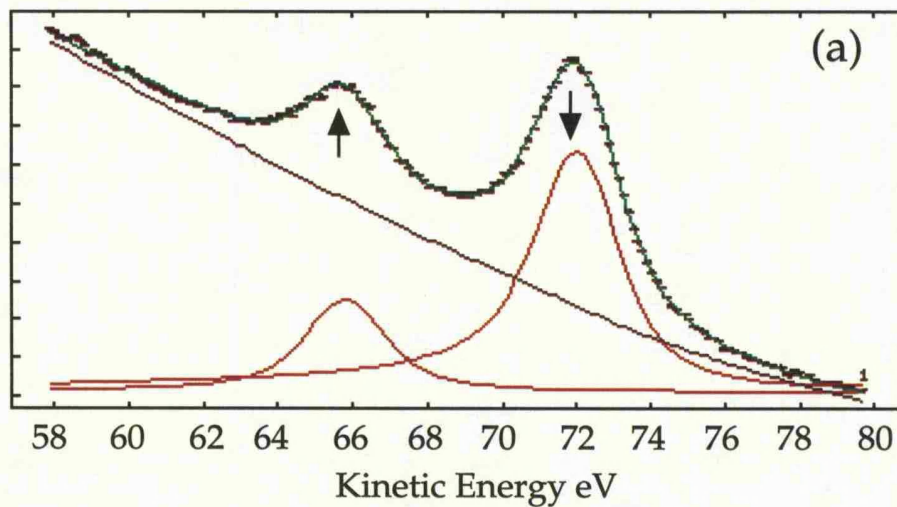
Photoemission spectra were recorded on beamline 6.1 of the Synchrotron Radiation Source (SRS) at Daresbury Laboratory. The Mn samples were prepared *in situ* by evaporation from a water-cooled Knudsen cell source onto HOPG graphite. The substrates were cleaved in air and, prior to deposition, they were heated to 1000 K for 30 minutes under UHV conditions. The chamber pressure during data collection was 1×10^{-10} mbar or better, rising to 2×10^{-10} during sample deposition. Photons were incident on the sample at an angle of 45° to the surface normal with electrons collected at the specular position by a VSW HA100 electron energy analyser employing 16 channel detection. The analyser was used in Fixed Analyser Transmission mode (FAT 10) with the combined resolution of the monochromator and the analyser estimated at 0.45 eV from detailed Fermi level measurements. Mn 3s core level photoelectrons were collected in the kinetic energy range 46-86 eV with a photon energy of 160 eV, while the valence band was monitored with a photon energy of 120 eV over the kinetic energy range 80-120 eV to check for the onset of oxygen contamination.

5.3 Analysis Procedure

Mn 3s photoelectron spectra were analysed using a Doniach-Sunjc line shape fitting routine to give the intensity, width and asymmetry of each contribution

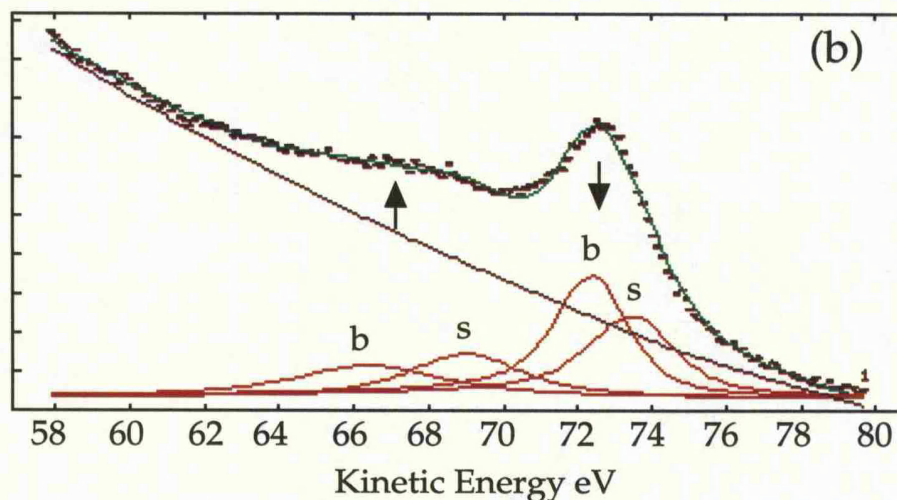
with the background modelled by a Tougaard contribution (Tougaard 1986) plus a polynomial. The routine fits Lorentzian lineshapes to account for lifetime broadening convoluted with a Gaussian to account for instrumental resolution. Starting parameters of the peak positions, heights, FWHM and a value for the width of the convoluting Gaussian are required. These parameters are then allowed to vary within some limits and the routine will find a best fit to the data based on a reduced chi-squared test. The spectra were first fitted as a function of the width of the convoluting Gaussian to find the minimum chi-squared. A value of 1.4 eV produced the best fit to the data, however, the experimental resolution was measured at only 0.45 eV, this discrepancy is probably to compensate for a departure of the actual lineshape from that predicted by the Doniach-Sunjic model.

Figure 5.3 shows typical Mn 3s photoelectron spectra, recorded at 40 K, of (a) a thick continuous Mn film and (b) an islanded Mn film where the average islanded size was 6 nm, with the corresponding output from the lineshape fitting routine. The thick film data were analysed by fitting two components, one to each peak, while the islanded film data were analysed by fitting four components, i.e. two pairs of spin-down and spin-up contributions. One spin-down and spin-up pair were assigned to a contribution from the bulk and the other pair to a contribution from the surface. The justification for this approach is provided from a couple of sources. Firstly, and very importantly, for (spherical) particles of this particular dimension the surface to volume ratio is 23% and one therefore expects a greater proportion of the photoelectron signal from the surface relative to the bulk. Secondly, figure 5.4 compares some background subtracted 3s photoelectron spectra from the islanded film with



	Position	Height	Width	Asymmetry	Area
peak 1 :	72.18	55797	1.8	0.09	277451
peak 2 :	65.89	20257	1.7	0.02	86475

Chi squared = 1.48



	Position	Height	Width	Asymmetry	Area
peak 1 :	73.60	10125	1.9	0.08	47005
peak 2 :	72.51	10952	1.4	0.08	58996
peak 3 :	69.01	8523	3.0	0.00	28504
peak 4 :	66.41	9218	4.5	0.00	27311

Chi squared = 3.25

Figure 5.3. Mn 3s photoelectron spectra at 40 K of (a) bulk Mn and (b) islanded Mn with corresponding output from the fitting routine. In (b) b corresponds to the contribution from the bulk and s from the surface.

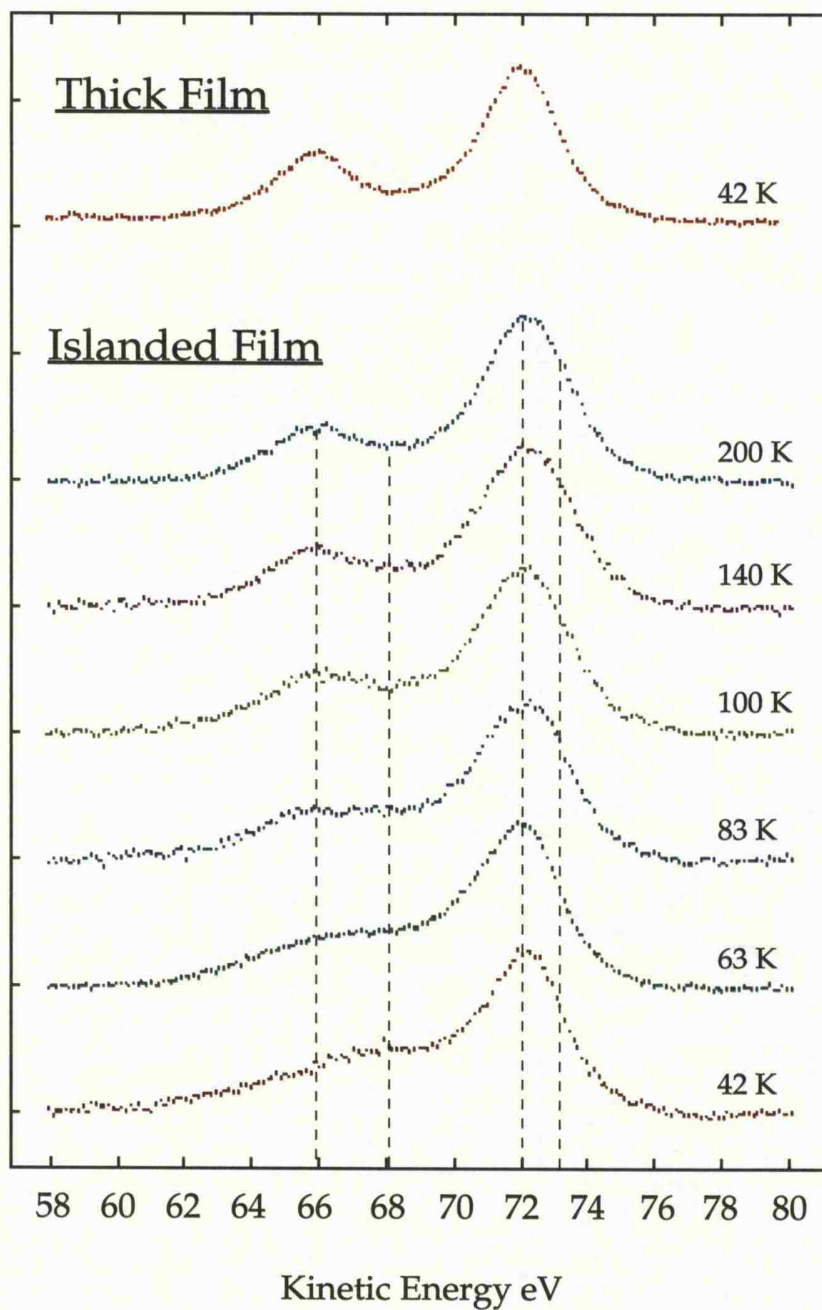


Figure 5.4. Comparison of background subtracted Mn 3s photoelectron spectra at various temperatures from the islanded film with bulk Mn. Also shown are the peak positions used for the islanded film analysis.

one from the thick film. A more complex lineshape structure is evidenced in the islanded film by the stark difference between the spectra, it clearly shows that there are more than two components leading to the conclusion that there is an observable contribution from the surface of the particles as well as from the interior. The procedure for the islanded films was then to fix the peak positions as marked in figure 5.4 during the fitting. It should also be noted that any background subtracted spectra displayed are the respective results from the fitting procedure and that only raw data has been used in quantitative analysis.

5.4 SPPED Results of Mn Films on HOPG

5.4.1 Thick Mn Film

Figure 5.5(a) shows background subtracted photoelectron spectra in the region of the Mn 3s multiplet at 6 different temperatures. These are typical of all the spectra recorded for this film in that there are no dramatic changes observed in the lineshape structure or the peak separation of the multiplet components. Closer observation, on the other hand, does show a change in the relative intensities of the two peaks as the temperature is changed. Figure 5.5(b) shows three of the spectra from figure 5.5(a) overlaid and normalised to the height of the high kinetic energy peaks, clearly displaying a decrease in the relative intensity of the 5S or spin-up peak with an increase in temperature. The spectra were fitted allowing the individual $^5S/^7S$ integrated intensity ratios to be calculated, these ratios were then expressed as a percentage change in terms of the experimental spin asymmetry, S_{exp} , defined by Sinkovic and Fadley(1985). Measurements were made between 40-700 K in the direction of increasing

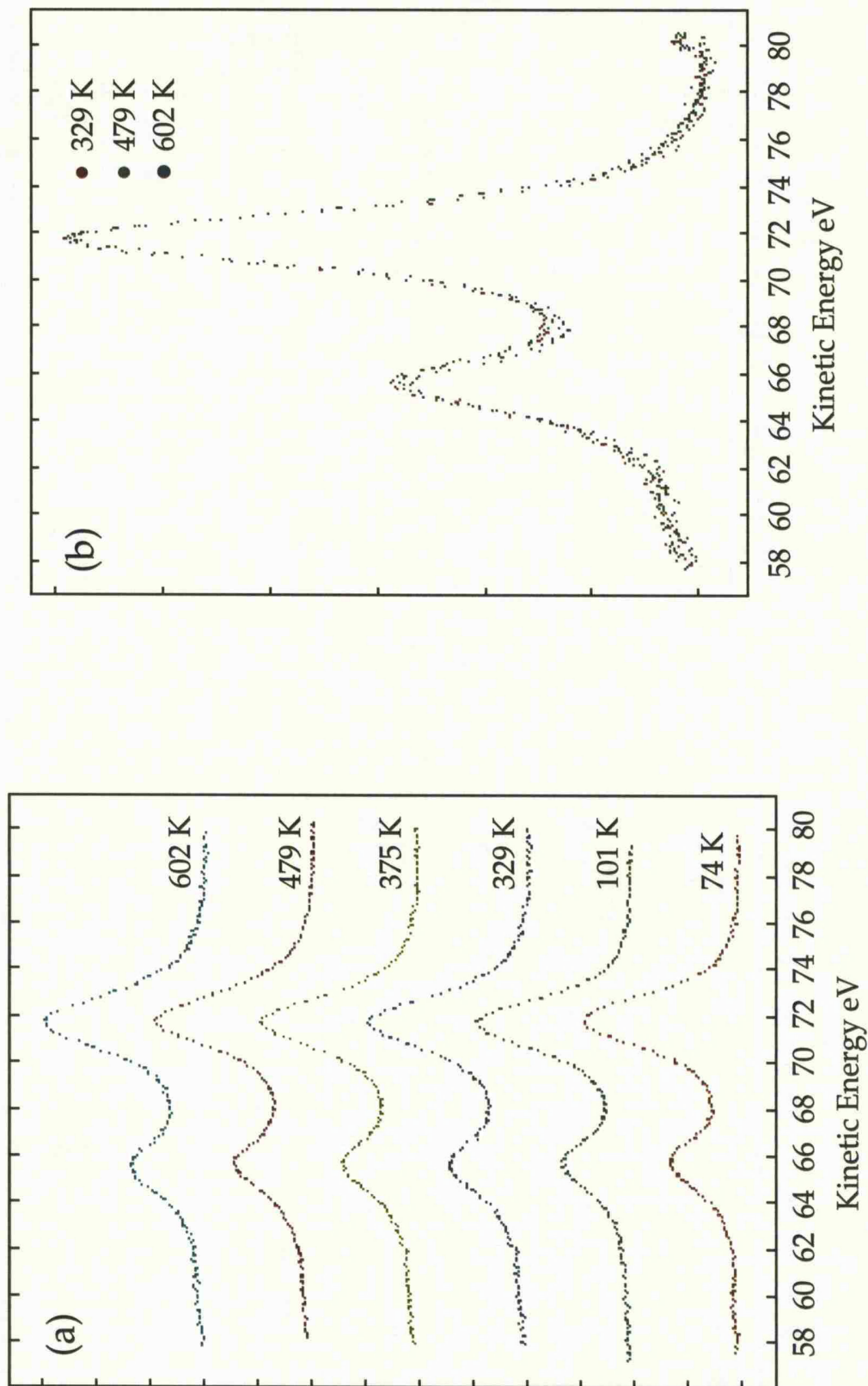


Figure 5.5. (a) Comparison of background subtracted Mn 3s photoelectron spectra from bulk Mn at various temperatures, (b) three of the spectra from (a) overlaid and normalised to the 7S peak height indicating the change in the relative intensity of the 5S and 7S peaks as temperature is varied.

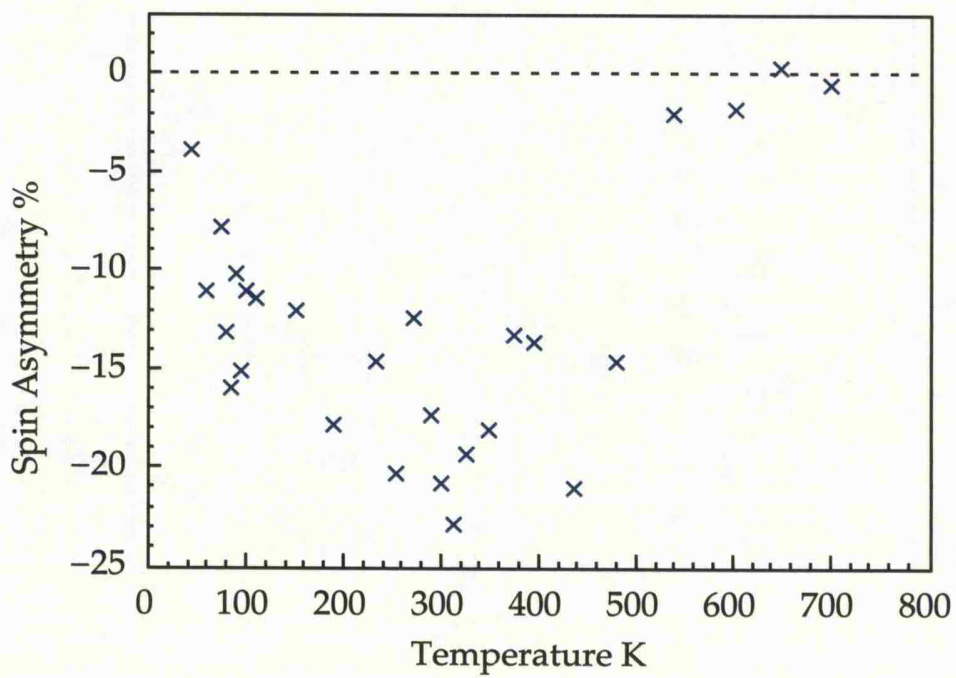


Figure 5.6. Experimental spin asymmetry of the Mn 3s core level as a function of temperature for the bulk film.

temperature. After reaching the upper limit the film was cooled to room temperature to perform a further reading as a stringent test that any change observed was reversible. The results for the thick Mn film are displayed in figure 5.6 where the spin asymmetry is plotted as a function of sample temperature. The plot shows an initial increase in spin asymmetry over the temperature range 80-100 K to an average value of -17% where it levels off until the temperature range 490-520 K where there is an abrupt fall off to zero.

5.4.2 Islanded Mn Film

As previously seen in figure 5.4 the photoelectron lineshape of the Mn 3s multiplet in the islanded film is more complex than that of the thick film. Figure 5.7 shows four of the spectra from figure 5.4 overlaid and normalised to the height of the high kinetic energy peaks. The ^{7}S peak is shown to have an essentially constant shape with temperature variation, as did both components in the thick film case (figure 5.5(b)), but the ^{5}S peak obviously does not. At low temperature there is more intensity in the kinetic energy region from 67-70 eV, corresponding to the trough between the ^{5}S and ^{7}S peaks in the thick film. As the sample temperature is increased this intensity decreases while the intensity in the region from 65-67 eV kinetic energy begins to increase, and the lineshape adopts that of the thick film. Measurements were made between 40-400 K in the direction of increasing temperature. The data were fitted and the results are displayed in figure 5.8 which shows the temperature dependence of the spin asymmetry for the combined contributions from the ^{5}S and ^{7}S peaks. The plot shows an average spin asymmetry of -26% at low temperature which abruptly falls to zero between the temperature range 80-100 K. This is a surprising result

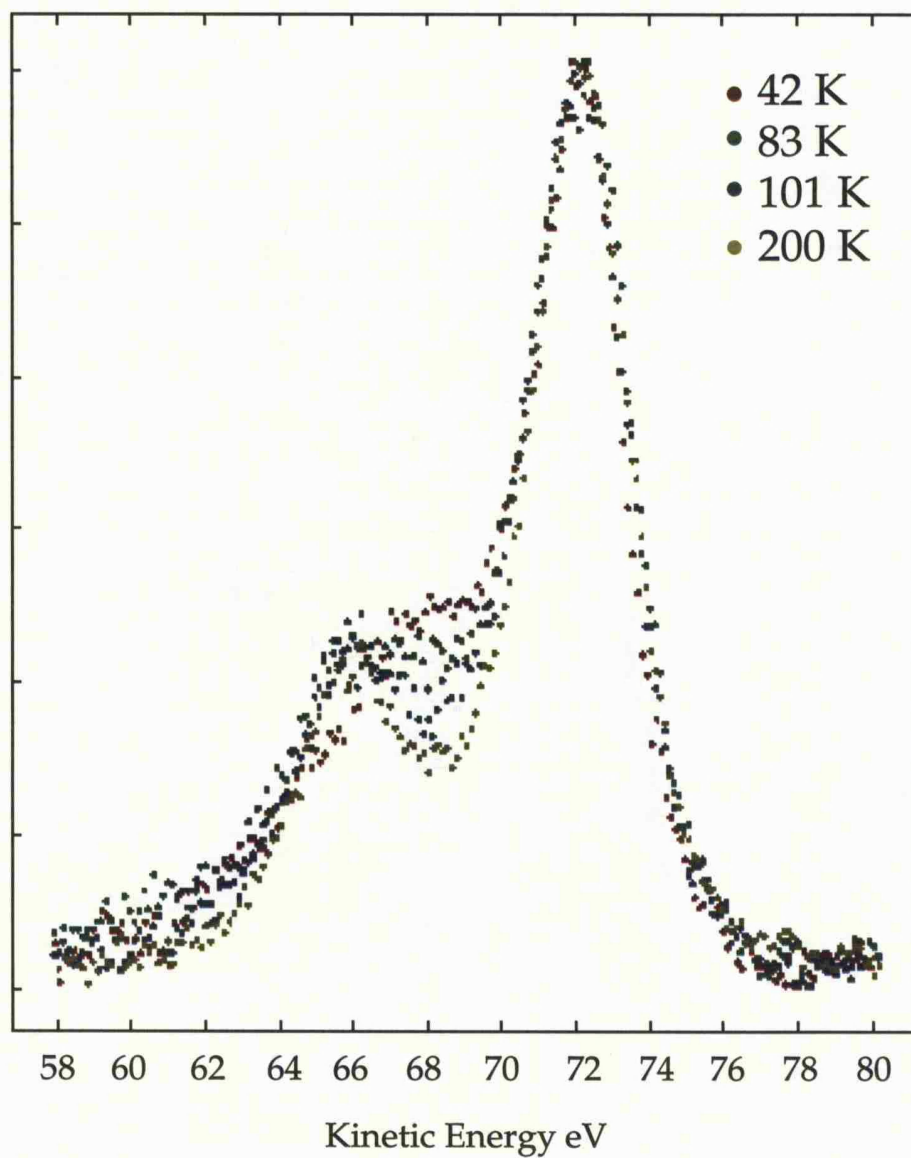


Figure 5.7. Background subtracted Mn 3s photoelectron spectra from the islanded film overlaid and normalised to the height of the 7S peak indicating the change in relative intensity of 5S and 7S peaks as the temperature is varied.

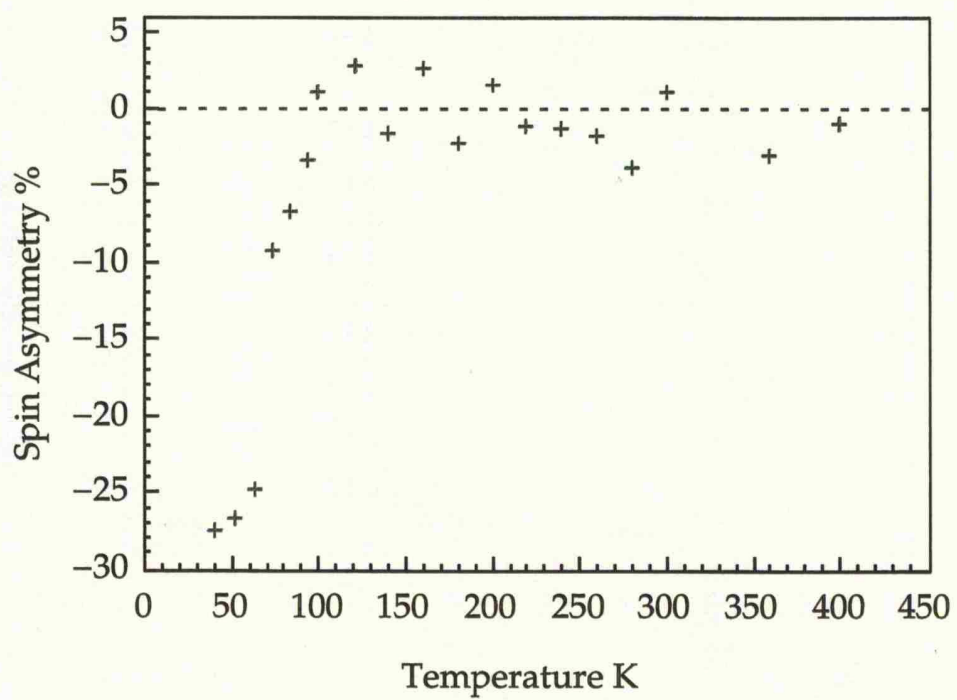


Figure 5.6. Experimental spin asymmetry of the combined contributions from the 5S and 7S peaks from the Mn 3s core level as a function of temperature for the islanded film.

since unlike all the bulk systems the change here is seen at the bulk Mn Néel temperature, there may well be a modified Néel temperature for the cluster though.

5.5 Discussion

It has been postulated that the abrupt step in the spin asymmetry, observed at T_{SR} , several times the Néel temperature, could result from a short-range magnetic order (SRMO) to disorder transition (Sinkovic and Fadley 1985). SPPED primarily samples near neighbour scattering events, i.e. short-range order effects, and since the only possible change in the scattering potential comes from the variation in temperature, this in turn affects the exchange term for spin-polarised photoelectrons through the orientation of the magnetic moments and manifests itself as a modification of the relative intensities of the two peaks.

Figure 5.9 compares the thick film results with other data for MnO, from Hermsmeier *et al* (1989), and $KMnF_3$, from Sinkovic *et al* (1985). There is good agreement between the three data sets in that the average value for the spin asymmetry just below T_{SR} is the same at approximately 17%. The value for T_{SR} is taken at the point of maximum slope in the step and occurs at 505 ± 10 K for bulk Mn, it compares with 530 ± 20 K for MnO and 240 ± 5 K for $KMnF_3$. These transitions occur at approximately 5.3 times T_N for bulk Mn, 4.5 times T_N for MnO and 2.7 times T_N for $KMnF_3$, showing a persistence of local magnetic order above the bulk ordering temperature. This result is not new, neutron scattering measurements by Schull *et al* (1951) along with simple mean-field

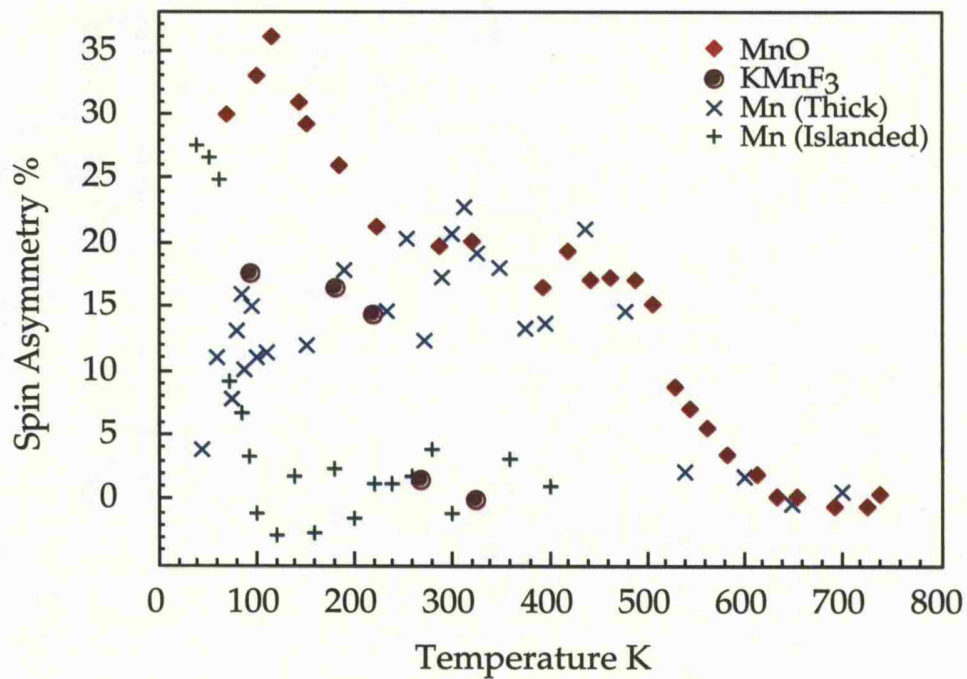


Figure 5.9. Comparison of experimental spin asymmetries from the bulk (x) and islanded (+) Mn films, which is the same data as in figures 5.6 and 5.8 respectively, with data on MnO (●) after Hermsmeier *et al* (1989), and KMnF₃ (◆) after Sinkovic *et al* (1985). It should be noted that ordinate scales for some of the data have been reversed to allow a direct comparison.

theoretical models by Smart (1966) have previously indicated that SRMO persists at high temperatures in MnO. Also, NMR data by Yamagata and Asayama (1972) along with neutron diffraction studies by Yamada *et al* (1972) and d.c. susceptibility measurements by Nagasawa and Uchinami (1973) have all reported atomic magnetic moment values for α -Mn in the paramagnetic phase, with Shull and Wilkinson (1953) reporting a magnetic moment up to 500K using neutron diffraction. However, the important result is that SRMO is seen to disappear very suddenly at T_{SR} , an effect which is not predicted by any current model of the short range spin-spin correlation function.

The curves do not show the simple monotonic form expected for a differential Debye-Waller effect on the two peaks involved. Sinkovic *et al* (1991) have investigated the effects of thermal vibrations on the measured spin asymmetries as the temperature is varied, by incorporating Debye-Waller effects into model calculations. The results showed significant changes for the back-scattering region only, with a calculated spin asymmetry of less than 0.5% for forward scattering.

The SPPED studies on the single crystals MnO and $KMnF_3$ have involved measurements along well defined crystallographic directions leading to measured spin asymmetries in the range ± 4 to 30%. A variation of emission direction has also given rise to different shapes of the curves as well as slopes, as evidenced in figure 5.1 where, for MnO, normal emission gives a sharp *decrease* in spin asymmetry but 15° off normal emission gives a more gradual *increase*. Although the exact nature of these differences is not understood it is thought to be linked to the local atomic environment on the scale of a few

nearest neighbours. The results presented here from the bulk Mn film will, however, reflect some sort of average because the film was polycrystalline. The data compare favourably by looking at the region around the transition, where the changes observed through the short-range order to disorder transition in all three sets are about 10-15%.

A further comparison can be drawn between the bulk Mn and MnO data at the long-range ordering temperatures where definite changes of slope are seen. The possibility of such a short-range order probe being sensitive to the loss of long-range magnetic order as well has been addressed by Hermsmeier *et al* (1990) who performed a similar spin asymmetry experiment on the Mn 3p level. This showed very similar results to the Mn 3s investigation with a maximum spin asymmetry of approximately +45% at low temperature, an abrupt change in the spin asymmetry of about 10% at 540K and a change of slope at the Néel temperature. The fact that the last point is seen in both the 3s and 3p multiplets in spite of the much different energy spacings and intensity ratios involved supports the idea that SPPED is sensitive to long-range order effects.

The results from the islanded film, figure 5.8, perhaps provide some further support to the above statement. The spin asymmetry is seen to fall abruptly to zero as the bulk Mn Néel temperature is passed. An important conclusion can be drawn from this result. In a mesoscopic system the role of dimensionality is paramount in the modification of the particles properties. The dimensions of the system may well be of the same order of magnitude or smaller than the correlation length for long range magnetic order. Implying then that as the

temperature is increased through the bulk Néel temperature this may induce a complete loss of magnetic order down to atomic length scales. These conclusions are supported by temperature-dependent changes seen in the 3p and valence band spectra for the islanded film which are discussed in chapter 6.

5.6 Summary

Spin-polarised photoelectron diffraction has been employed to investigate short-range magnetic order (SRMO) in bulk Mn and an islanded Mn film where the average island size was 6 nm. For bulk Mn the SRMO transition to disorder was observed to occur at approximately 505 ± 10 K.

SRMO has been shown to persist at temperatures well above the temperature at which long range magnetic order is lost in the bulk, to over five times the Néel temperature. The maximum spin asymmetry observed of approximately 17% compares well with similar data from antiferromagnetic Mn containing compounds. The temperature dependence of the spin asymmetry has also shown an effect at the bulk Néel temperature consistent with data from one of the Mn compounds, a surprising result considering the relatively short scale nature of the photoemission process.

The islanded Mn film produced a maximum spin asymmetry of 26% and provided a very surprising result in that the spin asymmetry was observed to fall abruptly to zero as the temperature was increased through the Néel temperature a feature not previously observed with SPPED.

Chapter 6

Photoemission from Bulk Mn and Mesoscopic Mn particles.

6.1 Introduction

6.2 Experimental

6.3 Results and Discussion

6.4 Summary

Chapter 6

Photoemission from Bulk Mn and Mesoscopic Mn particles.

6.1 Introduction

Allied with the results from chapter 5 in which was presented a SPPED study of Mn using photoemission from the 3s core level, this chapter presents 3p and valence band photoemission from the same bulk and particulate Mn films. An important consideration in metallic systems with nanoscale dimensions is the modification of the collective behaviour of the electron gas as the system becomes more confined, that is, with decreasing particle size. Wertheim and Citrin (1978) have shown that by measuring the lineshapes of core level photoelectrons detailed information can be gained regarding the response of the valence electrons to the creation of a core hole in photoionisation. Subsequently core hole screening in adsorbates on metals and in small metallic particles has been discussed quite extensively, see Fuggle *et al* (1978), Norton *et al* (1978), Bagus *et al* (1981), Stöhr *et al* (1983), Eberhardt *et al* (1985), Castellani *et al* (1985), Matthew (1990), Binns *et al* (1992), Methfessel *et al* (1993) and Uozumi *et al* (1996) for a selection of relevant references.

Eberhardt *et al* (1985) investigated the C 1s photoemission lineshape and width for different adsorbate environments. The Doniach-Sunjić asymmetry of the lineshape was observed to change with adsorbate species and this was correlated with the adsorption geometry. The asymmetry index was also calculated by dividing the half width half maximum of the low kinetic energy side of the peak by the one at the high kinetic energy side of the peak and converting the corresponding ratio directly as an independent confirmation of the fitted Doniach-Sunjić parameter.

Measurements of mesoscopic Cr and V particles by Binns *et al* (1992) revealed size-dependent changes in the screening response of valence electrons. The collective electron behaviour in these small particles was perturbed producing a less effective screening response, which was understood as a "stiffening" of the electron gas as it became more confined.

6.2 Experimental

The experimental measurements were made on beamline 6.1 of the SRS. The sample preparation and experimental procedure were as described in chapter 5.2 except that 3p photoelectron spectra were recorded over the kinetic energy range 90-120 eV with a photon energy of 160 eV.

6.3 Results and Discussion

In figure 6.1 (a) and (b) are displayed 3p and valence band photoelectron spectra from bulk and islanded Mn films respectively at various temperatures. In figure 6.1 (a) a comparison between the low and high temperature spectra from both the 3p and valence band shows no significant change with temperature. By contrast in figure 6.1 (b) the 3p lineshape and valence band spectra are seen to change considerably as the temperature is increased from 40 K through the Néel temperature. This marked change in lineshape is consistent with the SPPED result from the islanded sample in chapter 5 where the 3s core level photoemission lineshape was seen to change dramatically going through the Néel temperature. A theoretical study of monoxides, including MnO, by Ojala and Terakura (1986) predicted a change in the valence density of states between the antiferromagnetic and paramagnetic states, and

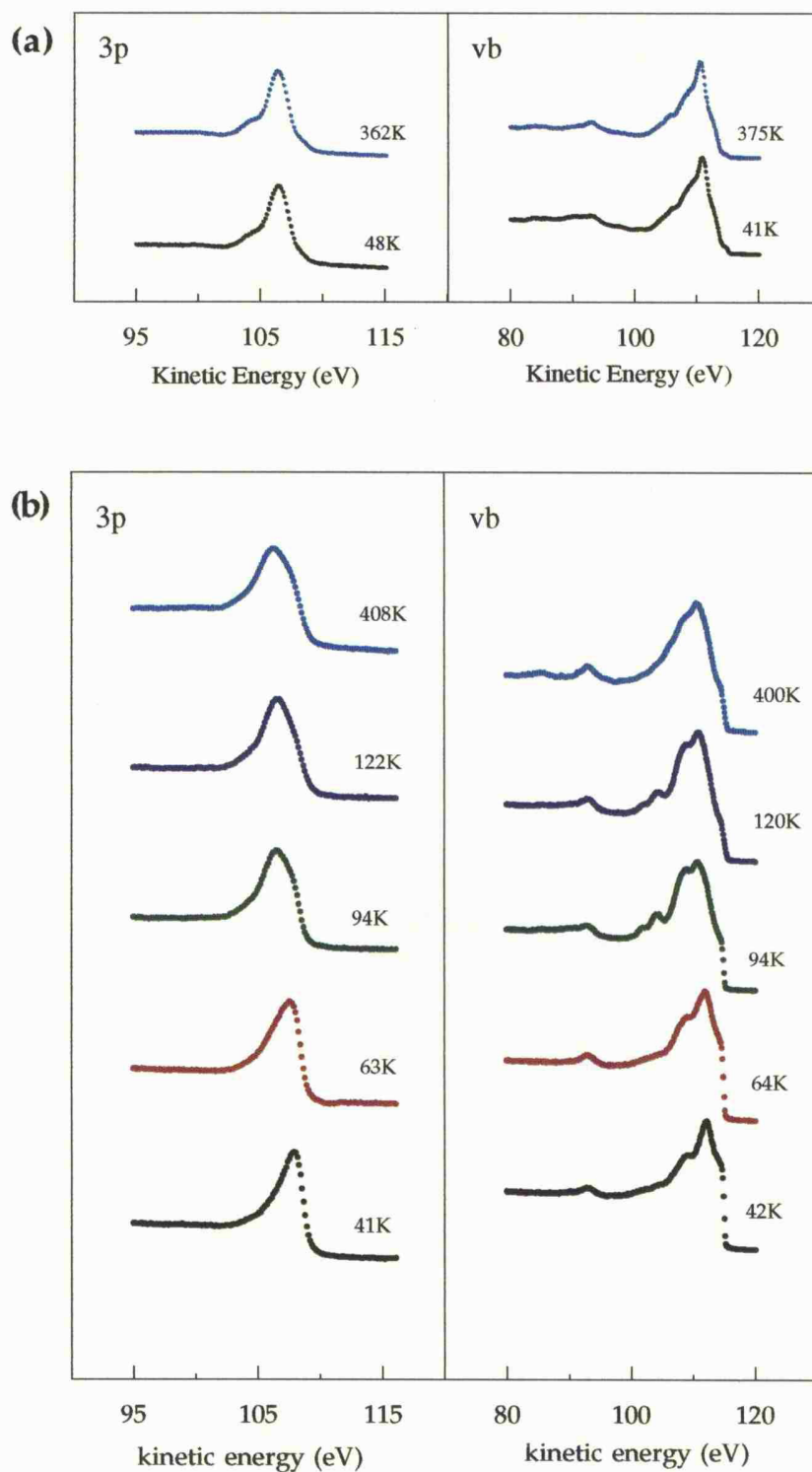


Figure 6.1. Comparison of 3p and valence band photoelectron spectra from (a) bulk manganese and (b) islanded manganese (where the average island size was 6nm) at various temperatures.

Hermesmeier *et al* (1990) observed a sensitivity of experimental valence band spectra from MnO to magnetic order. Taking these results into consideration it would not be unreasonable to explain the observed changes in the 3s and 3p core level and valence band photoemission spectra at the Néel temperature as an effect due to the complete loss of magnetic order in the whole particle.

Comparing the 3p spectra there is a contrast in the general lineshape between the bulk and islanded samples, indicating a modification of the multiplet structure in the islanded sample. Binns *et al* (1992) previously reported a significant change in 3p lineshape in islanded Cr and V films. Within a configuration interaction approach it is possible to distribute a peak intensity over a large number of states. The behaviour of the 3p multiplet structure could therefore be explained by an increase in the overlap of hole states with alternative configurations, as a result of size dependent changes in the distortion of excited orbitals.

Figure 6.2 shows the asymmetry of islanded Mn films as a function of particle size, similar Cr data is reproduced from Binns *et al* (1992) for comparison. An increase, relative to bulk Mn, in the peak asymmetry of the 3p photoemission spectra for the Mn particles is observed. The asymmetry has been calculated from the ratio of the half width half maximum measured on the low and high binding energy sides of the peak. Binns *et al* (1992) observed an increase in peak asymmetry with decreasing particle size for mesoscopic Cr and V particles. An increase in asymmetry indicates either an increase in the density of states near the Fermi level or a deeper potential produced by the core hole, as a result of less efficient screening by the valence electrons. Previously it was argued that the latter effect was responsible for the

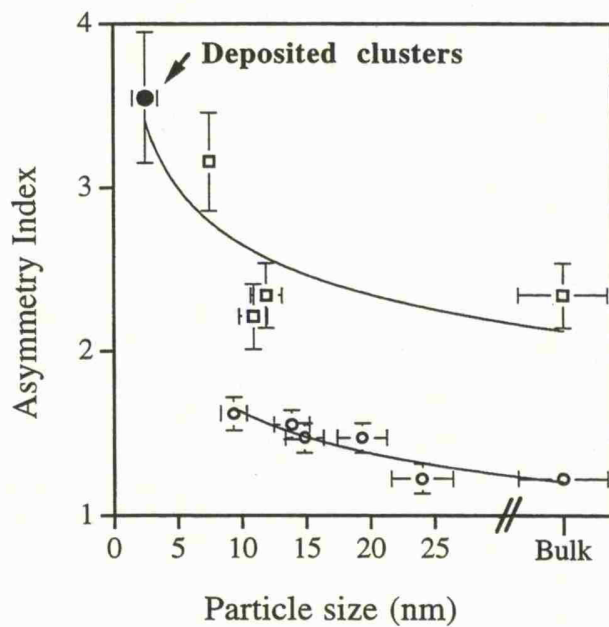


Figure 6.2 Asymmetry index (ratio of HWHM on low and high binding energy side) of Mn (\square) and Cr (\circ) 3p photoemission lines as a function of particle size, where (\bullet) is deposited Mn clusters on graphite (see chapter 7).

observed increase in asymmetry. In this case the observed increase in local moment of nanoscale Mn particles (see chapter 7) is consistent with an increased density of states at the Fermi level, so it is difficult to say which effect is dominant.

6.4 Summary

Photoemission from islanded Mn has shown a modified 3p core level lineshape relative to the bulk indicating a possible increase in the overlap of hole states. A size dependence of the peak asymmetry of the 3p core level in islanded Mn has indicated either an increase in the density of states near the Fermi level or a deeper core hole scattering potential. 3p core level and valence band photoemission spectra have shown dramatic changes as temperature is increased through the Néel temperature. These results in conjunction with the SPPED result for the islanded sample lead to the conclusion that as the long range magnetic ordering temperature is passed a complete loss of magnetic order is induced over the whole particle.

Chapter 7

Photoemission from Deposited Mesoscopic Mn Clusters.

7.1 Introduction

7.2 Experimental

7.3 TEM and Size Distributions

7.4 Results

7.5 Discussion

7.6 Summary

Chapter 7

Photoemission from Deposited Mesoscopic Mn Clusters.

7.1 Introduction

The final part of this thesis is concerned with a synchrotron radiation photoemission study of deposited ready-made Mn clusters. This work presents the next stage of the research programme into mesoscopic systems by the Leicester group with the use of a recently developed gas aggregation source to produce the clusters and deposit them *in-situ*. The first experimental data using the Leicester University Mesoscopic Particle Source (LUMPS) is presented here. Photoelectron spectra were recorded from uncovered mass filtered clusters and from a nanoscale granular film consisting of a continuous V matrix incorporating unfiltered Mn clusters. Size-selection was achieved with the aid of a quadrupole filter.

Adsorbing particles on a solid surface or embedding them within a matrix will modify their intrinsic properties and introduce particle-host and particle-particle interactions. Davies (1994) has shown an enhancement of the remanent magnetisation of nanoscale ferromagnetic assemblies as being due to the exchange interaction between the grains. Xhie *et al* (1991, 1992) have induced charge-density waves (CDW's) on graphite surfaces and observed a tendency for Pt and Co particles to assemble at the nodes of the CDW. Such cluster lattice systems observed also for C₆₀ by Li *et al* (1991) and Au particles by Sattler (1992) are examples of the new forms of matter that can be created. Lineshape studies of the x-ray photoemission of small metal Pd and Pt clusters by Cheung (1983) have

shown an increase in linewidth and a shift of the line position toward higher binding energy with a decrease in particle size.

V is paramagnetic in the bulk although it is close to being magnetic and is easily polarised. Theoretical studies by Gempel and Ying (1980), Yokoyama *et al* (1981), Fu *et al* (1985), Gay and Richter (1986) and Blugel *et al* (1988) have predicted magnetic order localised at the surface or in ultra-thin films. However, experimental studies by Rau *et al* (1986), Drube and Himpsel (1987), Stampanoni *et al* (1988), Rau *et al* (1988), Moodera and Meservey (1989) and Fink *et al* (1990) show conflicting results. Binns *et al* (1992), however, have reported photoemission from islanded V films identifying a low spin component to a multiplet split $3s$ contribution with the interpretation that the surface of the film was magnetically ordered. It has also been interpreted as due to a dielectric relaxation effect by Rakotomahevitra *et al* (1995) but the magnetic interpretation was favoured since the feature is observed much more weakly on continuous films than on islanded films where a higher proportion of the photoemission signal is from the surface. It has also been shown by Binns *et al* (1992) that a small trace of CO contamination completely removed the feature and possibly explains conflicting results between theory and experiment.

7.2 Experimental

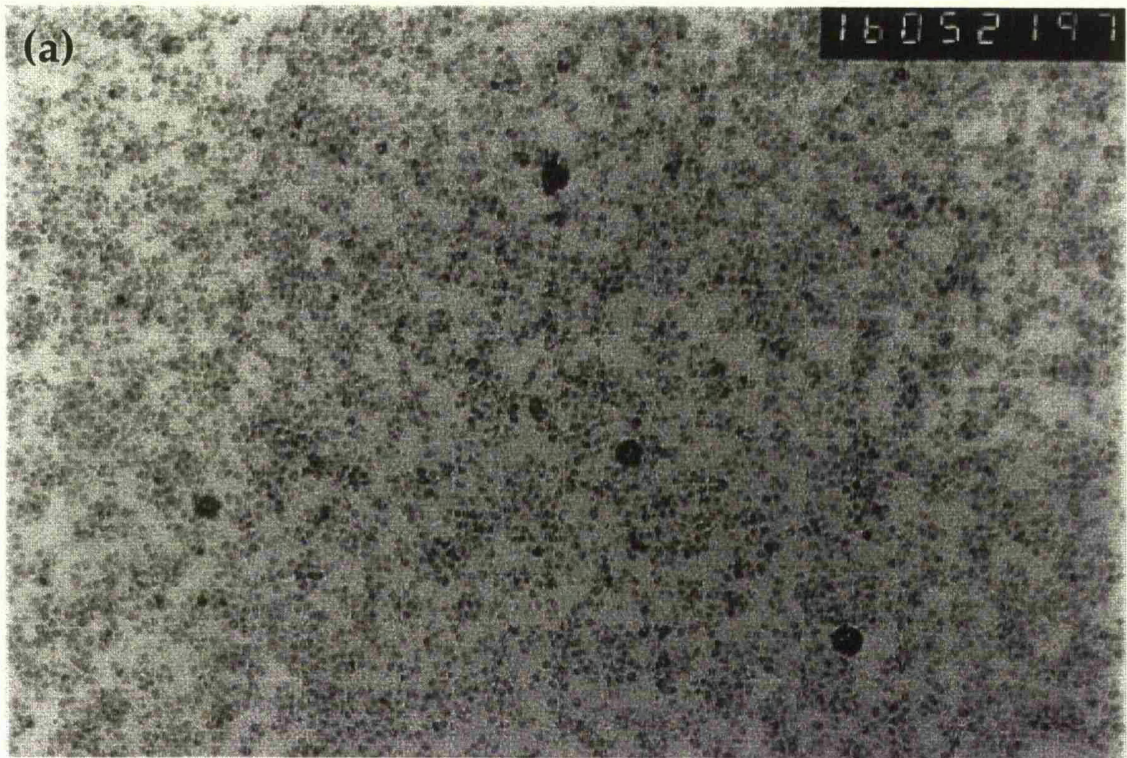
The measurements were made on beamline 6.1 of the SRS at Daresbury Laboratory. The gas aggregation source was coupled to the UHV sample chamber and the clusters were deposited directly onto HOPG substrates. The reader is directed to chapter 3.2.6 for a detailed description of the cluster source and

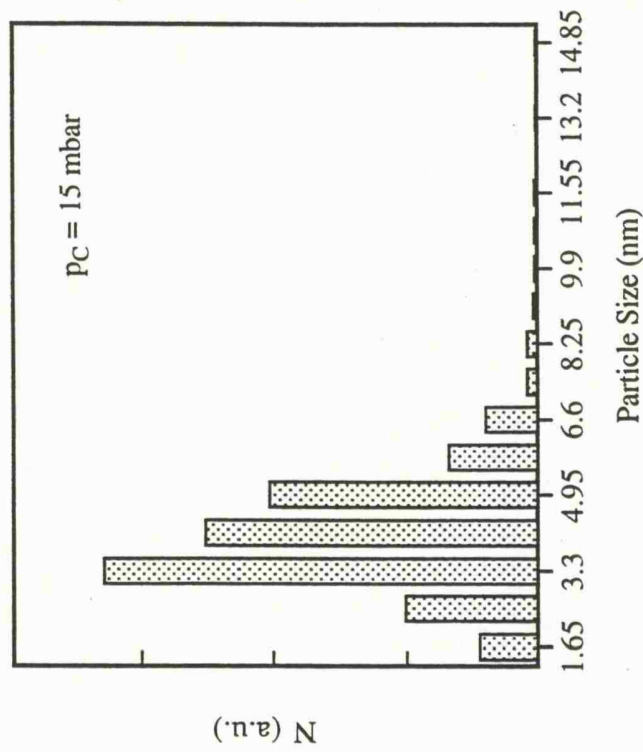
operating conditions. During deposition the chamber pressure rose to 5×10^{-6} mbar of the helium bath gas with a contaminant partial pressure, mainly CO, of 5×10^{-11} mbar. On closing off the source, the main chamber recovered to its base vacuum of 2×10^{-11} mbar within 5 minutes. The substrates were cleaved in air and, prior to deposition, they were heated to 1000 K for 30 minutes in UHV, leaving no trace of the main contaminants O, N and S but occasionally produced a small level of Si contaminant as evidenced by the appearance of a weak Si 2p feature. During deposition the substrates were cooled to 40 K to inhibit surface diffusion of the clusters. During the mass filtered deposition the quadrupole was set to filter particles of 3.8×10^4 amu (2.5nm) with a 10% resolution. For the deposition of the granular film the mass filter was turned off and V was co-deposited from a compact electron beam MBE source surrounded by a water cooled jacket, Taylor and Newstead (1987). The photoelectron spectra were recorded with a VSW HA100 electron energy analyser using 16 channel detection. The combined resolution of the monochromator and the analyser was 0.4 eV at a photon energy of 160 eV.

7.3 TEM and Size Distributions

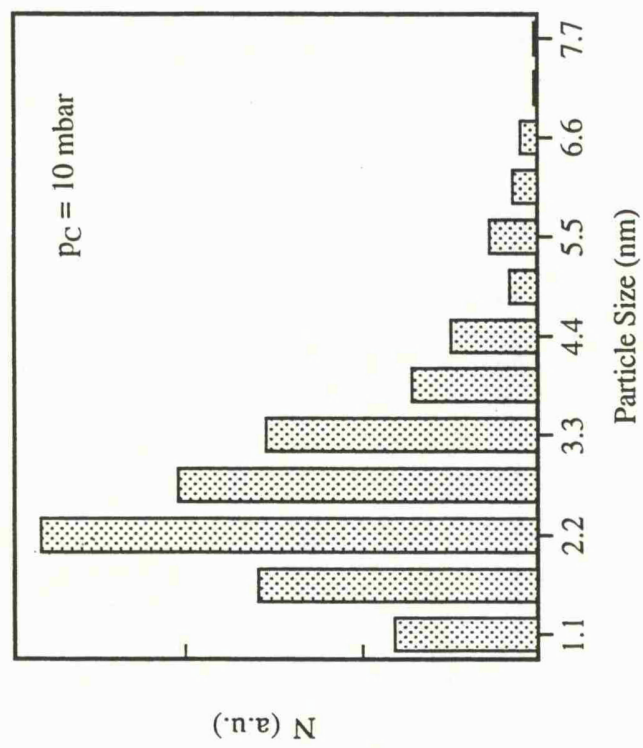
The quadrupole filter has been calibrated by imaging the deposited clusters in a transmission electron microscope. The clusters were deposited on carbon coated copper TEM grids under the same operating conditions used in the experiment. Plate 7.1 shows transmission electron micrographs of two 5 minute depositions of unfiltered clusters, (a) is with the gas cell at 10 mbar and (b) at 15 mbar, revealing well defined particles. Investigation of the distribution of particle sizes, shown in figure 7.1, reveals the expected log normal distributions peaking at (a) 2.2 nm for

Plate 7.1 Transmission electron micrographs of Mn clusters on Cu grids (a) gas cell pressure 10 mbar, (b) gas cell pressure 15 mbar.





(a)



(b)

Figure 7.1 Cluster size distributions measured from the TEM photographs: both are from 5 minute unfiltered depositions where (a) is with the gas cell pressure at 10 mbar and (b) at 15 mbar.

the 10 mbar run and (b) 3.3 nm for the 15 mbar run. Granqvist and Buhrman (1976) have presented a detailed study of the use of log-normal distribution functions in the analysis and theoretical prediction of island size distributions in the growth of ultra-thin metallic films. Suffice it to say here, though, that generally experimental studies arrive at this result. Figure 7.2 shows a comparison of the size distribution of the deposited clusters from the 10 mbar run between measurements from the TEM photograph (bars) and the ion current measured at the end of the filter (dots). The agreement between the two sets of data is very good showing that particle integrity is maintained on landing. This is further qualified by a recent STM study by Upward *et al* (1996). Figure 7.3 shows STM images of unfiltered Mn clusters from the gas aggregation source deposited on the Si (111) surface, note the atomic resolution achieved for the Si substrate in figure 7.3 (b) which shows a close up of figure 7.3(a). Analysis of the STM results shows the same range of cluster sizes as was found in the TEM study and that the clusters do not fragment on landing, though the clusters are longer than higher, the height is approximately 1/3 -1/2 times the length. From figure 7.3 (a) it is also evident that the clusters do not appear to have a preference to align along step edges, one of which is visible in the bottom left of the picture.

7.4 Results

Figure 7.4 shows the photoemission spectrum over the region of the Mn 3s core level obtained from 4 types of Mn films, (a) and (b) are from exposed clusters with increasing coverage and (c) is from an islanded sample where the average island size was 6 nm and (d) is from a thick film. Samples (c) and (d) were produced by a

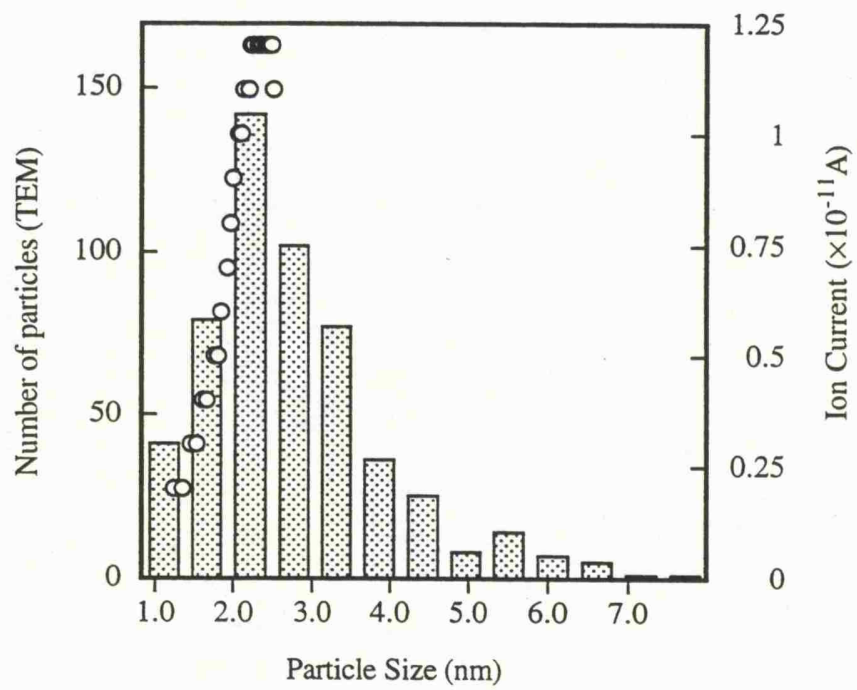
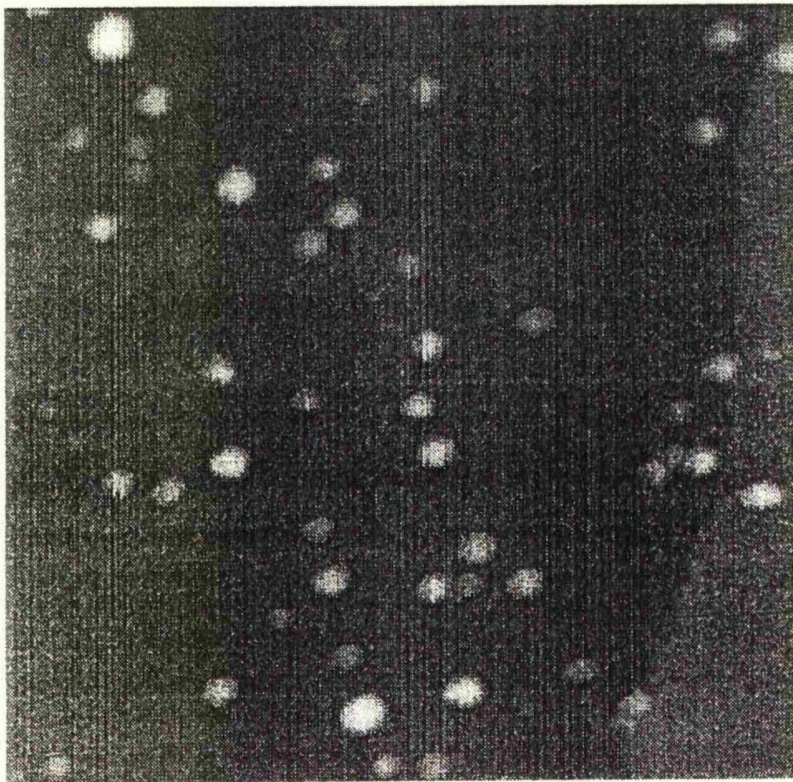
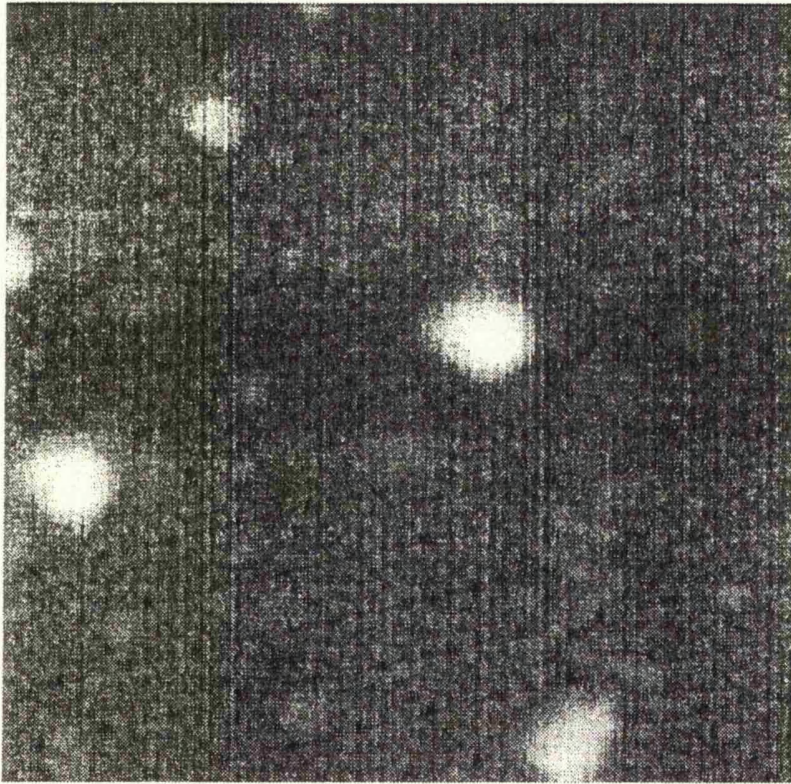


Figure 7.2 Comparison of size distribution measured from the TEM photo (bars) and ion current (O) measured at the end of the filter.



(a)



(b)

Figure 7.3 (a), (b) STM images of Mn clusters deposited on Si (111), (b) is a close up of (a).

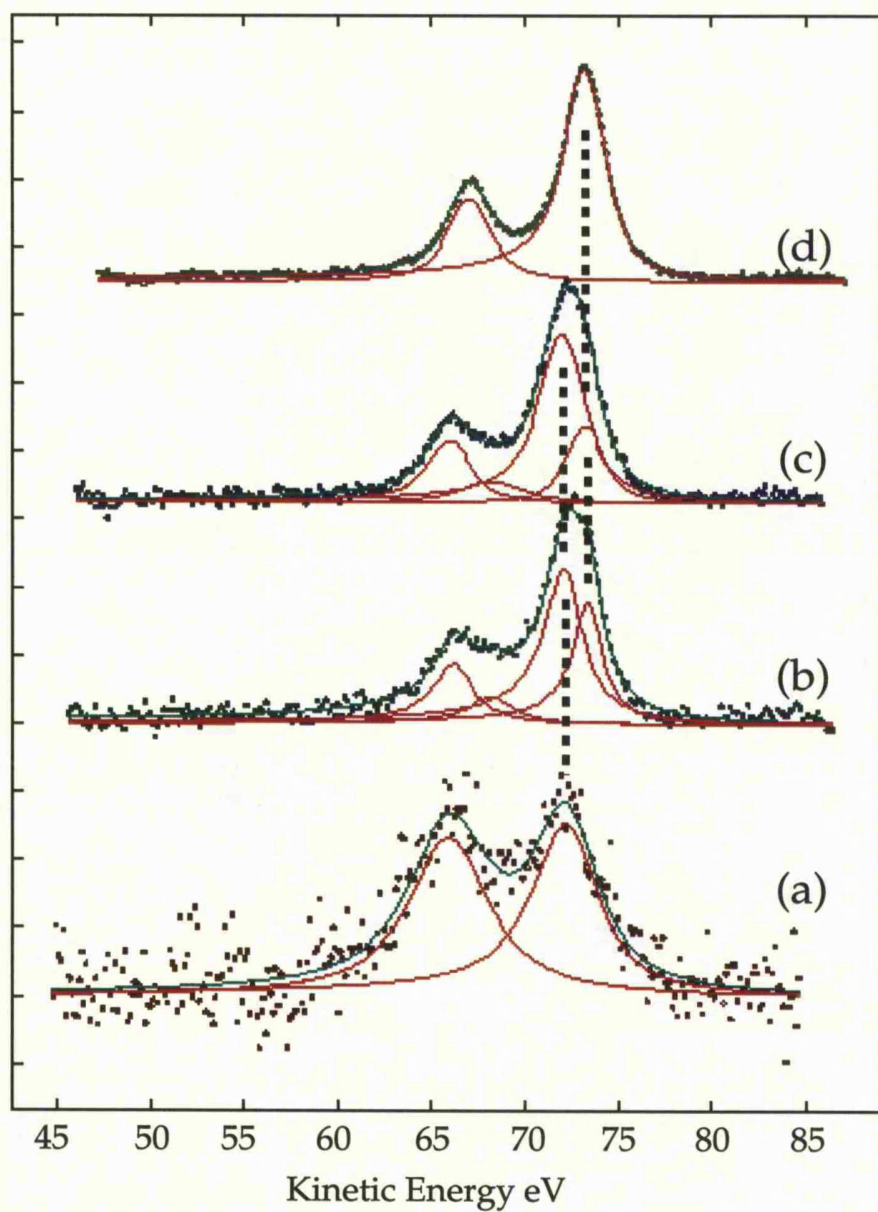


Figure 7.4. Comparison of Mn 3s core level photoelectron spectra from (a) 2.2 nm size selected clusters, (b) unfiltered clusters with an average size of 4 nm, (c) an islanded sample produced by a conventional evaporation source with an average size of 6 nm and (d) a thick continuous film.

conventional MBE type evaporation source with conditions such that Volmer-Weber growth would occur. The spectra have been fitted by Doniach-Sunjić lineshapes on a background modelled by a Tougaard contribution, Tougaard (1986), plus a polynomial. All spectra are displayed with the inelastic background subtracted and in (a), which is a very low coverage sample, two additional peaks have also been subtracted; a Si 2p line from the dilute Si contaminant at 54 eV and a weak feature in the graphite background at 63 eV leaving the remaining Mn 3s peaks indicated by the solid lines.

Figure 7.4 (a) is from a very dilute sample of mass filtered 2.2 nm diameter clusters with a coverage (defined by the intensity ratio of the observed 3s photoemission signal to the bulk value) of 1.8%. The relative peak intensity is considerably different to the bulk value and is probably distorted by an incomplete removal of the graphite feature due to the low count rate. In comparison to the bulk spectrum of figure 7.4 (d) though, there is a shift toward higher binding energy for both components of 1.3 eV and an increased linewidth with an average Lorentzian contribution of 4.4 eV compared to the bulk value of 1.85 eV.

Figure 7.4 (b) is from an unfiltered deposition of clusters with an average size of 4 nm and a coverage of 20%. In this spectrum a definite shoulder has appeared on the high kinetic energy side of the ^{75}S peak and the valley between the two features has filled indicating the appearance of a second 3s doublet. This is ascribed to a sufficiently high cluster density in some regions to produce agglomeration and a bulk 3s contribution to the spectrum. Comparison between spectra (b) and (c), which is from an islanded deposition, shows a very similar lineshape lending

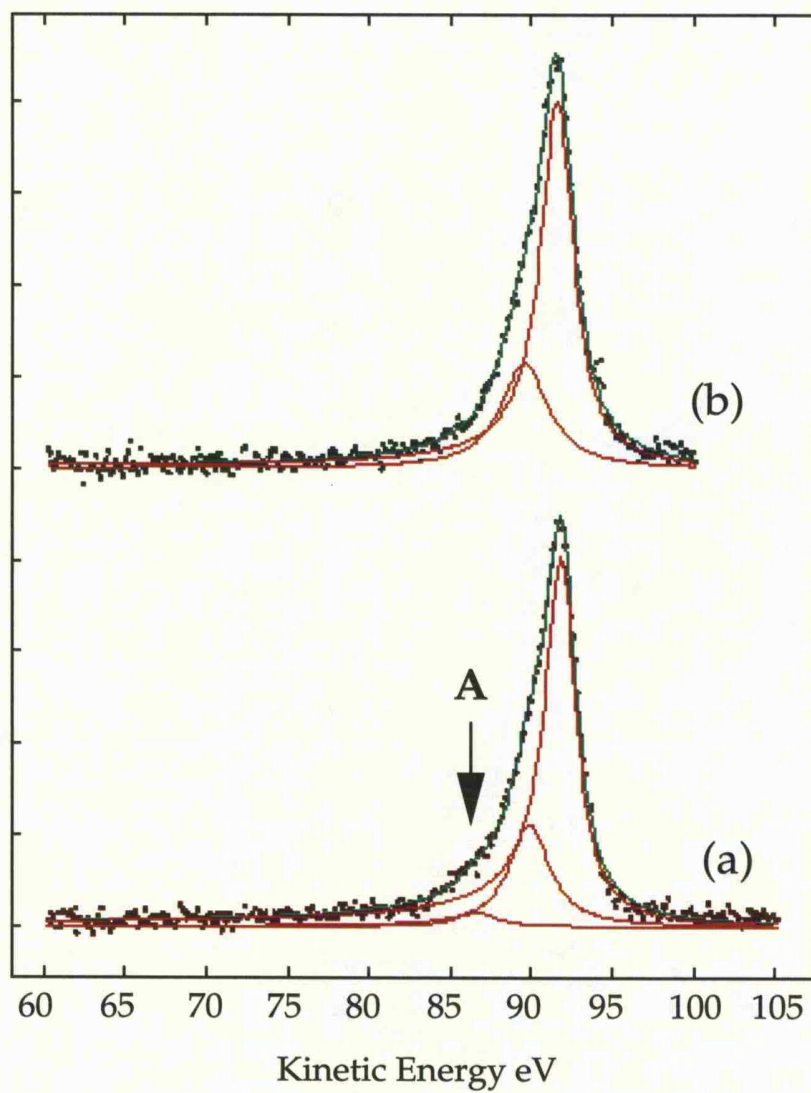


Figure 7.5. V 3s core level photoemission from (a) a granular film consisting of a V matrix embedded with 0.5% Mn clusters and (b) a thick continuous V film.

weight to the above statement. Further support is found in the fit producing the bulk binding energy for the leading set of peaks with the trailing set aligning with the features observed in the more dilute cluster spectra. Spectrum (b) has thus been fitted by four peaks corresponding to contributions from both the cluster, effectively a modified surface contribution, and the bulk. The observed values of the $^{75}\text{S}:$ ^{55}S intensity ratio for the cluster and bulk contributions are 2.81 and 3.25 respectively, and the multiplet splittings are 5.90 eV and 5.16 eV respectively.

Figure 7.5 shows the photoemission spectrum over the region of the V 3s core level obtained from (a) a V film containing embedded Mn clusters from the gas aggregation source at a volume concentration of 0.5% and (b) from a pure V film. An extra feature marked A is observed in the granular film which is not seen in the bulk spectrum.

7.5 Discussion

The Mn 3s spectra from figure 7.4 essentially show a simple doublet for which the energy difference between the spin-up and spin-down components can be interpreted as being due to the 3s-3d exchange interaction. The magnetic origin of the multiplet splitting for Mn has been clearly established by Hermsmeier *et al* (1988). The energy separation (ΔE) and intensity ratio I_R of the multiplets for a 3d spin, S , and a 3s-3d exchange coupling term J^{dc} are given by

$$\Delta E = J^{dc}(2S + 1), \quad (7.1)$$

$$I_R = \frac{(S+1)}{S}. \quad (7.2)$$

The fit to the data in figure 7.4 (b) allows a direct comparison, within the *same* sample, of the cluster and bulk 3s spectrum. The changes observed in the intensity ratio and multiplet splitting are consistent with an increase in the Mn magnetic moment in the clusters relative to the bulk value by about 20%. In conjunction with the results from spectrum (a) one can conclude qualitatively that the magnitude of the increase in magnetic moment is thus inversely related to particle size.

This result is in agreement with reported measurements by Billas *et al* (1994) on particles of the ferromagnetic metals, Ni, Co and Fe for which the convergence to the bulk moment is complete for clusters of about 300, 400 and 500 atoms respectively. For Mn the size distribution peaks for particles containing about 700 atoms. The rate of convergence to the bulk moment with particle size is related to the valence band electron density. Higher densities tend to produce a more rapid convergence to bulk behaviour by a more effective screening of novel surface behaviour, Billas *et al* (1994). The electron density in Ni, Co and Fe descends in the ratio 1.0 : 0.98 : 0.93 which results in a persistence of surface magnetic moments to larger cluster sizes across this series. On the same scale the valence electron density of Mn is 0.89 so enhanced surface moments will persist to larger cluster sizes. Turning to the spin alignment, which is nominally anti-ferromagnetic in the Mn clusters, there is probably a high proportion of uncompensated spins. This will result in ferrimagnetic rather than purely anti-ferromagnetic particles. The

photoemission spectrum however is related only to the magnitude of the atomic moment and is insensitive to spin configuration.

With reference to the investigation by Binns *et al* (1992) the feature marked A in figure 7.5 (a) is interpreted as a low spin component of a multiplet split 3s contribution with the high spin surface component hidden beneath the bulk line. Although it is present only rather weakly in the photoelectron spectrum from the granular film it is suggested that V atoms immediately surrounding the Mn clusters are magnetically polarised by presence of the clusters.

7.6 Summary

Mesoscopic Mn clusters have been deposited from a gas aggregation source onto HOPG. Transmission electron micrographs and scanning tunnelling microscopy has revealed well defined particles which maintain their integrity on landing. Photoemission from exposed mass filtered Mn clusters has revealed an increase in linewidth of the 3s core level with decreasing particle size, along with an increase in binding energy of the line position. Also observed is a decrease in the $^{75}\text{S}:\text{S}$ intensity ratio with decreasing particle size. Results which are consistent with an increase in the Mn magnetic moment with decreasing particle size.

Photoemission from a nanoscale granular film consisting of a V matrix with mesoscopic Mn particles embedded inside revealed a satellite structure in the 3s core level photoemission of V. This was interpreted as a low spin component to

the multiplet split 3s and indicated a magnetic polarisation of V atoms in the vicinity of Mn clusters.

Chapter 8

Summary and Suggestions for Further Work

- 8.1 Introduction
- 8.2 Mn Growth
- 8.3 Photoemission and SPPED Results from Mn
- 8.4 Investigation of Deposited Clusters
- 8.5 Suggestions for Further Work

Chapter 8

Summary and Suggestions for Further Work

8.1 Introduction

This chapter presents a summary of experimental work from the previous chapters discussed with respect to similar studies. More detailed information is presented in the data chapters, chapters 4-7, to which the reader is directed.

The growth and morphology of Mn films on HOPG studied using XUV reflectivity is described in section 8.2. Photoemission and SPPED results from islanded and thick Mn films on graphite are summarised in section 8.3. While photoemission from exposed mesoscopic Mn clusters and clusters embedded in a continuous V matrix is presented in section 8.4. Finally suggestions for further experimental work are described in section 8.5

8.2 Mn Growth

Mn films have been grown by vacuum evaporation with the sample environment conditions such that Volmer-Weber growth would occur to investigate the growth and morphology from the earliest stages through to a thick film. A technique was used which models the surface reflectivity in the XUV spectral region as a function of three parameters: the average island size; the coverage; and a shape parameter. It

involves comparing the measured reflectivity of the islanded film in the range 6-36 nm with a calculation of the clean substrate reflectivity modified by the overlayer.

The calculation uses a theory developed by Jarrett and Ward (1976) in which the reflectivity of an islanded film is calculated by considering the overlayer as a continuous film with an effective refractive index corresponding to an inhomogeneous medium. The results show that initially the Mn covers a large proportion of the surface. This is quickly followed by a vertical columnar growth until the island height is equivalent to the width, at approximately 10 nm. There then follows a change in growth mode to lateral growth, accompanied by a change in sticking probability, until the islands have agglomerated into a continuous film.

8.3 Photoemission and SPPED Results from Mn

The results from chapters 5 and 6 are summarised in this section. SPPED is an emerging technique for the study of magnetic order in magnetic materials. No polarised radiation or external spin detection are required and only a variation of sample temperature is needed to vary the scattering potential. The technique is also sensitive to changes in antiferromagnetic as well as ferromagnetic materials. The experiment requires the measurement of two core photoelectron peaks that are well resolved, close together in kinetic energy and highly spin polarised in opposite directions. Multiplet split core level photoemission lines from partially filled 3d and 4f atoms present suitable cases for study. The diffraction process manifests itself as a modification of the relative intensities of the multiplet split peaks, or as an abrupt

change in the spin asymmetry. This point is attributed to the short range magnetic order (SRMO) to disorder transition.

Mn 3s photoelectron spectra were recorded as a function of temperature over the range 40 to 700 K for the thick film and 40 to 400 K for the islanded film. The relative peak intensities were calculated with a Doniach-Sunjic lineshape fitting routine allowing the temperature dependent spin asymmetry to be found. For bulk Mn the SRMO transition was found to occur at 505 ± 10 K with a measured spin asymmetry of 17% showing a persistence of local magnetic order to over 5 times the Néel temperature. These values compare well with work by Hermsmeier et al (1988) and Sinkovic et al (1985) on antiferromagnetic Mn-containing compounds. For the islanded film this magnetic order-disorder transition occurred at a lower temperature than the thick film, as expected, and produced a surprising result in that it occurred at the Néel temperature, leading to the conclusion that the finite nature of the particles induces a loss of short-range magnetic order when the long-range ordering temperature is passed.

The 3p and valence band photoemission from bulk and islanded Mn provided some interesting results also. The 3p lineshape and valence band photoemission have shown dramatic changes as temperature is increased through the Néel temperature for the islanded sample, whereas no changes in the corresponding spectra for the bulk film were observed between low and high temperature. This agrees with the 3s data and is also a result of the loss of short-range magnetic order at the bulk ordering temperature in a mesoscopic system. The general lineshape of the 3p core level is

observed to have changed with respect to the bulk indicating a modified multiplet structure in the islanded sample.

The asymmetry of core level photoemission lines, which is a result of the collective electron response to the production of a core hole, is seen to increase with decreasing particle size. This increasing asymmetry indicates either an increase in the density of states near the Fermi level or a deeper potential produced by the core hole. It is difficult to say which is the dominant effect though.

8.4 Investigation of Deposited Clusters

An investigation of deposited mesoscopic Mn clusters is presented in chapter 7. The clusters were deposited from a high temperature gas aggregation source directly onto substrates in UHV. Both dilute assemblies of size selected 2.2 nm clusters and unfiltered Mn clusters embedded in a continuous V matrix, to make a nanoscale granular film, have been studied. Mass selection was obtained with the use of a quadrupole filter.

The exposed single size Mn clusters have revealed a modified 3s photoemission lineshape. Qualitatively, an increase in the photoemission linewidth is observed with decreasing particle size along with a change in the line position to increased binding energy and a decrease in the $^{7S:5S}$ peak intensity ratio with decreasing particle size, results which are all consistent with an increasing Mn magnetic moment with decreasing particle size.

Photoelectron spectroscopy of the granular film has revealed a satellite structure in the 3s photoemission of V. It was attributed to a low spin component of a multiplet split surface contribution with the interpretation that the Mn clusters magnetically polarise the immediately surrounding V atoms.

8.5 Suggestions for Further Work

Spin polarised photoelectron diffraction allied with some basic interpretation of photoemission lineshapes has been able to provide very interesting information on the size dependence of electronic and magnetic properties of mesoscopic Mn clusters. Mesoscopic systems in general present a field where electronic and magnetic properties are considerably modified from the bulk but in the form of clusters embedded in 3D metallic matrices is presented the possibility of creating new magnetic materials with application in a wide range of technologies. These systems represent a massive growth area of research in recent years.

Extending the experimental studies to include synchrotron radiation measurements of spin polarised photoelectron spectroscopy, magnetic linear dichroism (MLD) and magnetic circular dichroism (MCD) and magnetometry measurements using a SQUID will allow a much more complete characterisation of the size dependence on electronic and magnetic properties.

MCD and MLD, using circular and linear polarised incident radiation will allow the determination of important magnetic parameters. MCD determines the difference in photoemission signal from core levels as the photon spin is oriented parallel or anti-parallel to the magnetisation. The magnitude of the asymmetry allows the determination of both the total atomic magnetic moment and the orbital contribution. This is important in mesoscopic systems where the orbital moment is enhanced and becomes significant relative to the spin moment. To date studies have only been on magnetic ultra-thin continuous films.

From MLD the temperature dependence of the metal magnetic moment can be determined by monitoring the magnitude of the dichroism signal. Again the bulk of the reported work has concentrated on magnetic ultra-thin films but recent measurements have been performed on mesoscopic Fe particles on HOPG by Baker *et al* (1996). These measurements allied with magnetometry measurements from a SQUID magnetometer would allow the MLD technique to be calibrated with regards to the determination of saturation magnetisation, coercivity and remanent magnetisation.

Publications

A Synchrotron Radiation Study of Electronic and Magnetic Properties of Ultra-Small Manganese Particles

A.M. Keen, S.H. Baker, C. Binns, S. Mozley, C. Norris and H.S. Derbyshire
Surf. Rev and Letts 1 No.4 (1994) 525-527

Morphology of Islanded Transition Metal Films on Graphite Studied by XUV Reflectivity

C. Binns, S.H. Baker, A.M. Keen, S. Mozley, C. Norris and H.S. Derbyshire and S.C. Bayliss
Phys Rev B53 (1996) 7451-7459

Synchrotron Radiation Study of Mesoscopic Manganese Particles

A.M. Keen, C. Binns, S.H. Baker, S. Mozley, C. Norris and S.C. Thornton
Surf. Sci. 352-354 (1996) 715-718

Synchrotron Radiation Photoemission Study of Supported Mesoscopic Manganese Particles

C. Binns, S.H. Baker, A.M. Keen, C. Norris and S. Mozley
Sol. St. Comm. 99 No.5 (1996)353-357

The Construction of a Gas Aggregation Source for the Preparation of Mass-Selected Ultra-Small Particles.

S.H. Baker, S.C. Thornton, A.M. Keen, T.I. Preston, C. Norris and C. Binns
Accepted for publication in Rev. Sci Instr. (1996)

Magnetic Linear Dichroism Measurements of Fe Films on Graphite

S.H. Baker, K.E. Edmonds, C. Binns and A.M. Keen
Phys. Rev. B submitted (1996)

Spin Polarised Photoelectron Diffraction of Nanoscale Manganese Structures

A.M. Keen, C. Binns, S.H. Baker, S.N. Mozley, C. Norris and H.S. Derbyshire

In preparation to be submitted to Phys. Rev. Letts.

References

- Adawi I., Phys. Rev. **134** (1964) A788.
- Alvarado S. F., Campagna M. and Hopster H. Phys. Rev. Lett **48** (1982) 51.
- Bagus P. S. and Seel M., Phys. Rev. B **23** (1981) 2065.
- Baibich M. N., Broto J. M., Fert A., Nguyen van Dau F., Petroff F. Etienne P.,
Creuzet G., Friederich A. and Chazelas J., Phys. Rev. Lett. **61** (1988) 2472.
- Bailey P. and Quinn F. M., Daresbury technical memorandum DL/SCI/TM94E,
March 1993.
- Baker S. H., Edmonds K. W., Binns C. and Keen A. M., Phys. Rev. B (1996)
submitted.
- Baker S. H., Thornton S. C., Keen A. M., Preston T. I., Norris C. and Binns C.,
Rev. Sci. Instrum. (1996) in press.
- Baumgarten L., Schneider C. M., Petersen H., Schäfers F. and Kirschner J., Phys.
Rev. Lett. **65** (1990) 492.
- Berkowitz A. E., Mitchell J. R., Carey M. J., Young A. P., Zhang S., Spada F.
E., Parker F. T., Hutten A. and Thomas G., Phys. Rev. Lett. **68** (1992)
3745.
- Billas I. M. L., Châtelain A. and De Heer W. A., Science, **265** (1994) 1682.
- Billas I. M. L., De Heer W. A. and Châtelain A., J. Non-Cryst. Sol. **179** (1994) 316.
- Binns C. and Bayliss S. C., Surf. Sci. **214** (1989) 165.
- Binns C., Norris C., Derbyshire H. S. and Bayliss S. C., proceedings (ISPCFS)
International Symposium on the Physics and Chemistry of Finite
Systems, Richmond, Va, USA, Oct. 1991, published in "Physics and
Chemistry of Finite Systems: from Clusters to Crystals, NATO ASI series
eds. Jena, Khanna and Rao, Kluwer, Dordrecht, 1992.

- Binns C., Derbyshire H. S., Bayliss S. C. and Norris C. *Phys. Rev B* **45** (1992) 460.
- Binns C., Norris C., Baker S. H., Keen A. M. and Mozley S. N., Daresbury
Annual Report, 1995, *Rev. Sci. Instr.* in press (1996).
- Blügel S., Weinert M. and Dederichs P. H., *Phys. Rev. Lett.* **60** (1988) 1077.
- Born M. and Wolf E., *Principles of Optics*, 6th ed. (Oxford: Pergamon) (1980)
p61-66.
- Bross H., *Z. Phys. B* **28** (1977) 173.
- Bucher J. P., Douglass D. C. and Bloomfield L. A., *Phys. Rev. Lett.* **66** (1991)
3052.
- Cardona M. and Ley L., ed. *Photoemission in Solids Vol I* (Berlin: Springer-
Verlag) (1978) p133.
- Caroli C., Lederer-Rozenblat D., Roulet B. and Saint-James D., *Phys. Rev. B* **8**
(1973) 4552
- Castellani N. J., Leroy D. B. and Lambrecht W., *Phys. Stat. Sol.* **129** (1985) K69.
- Celotta R. J., Pierce D.C., Wang G.-C., Bader S. D. and Felcher G. P., *Phys. Rev.*
Lett. **43** (1979) 728.
- Chen J. P., Sorensen C. M., Klabunde K. J. and Hadjipanayis G. C., *J. Appl. Phys.*
76 (1994) 6316.
- Cheung T. T. P., *Surf. Sci.* **127** (1983) L129.
- Clegg O. L., *Proc. Phys. Soc. B* **64** (1952) 774.
- Cox A. J., Louderback J. G., Apsel S. E. and Bloomfield L. A., *Phys. Rev. B* **49**
(1994) 12295.
- David E. Z. *Phys.* **114** (1939) 389.
- Davies H., *Phys. World*, Vol. 7 (11) Nov. 1994 41.
- Drube W. and Himpsel F. J., *Phys. Rev. B* **35** (1987) 4131.

- Eberhardt W., Stöhr J., Outka D. and Madix R. J., *Sol. St. Commun.* **54** (1985) 493.
- Fan W. C., Strozier J. and Ignatiev A., *Surf. Sci.* **195** (1988) 226.
- Faraday M., *Phil. Trans. R. Soc.* **147** (1857) 145.
- Feder R., ed. *Polarised Electrons in Surface Physics* (World Scientific, Singapore) (1985).
- Feibelman P. J. and Eastman D. E., *Phys. Rev. B* **10** (1974) 4932
- Fink R. L., Ballentine C. A. and Erskine J. L., *Phys. Rev. B* **41** (1990) 10175.
- Fu C. L., Freeman A. J. and Oguchi T., *Phys. Rev. Lett.* **54** (1985) 2700
- Fuggle J. C., Umbach E., Menzel D., Wandelt K. and Brundle C. R., *Sol. St. Commun.* **27** (1978) 65.
- Ganz E. Sattler K. and Clarke J., *Phys. Rev. Lett.* **60** (1988) 1856.
- Ganz E. Sattler K. and Clarke J., *Surf. Sci.* **219** (1989) 33.
- Gay J. G., and Richter R., *Phys. Rev. Lett.* **56** (1986) 2728.
- Gijs M. A. M. and Okada M., *J. Magn. Magn. Mat.* **113** (1992) 105.
- Girouard F. E. and Truong Vo-Van, *J. Opt. Soc. Am.* **1** (1984) 76.
- Granqvist C. G. and Buhrman R. A., *J. Appl. Phys.* **47** (1976) 2200.
- Grepel D. R. and Ying S. C., *Phys. Rev. Lett.* **45** (1980) 1018.
- Gumprecht R. O. and Sliepcevich C. M., *J. Chem. Phys.* **57** (1953) 90.
- Hagemann H. -J., Gudat W. and Kunz C., *DESY Report: SR-74/7*, 1974.
- Harsdorff M., *Thin Solid Films* **32** (1976) 103.
- Harsdorff M., *Thin Solid Films* **90** (1980) 1.
- Henke B. L., Gullikson E. M. and Davis J. C., *At. Data & Nucl. Tables* **54** 181 (1993).
- Hermesmeier B., Fadley C. S., Krause M. O., Jimenez-Mier J., Gerard P. and Manson S. T., *Phys. Rev. Lett.* **61** (1988) 2592.

- Hermesmeier B., Osterwalder J., Friedman D. J. and Fadley C. S., Phys. Rev. Lett. 62 (1989) 478.
- Hermesmeier B., Osterwalder J., Friedman D. J., Sinkovic B., Tran T. and Fadley C. S., Phys. Rev. B 42 (1990) 11895.
- Holland B. W., Surf. Sci. 68 (1977) 490.
- Howells M. R., Norman D., Williams G. P. and West J.B., J. Phys. E. 11 (1978) 199.
- Jarrett D.N. and Ward L., J. Phys D: Appl. Phys. 9 (1976) 1515.
- Johnson M. T., Starnberg H. I. and Hughes H. P., J. Phys. C: Solid State Phys. 20 (1987) 4385.
- Johnson P. B. and Christy R. W., Phys. Rev. B 9 (1974) 5056.
- Kern R., Le Lay G. and Métois J. J., in Current Topics in Materials Science vol 3, ed. Kaldis E. (Amsterdam: North-Holland) (1979) p139.
- Kessler J. Polarised Electrons (Springer-Verlag, Berlin) (1976).
- Kinsinger V., Sander I., Steiner P., Zimmerman R. and Huffner S., Sol. St. Commun. 73 (1990) 527.
- Kobayashi S., Takahashi T. and Sasaki W., J. Phys. Soc. Japan, 32 (1972) 1234.
- Kubo R., J. Phys. Soc. Japan, 17 (1962) 975.
- Li C. H., Lubinsky A. R. and Tong S. Y., Phys. Rev. B 17 (1978) 3128.
- Li Y. Z., Patrin J. C., Chandler M., Weaver J. H., Chibante L. P. F. and Smalley R. E., Science 252 (1991) 547.
- Liebsch A., Electron and Ion Spectroscopy of Solids (New York: Plenum) (1978) p93
- McKenna W. T. and Ward L., Phys. Status Solidi a 68 (1981) K11.
- Maeda A., Minoru K., Oikawa S., Shimizu Y. and Masaru D., J. Phys: Condens Matter 5 (1993) L189.

- Mahan G. D., *Phys. Rev B* **2** (1970) 4334.
- Matthew J. A. D., *Sol. St. Commun.* **73** (1990) 179.
- Maxwell-Garnett J. C., *Phil. Trans. R. Soc. A* **203** (1904) 383.
- Maxwell-Garnett J. C., *Phil. Trans. R. Soc. A* **205** (1906) 237.
- Methfessel M., Hennig D. and Scheffler M., *Surf. Sci.* **287-288** (1993) 785.
- Metzger R.M., Bao X. and Carbucicchio M., *J. Appl. Phys.* **76** (1994) 6626.
- Meunier M. and Henry C., *Surf. Sci.* **307-309** (1994) 514.
- Mie G., *Ann. Physik* **25** (1908) 377.
- Miyake K. P., Kato R. and Yamashita H., *Sci. Light* **18** (1969) 39.
- Moodera J. S. and Meservey R., *Phys. Rev. B* **40** (1989) 8541.
- Nagasawa H. and Uchinami M., *Phys. Lett.* **42A** (1973) 463.
- Norton P. R., Tapping R. L. and Goodale J. W., *Surf. Sci.* **72** (1978) 33.
- O'Brien W. L. and Tonner B. P., *Phys. Rev. B* **50** (1994) 2963.
- Ojala E. J. and Terakura K. *Phys. Rev B* **33** (1986) 2733.
- Palik E.D. *Handbook of the Optical Properties of Solids* , Orlando Academic Press, 1984.
- Parkin S. S. P., Modak A. and Smith D. J., *Phys. Rev. B* **47** (1993) 9136.
- Pendry J. B., *J. Phys. C: Sol. St. Phys* **8** (1975) 2413.
- Pendry J. B., *Surf. Sci.* **57** (1976) 679.
- Proceedings (ISPCFS) International Symposium on the Physics and Chemistry of Finite Systems, Richmond, Va, USA, Oct. 1991, published in "Physics and Chemistry of Finite Systems: from Clusters to Crystals, NATO ASI series eds. Jena, Khanna and Rao, Kluwer, Dordrecht, 1992
- Rakotomahevitra A., Garreau G., Demangeat C. and Parlebas J.-C., *Surf. Sci.* **331** (1995), in press.
- Rau C., Liu C., Schmalzbauer A. and Xing G., *Phys. Rev. Lett.* **57** (1986) 2311.

- Rau C., Xing G. and Robert M., *J. Vac. Sci. Technol. A* **6** (1988) 579.
- Raue R., Hopster H. and Clauberg R., *Phys. Rev. Lett.* **50** (1983) 1623.
- Robins J. L., *Thin Solid Films* **32** (1976) 151.
- Robins J. L., *Surf. Sci.* **86** (1979) 1.
- Rothberg G. M., *J. Magn. Magn. Mat.* **15-18** (1980) 323.
- Rouard P. and Bousquet P., *Optica Acta* **16** (1969) 675.
- Sattler K. in "Physics and Chemistry of Finite Systems: from Clusters to Crystals" (eds. Jenna, Khanna and Rao), Kluwer, Dordrecht, 1992. p.61.
- Schade H. and Smith Z. E., *Appl. Opt.* **24** (1985) 3221.
- Schaiach W. and Ashcroft N., *Phys. Rev. B* **3** (1971) 2452.
- Seah M. P. and Dench W. A., *Surf. Interface Anal.* **1** (1979) 2.
- Sennett R. S. and Scott A. D., *J. Opt. Soc. Am.* **40** (1950) 203.
- Shull C. G. and Wilkinson M. K., *Rev. Mod. Phys.* **23** (1953) 100.
- Shull C. G., Strause W. A. and Wollan E. O., *Phys. Rev.* **83** (1951) 333.
- Siegmann H. C., Meier F., Erbudak M. and Landolt M. in: *Advances in Electronics and Electron Physics*, ed. Hawkes P. W. (Academic, New York) (1984) vol 62.
- Sinkovic B. and Fadley C. S., *Phys. Rev. B* **31** (1985) 4665
- Sinkovic B., Hermsmeier B. and Fadley C. S., *Phys. Rev. Lett.* **55** (1985) 1227.
- Sinkovic B., Friedman D. J. and Fadley C. S., *J. Magn. Magn. Mat.* **92** (1991) 301.
- Smart J. E., *Effective Field Theories of Magnetism* (Saunders: New York) (1966) chap 4.
- Sonntag B., Haensel R. and Kunz C., *Sol. St. Commun.* **7** (1969) 597.
- Spicer W. E., *Phys. Rev.* **112** (1958) 114
- Stampanoni M., Vaterlaus A., Pescia D., Aeschlimann M., Meier F., Dürr W. and Blügel S., *Phys. Rev. B* **37** (1988) 10380.

- Stenzel H., Velfe H. D. and Krohn M., *Kristall Technik* 15 (1980) 255.
- Stöhr J., Jaeger R. and Rehr J. J., *Phys. Rev. Lett.* 51 (1983) 821.
- Taylor J. S. and Newstead D. A., *J. Phys. E* 20 (1987) 1288.
- Teehan D., Daresbury Technical Memorandum, DL/SCI/TM82E December 1991.
- Tomboulain D. H. and Hartman P. L., *Phys. Rev.* 102 (1956) 1423.
- Tougaard S., *Phys. Rev. B* 34 (1986) 6779.
- Tsoukatos A., Wan H. and Hadjipanayis G.C., *Appl. Phys. Lett.* 61 (1992) 3059.
- Uozumi T., Okada K. and Kotani A., *J. Elec. Spec. Rel. Phenom.* 78 (1996) 103.
- Upward M. D., Moriarty P., Beton P., Baker S. H., Binns C. and Edmonds K., submitted to *Appl. Phys. Letts.* August 1996.
- Venables J. A., Spiller G. D. T. and Hanbücken M., *Rep. Prog. Phys* 47 (1984) 399.
- Waddill G. D., Tobin J. G., Guo X. and Tong S. Y., *Phys. Rev. B* 50 (1994) 6774.
- Walker T.G. and Hopster H., *Phys. Rev. B* 48 (1993) 3563.
- Walker T.G. and Hopster H., *Phys. Rev. B* 49 (1994) 7687.
- Wertheim G. K. and Citrin P. H. in *Photoemission in Solids I*, Topics in applied Physics Vol. 26, Springer-Verlag, 1978, (eds. M. Cardona and L. Ley).
- Xhie J., Sattler K., Mueller U., Venkateswaran N. and Raina G., *Phys. Rev. B* 43 (1991) 8917.
- Xhie J., Sattler K., Ge M. and Venkateswaran N., "Physics and Chemistry of Finite Systems: from Clusters to Crystals" (eds. Jenna, Khanna and Rao), Kluwer, Dordrecht, 1992. p.1159.
- Xu S., Evans B. L., Flynn D. I. and En C., *Thin Solid Films* 238 (1994) 54.
- Yamada T., Konitomi N., Nakai Y, Cox D. E. and Shirane G., *J. Phys. Soc. (Japan)* 28 (1970) 615.

Yamagata H. and Asayama K., J. Phys. Soc. (Japan) **33** (1972) 400.

Yamaguchi T., Yoshida S. and Kinbara A., Thin Solid Films **13** (1972) 261.

Yarwood J. in High Vacuum Techniques (London: Chapman and Hall) (1967).

Yokoyama G., Hiroshita N., Oguchi T., Kambara T. and Gondaira K. I., J. Phys. F
11 (1981) 643.